3.2 First-Principles Calculation of Material Properties

Atomic Structures and Electronic Properties of Hard- and Soft-Nanomaterials

Atsushi Oshiyama
Department of Applied Physics, The University of Tokyo
Hongo, Tokyo 113-8656

In the fiscal year of 2017, on the basis of the density-functional theory we have clarified 1) roles of stacking faults in electronic properties at SiC/SiO$_2$ interfaces[1], 2) physical and chemical origins of the electron states at the Fermi level and the disappearance of so called Dirac states in silicene on Ag substrate using our newly developed unfolding technique2, 3, and 3) the atom-scale mechanism of the atom manipulation by using AFM tip on Si (111) surface[4]. In the following, I explain the first issue.

An intrinsic interface state controlled by atomic stacking sequence at SiC/SiO$_2$

To realize energy-saving society, highly efficient power devices are necessary. SiC has been recognized to be suitable for such purpose due to its prominent material properties. SiC-MOSFET devices are indeed available commercially. However, they still face a severe problem that the electron mobility is far from the theoretical values due to the huge density of interface levels at the SiC/SiO$_2$ interface. In particular, energy levels appearing in the gap within the range of 0.3 eV below the conduction band minimum (CBM) are known to cause the substantial reduction of the electron mobility.

SiC is a tetrahedrally bonded semiconductor in which atomic bilayers consisting of Si and C atoms are stacked along the bond direction. Different stacking sequences lead to polytypes. Figure shows three typical SiC polytypes, 2H, 3C, and 4H structures. The most frequently obtained structure is the 4H-structure whose stacking sequence is depicted as ABCB. Although the local atomic structures of polytypes are identical to each other, their electronic properties, in particular, the band gaps, are known to differ from one to another. As we have clarified [PRL, 112, 136403 (2014)], this is due to the interesting character of the CBM: i.e., the wavefunction of the CBM is not distributed around the atomic sites but is extended or floats in the interstitial structural channels generally existing in the tetrahedrally bonded structures. This *floating* nature renders the energy level of the CBM being strongly affected by the length of the internal structural channel which is peculiar to each polytype.

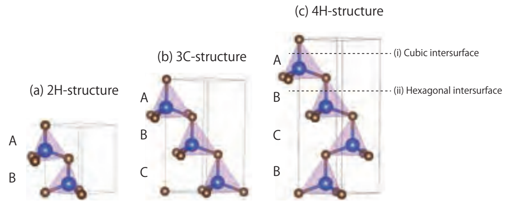

Figure 1: Atomic structures of (a) 2H-SiC, (b) 3C-SiC, and (c) 4H-SiC polytypes. Different stacking sequences of atomic bilayers are depicted by the letters, A, B and C. In (c), two dotted lines show (i) the cubic and (ii) the hexagonal surface planes. When SiO$_2$ films contact with the SiC substrate at the position (i) or (ii), we call it the cubic or the hexagonal interface.

Considering the layer-by-layer oxidation of 4H-SiC (0001) surface, only two types of the stacking termination at the interface are possible. Those correspond to the two interface planes shown by the dotted lines in Figure (c): One is a cubic interface [BCBA-stack/SiO$_2$ as shown in Figures (c) and (a)], and the other is a hexagonal interface [ABCB-stack/SiO$_2$ as in Figures (c) and (b)]. In addition to those interfaces, we here consider a stacking-fault interface, where the topmost stacking sequence in the hexagonal interface ABCB is changed to be ABCA, forming the ABCA-stack/SiO$_2$ shown in Figure (c). As deduced from the *floating* nature explained above, the variation of the stacking sequence near the interface leads to the variation of the channel length there and hereby varies the energy level of the CBM at the interface.

Figure is the calculated Local density of states (LDOS) for the three interfaces. Importantly, in the energy region near the CBM, the LDOS at the interface is sensitive to the atomic stacking

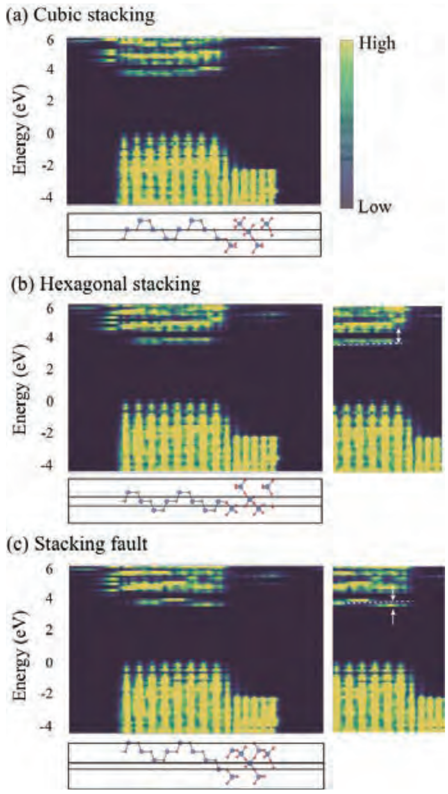

Figure 2: Calculated LDOS by the HSE functional for the cubic (a), the hexagonal (b), and the stacking-fault (c) interfaces. The left and right sides correspond to the SiC and SiO$_2$ regions.

at the interface. Comparing Figures (a) and (b), we have found that the hexagonal-stacking interface (ABCB-stack/SiO$_2$) induces an interface state located about 1.2 eV above the bulk CBM. This interface state is caused by the quantum confinement of the bulk CBM state in the shorter interstitial channel near the interface. Furthermore, in the stacking-fault interface (ABCA-stack/SiO$_2$), an interface state caused by the modulation of the length of the interstitial channel is located at 0.3 eV below the bulk CBM [Figure (c)]. This interface state induces not a single level but a band as observed in Figure (c). The width of the band is due to the kinetic energy dispersion in the lateral plane of the interface state. This unequivocally clarifies that the stacking difference near the interface changes the interface properties considerably.

Imperfection of atomic stacking is commonly observed in tetrahedrally bonded semiconductors. This planar imperfection has been thought to play a minor role in electronic structure. However, we have found, for the SiC(0001) surface or the interface, that this stacking sequence determines the length of the internal channel and thus induces interface states near CBM, which are strong candidates for the mobility killer, not yet identified before, in the performance of MOSFET devices. Importantly, the mechanism for the appearance of those interface states is the intrinsic *floating* nature of the conduction electrons in SiC. In contrast, the channel lengths are infinite in 3C-SiC. This fact means that the channel structure modification at interface can not be seen in 3C-SiC. Therefore, the interface states induced by stacking near the interface is not expected in 3C-SiC. Another noteworthy thing in 4H-SiC is non-polar surfaces such as (11$\bar{2}$0)- or (1$\bar{1}$00)-face. In actual SiC-MOSFET devices, non-polar surfaces In SiC MOSFET, non-polar surfaces such as (11$\bar{2}$0)- or (1$\bar{1}$00)-face are occasionally used for the device fabrication. In those non-polar surfaces, the lengths of the channels are infinite, thus being independent of the bilayer stacking along the (0001) direction. Hence, the interface state near the CBM is not expected to emerge by the stacking modulation on the non-polar surface. From this viewpoint, the (11$\bar{2}$0) and (1$\bar{1}$00) surfaces are expected to have advantages than the (0001) surface to fabricate high-performance SiC devices.

Related Publuications

1. Y.-i. Matsushita and A. Oshiyama, Nano Lett. **17**, 6458 (2017).
2. J.-I. Iwata, Y.-i. Matsushita, H. Nishi, Z.-X. Guo, and A. Oshiyama, Phys. Rev B **96**, 235442 (2017).
3. Y.-i. Matsushita, H. Nishi, J.-i. Iwata, T. Kosugi and A. Oshiyama, Phys. Rev. Materials **2**, 010801 (R) (2018).
4. B. Enkhtaivan, Y. Sugimoto and A. Oshiyama, Phys. Rev. B **96**, 155417 (2017).

Analyses on atomic structure, magnetism, and electronic structure in spintronics materials and molecular magnets

Tatsuki ODA[1,2], Mega CHRISTIVANA[2], Tomosato KANAGAWA[2], Indra PARDEDE[2],
Nurul IKHSAN[2], Hasan Al RASYID[2], Masao OBATA[2]

[1]*Institute of Science and Engineering, Kanazawa University, Kanazawa, Ishikawa 920-1192*

[2]*Graduate School of Natural Science and Technology, Kanazawa University, Kanazawa, Ishikawa, 920-1192*

We studied the several topics involved with this project; magnetic anisotropy and its electric field (EF) effect in the thin film related with spintronic devices. We also developed a method of van der Waals density functional (vdW-DF) approach for magnetic systems. These investigations have been done by employing the home-made density functional code, which has run efficiently in the architectures in Systems B in ISSP.

Magnetic anisotropy and electric field effect

Magnetic anisotropy energy (MAE) and its EF effect were investigated in the slab system of V/Fe/MgO by using first-principles calculation.

Such system keeps the Fe/MgO interface and was reported as a system with a large voltage-control magnetic anisotropy (VCMA) coefficient. We estimated MAEs and VCMA coefficient and analyzed the electronic structures in V/Fe/MgO slabs. As the results, we found the maximum perpendicular magnetic anisotropy energy of 1.5 mJ/m^2 and tends to decrease with the decreasing lattice constant. The EF control coefficient of MAE initially tends to increase to the reach maximum value 136 fJ/Vm with increasing the lattice constant, and then decreases to a negative value at the strain of 5.23% inducing with respect to the Fe lattice constant. This behavior may be addressed to the modulation of eigenstates of Fe minority d-orbital component at the interface near the Fermi level.

Van der Waals density functional approach

The vdW-DF approach is one of promising methods to overcome the problem that the density functional approach, such as local density approximation or generalized gradient approximation, cannot describe van der Waals (vdW) force properly. We have proposed the extension of vdW-DF to spin-polarized systems, vdW-DF-SGC (SGC stands for spin-polarization-dependent gradient correction), and demonstrated the usefulness. Another spin van der Waals method (svdW-DF) was developed in 2015. We found that the results of the svdW-DF is very similar to those of the vdW-DF-SGC by using the alpha solid oxygen.

We have extended the methods of vdW-DF to noncollinear magnetism. To demonstrate them, we have carried out the electronic structure calculation for the beta solid oxygen which has a spin configuration of 120 degree in the same oxygen layer. The results for the optimized crystal structure show an agreement with those obtained by experiments. We may study inadequate elements of vdW-DF to reproduce the structural properties in oxygen systems.

Analyses on atomic, magnetic, and electronic structures in high-performance spintronics materials and molecular magnets

Tatsuki ODA[1,2], Mega CHRISTIVANA[2], Tomosato KANAGAWA[2], Indra PARDEDE[2], Nurul IKHSAN[2], Hasan Al RASYID[2], Masao OBATA[2]

[1]*Institute of Science and Engineering, Kanazawa University, Kanazawa, Ishikawa 920-1192*

[2]*Graduate School of Natural Science and Technology, Kanazawa University, Kanazawa, Ishikawa, 920-1192*

We studied the several topics involved with this project; magnetic anisotropy and its electric field (EF) effect in the thin film related with spintronic devices and ferrimagnetic spinels. These investigations have been done by employing the home-made density functional code, which has run efficiently in the architectures in Systems B in ISSP. Additionally, we used a code of quasiparticle self-consistent GW method (QSGW) developed by Kotani et al.[1].

Magnetic anisotropy and electric field effect

Magnetic anisotropy energy (MAE) and its EF effect were investigated in the slab system of Cr/[CrFe]/Fe/MgO by using first-principles calculation. We estimated MAEs and voltage-control magnetic anisotropy (VCMA) coefficient (γ) and analyzed the electronic structures. We observe that the perpendicular magnetic anisotropy energy (PMAE) is enhanced when introducing Fe/Cr interchanges, compared with the system without interchange. This is related to the significant orbital reconstruction in electronic structure of Fe at the interface as a proximity effect of Cr. In this system, the enhanced PMAE can be achieved by both expansive and compressive strains. These behaviors are related to the oscillation position of d-orbital states near the Fermi level with magnetic quantum number |m|=1 and |m|=2. For the second one, we found that sign changes in γ are also induced by Fe/Cr interchanges and much enhanced at the compressive strain -3.1%, appearing with the minimum value of -170 fJ/Vm. The enhancement of γ is strongly related to the density of states (DOSs) in the vicinity of the Fermi level. Small modulation by EF in large DOS near and/or cross the Fermi level will increase or decrease the number of coupling states between occupied and unoccupied states. Hence, the PMAEs will significantly change, according to through the second order perturbation theory.

Nickel cobaltite spinels

Spinel compounds, AB_2X_4, could exhibit many different properties due to the choice of A, B and X atoms. The spinel compound $NiCo_2O_4$, which has a ferrimagnetic property, shows an interesting peculiar variation on its metallicity and magnetism, widely spanned from metallic-ferrrimagnetic until non-magnetic insulator. This unique properties of $NiCo_2O_4$ opens many possibilities for its application, i.e. as catalyst in oxygen reduction reaction, photonic devices, etc. To have better understanding and encourage efficient development process, we investigated electronic structures. We employed the density functional theory (DFT) and quasiparticle self-consistent GW method (QSGW) to elucidate electronic and magnetic properties of different types of $NiCo_2O_4$. The QSGW method is considered as one of post-DFT method that can better describe the properties of materials, due to its inclusion of many-body effects among electrons and the self-consistent treatment [1].

The QSGW shows a larger band gap on the majority spin state, compared to the GGA method. From its band structure, we found that NiCo2O4 has direct band gap around X point. This information might be important for experiment research to explore optical band gap properties from the angle-resolved photoemission spectroscopy (ARPES).

The discrepancies arose between both methods were also investigated, especially those on conduction band of majority-spin regarding hybridization of Ni e_g-orbital and that of octahedral Co. The band structure from the QSGW method have better agreement with the model proposed previously.

This information could be taken in making the model of interaction on $NiCo_2O_4$ surface.

[1] T. Kotani et al., PRL, **96**, (2006), 226402.

Large-scale device-material research by massively parallel electronic structure calculation and data science

Takeo Hoshi

Department of Applied Mathematics and Physics, Tottori University,
4-101 Koyama-Minami, Tottori 680-8550, Japan.

The present project was carried out for the joint research between electronic structure calculations and data science. Related mathematical studies and software development were also carried out. The main collaborators are Yusaku Yamamoto (U. Elec. Comm.), Koji Hukushima (U. Tokyo), Takatoshi Fujita (IMS), Hiroyuki Matsui (Yamagata U.), Toshio Hyodo and Ayahiko Ichimiya (KEK).

The large-scale electronic-state and transport calculations were carried out for flexible organic devices. As a main achievement, principal component analysis (PCA) was carried out so as to analyze large-scale electronic state calculation data for exploration of organic polymer device materials [1-3]. The method is given by the dimensional reduction of electronic wavefunctions, since the original data size is huge. The reduction is realized, when the participation ratio of wavefunctions, a measure of quantum localization, is chosen as the descriptor. The computation was carried out for electronic states for 40,000 samples of disordered organic polymers with 1,200 atoms by our large-scale electronic state calculation code ELSES (http://www.elses.jp/) on the K computer. As results, the polymer samples are classified into four groups correctly and the physical meaning of the principal components is clarified. The present method is general and forms a rigorous foundation of the data-driven material science. Numerical methods for large-scale electronic state calculations were developed for efficient contour integral [4], intermediate eigenpair computation [5], middleware for parallel eigenvalue computation with the performance prediction function by Bayesian inference [6]. In addition, preliminary researchs were carried out for large-scale exiton calculation of organic interface [7] and large-scale electronic state calculation of disordered pentacene thin film [8], the development of data analysis on positron diffraction experiment [9].

As mathematical studies, we developed a new preconditioner for the CG method which combines the block red-black ordering with relaxed modified incomplete Cholesky factorization. Numerical experiments on a multicore processor shows that the preconditioner is both effective and scalable [10]. We also developed a new algorithm for the nonlinear eigenvalue problem based on signed singular values [11].

References

[1] T. Hoshi, H. Imachi, K. Oohira, Y. Abe, and K. Hukushima, 'Principal component analysis with electronic wavefunctions for exploration of organic polymer device materials', International Meeting on High-Dimensional Data-Driven Science , Kyoto, 10-13. Sep. 2017

[2] T. Hoshi, H. Imachi, Y. Abe, K. Oohira, K. Hukusima, 'Principal component analysis with large-scale electronic state calculation for ultra-flexible device materials', Waseda U., 18th SIAM Conference on Parallel Processing for Scientific Computing (SIAM-PP18), 7-10, Mar. 2018.

[3] (Award) T. Hoshi, 'Organic-device material research based on 100-nano-meter electronic structure calculation and data science', Excellent achievement award of HPCI projects, 2. Nov., 2017.

[4] H. Kohashi, K. Sugita, M. Sugihara and T. Hoshi, 'Efficient methods for computing integrals in electronic structure calculations', JSIAM Letters 9, pp. 81-84 (2017)

[5] D. Lee, T. Hoshi, T. Sogabe, Y. Miyatake, S.-L. Zhang, 'Solution of the k-th eigenvalue problem in large-scale electronic structure calculations', submitted; Preprint (http://arxiv.org/abs/1710.05134).

[6] T. Hoshi, T. Fukumoto, T. Fukaya, Y. Yamamoto, 'Analysis and prediction of the performance in generalized eigenvalue solvers on Oakforest-PACS', International Workshop on Eigenvalue Problems: Algorithms; Software and Applications, in Petascale Computing (EPASA2018), 5-6, Mar. 2018.

[7] MD K. ALAM, T. Fujita, T. Hoshi, 'Excited-state calculation for large size C60/Pentacene interface based on the fragment molecular orbital method', Meeting of The Japan Society of Applied Physics, Hakata, 5-8, Sep 2017.

[8] T. Hoshi, Y. Abe, A. Kuwata, K. Kakuda, T. Fujita, H. Matsui, 'Large-scale electronic state calculation in disordered pentacene thin film', Meeting of The Japan Society of Applied Physics, Waseda U., 17-20, Mar. 2018 (Japanese)

[9] T. Hoshi, K. Tanaka, I. Mochizuki, T. Hyodo, A. Ichimiya, Y. Nakanishi, K. Hukushima, 'Development of data analysis software for positron diffraction', 2nd Workshop on Positron Diffraction, organized by T. Hyodo and T. Hoshi, KEK Tsukuba, 30. Mar. 2018. (Japanese)

[10] A. Shioya and Y. Yamamoto, 'The danger of combining block red–black ordering with modified incomplete factorizations and its remedy by perturbation or relaxation', Jpn. J. Ind. Appl. Math., 35, pp 195-216 (2018).

[11] K. Ooi, Y. Mizuno, T. Sogabe, Y. Yamamoto and S.-L. Zhang, 'Solution of a nonlinear eigenvalue problem using signed singular values', East Asian J. Appl. Math. 7, pp. 799 - 809 (2018).

Development of first-principles electronic-structure and transport calculation method based on real-space finite-difference approach

Tomoya ONO
Center for Computational Sciences, University of Tsukuba
Tennodai, Tsukuba, Ibaraki 305-8577

1 Introduction

Among the high-k materials, HfO_2 is one of the most intensively studied materials for the gate oxide of MOSFET because of its large dielectric constant, large band gap, and thermodynamic stability. The performance of such high-k-based MOSFETs depends on the interface state formed between the HfO_2 layer and Si substrate. Oxygen vacancies are generated in the HfO_2 layer, SiO_2 layer, and at HfO_2/SiO_2 interface. However, the relationship between the leakage current and oxygen vacancies in high-k gate stacks is not fully understood.

In this study, the leakage current through $HfO_2/SiO_2/Si(001)$ gate stacks are investigated by a first-principles calculation based on density functional theory (DFT).

2 Computational models and methods

Several studies on HfO_2-based gate stacks involving first-principles calculations have been performed using interface atomic structures consisting of crystalline SiO_2 and HfO_2. The monoclinic HfO_2 structure is widely employed for the computational models in first-principles calculations. In accordance with previous studies, the monoclinic HfO_2/β-cristobalite SiO_2/Si structure is employed for our computational model, as shown in Fig. 1. Following the study by Capron *et al.*,[1] oxygen vacancies are inserted by removing an O atom from the HfO_2 layer, HfO_2/SiO_2 interface plane, or SiO_2 interlayer and the doubly positively charged state is considered for the vacancy in the HfO_2 layer. The positions of oxygen vacancies are indicated by arrows in Fig. 1(b). The model without the O atom indicated by Ox is referred to as V_{Ox}.

To perform the electronic-structure and electron-conduction calculations, we employ first-principles calculation code RSPACE[2] based on DFT and real-space finite-difference method. The other computational details are explained in Ref. 3. The interface atomic structures in the scattering region are those obtained by the structural optimization. In our computational model for the electron-conduction calculation, a monoclinic HfO_2/β-cristobalite SiO_2/Si structure consisting of three molecular layers of HfO_2, two molecular layers of SiO_2, and eight atomic layers of Si is suspended between Al jellium electrodes.

3 Leakage current

The ratios of the leakage current are shown in in Table 1, where the leakage current of the interface without oxygen vacancies is set to 1. It is found that the leakage current is increased by the generation of oxygen vacancies in the HfO_2 layer. In the cases of V_{O1} and V_{O1}^{2+}, the leakage currents are 247 and 396 times that in the model before the generation of oxygen va-

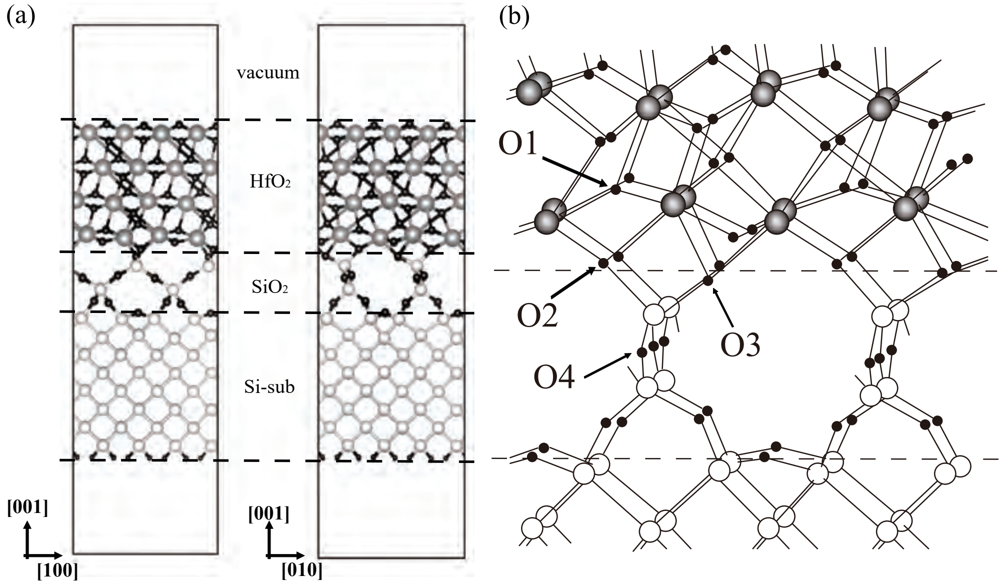

Figure 1: (a) Computational model of monoclinic HfO_2/β-cristobalite SiO_2/Si(001). Gray, black, white, and small black balls represent Hf, O, Si, and H atoms, respectively. (b) Enlarged view at the interface plane. Arrows represent O atoms that are removed. The model without an O atom at an Ox site is referred to as V_{Ox}. Figure is taken from Ref. 3.

Table 1: Ratios of leakage current for models with and without oxygen vacancies. Data are taken from Ref. 3.

Model	Current ratio
No oxygen vacancy	1.0
V_{O1}	247
V_{O2}	1.3
V_{O3}	3.6
V_{O4}	2.6
V_{O1}^{2+}	396

cancies, respectively. On the other hand, the amount of the leakage current is comparable when oxygen vacancies exist at the HfO_2/SiO_2 interface plane or in the SiO_2 interlayer. It is reported that charged oxygen vacancies appear in an n-type MOSFET under zero gate voltage stress or a p-type MOSFET under finite gate voltage stress. The ratio of the leakage current of V_{O1}^{2+} is larger than that of V_{O1}, however the effect of charged states is not significant compared with the position of the vacancies. It is reported by an experimental study that doubly charged oxygen vacancies are replaced by neutral oxygen vacancies by applying voltage stress and that the decrease in the leakage current is not large, a maximum of 30%, when the density of the doubly charged oxygen vacancies is decreased. Our result is consistent with this experimental result.

References

[1] N. Capron, P. Broqvist, and A. Pasquarello: Appl. Phys. Lett. **91** (2007) 192905.

[2] K. Hirose, T. Ono, Y. Fujimoto, and S. Tsukamoto: *First-Principles Calculations in Real-Space Formalism, Electronic Configurations and Transport Properties of Nanostructures* (Imperial College, London, 2005).

[3] K. Takagi and T. Ono: Jpn. J. Appl. Phys., in press.

Theoretical Analyses on Ionic Transport Properties, Electrical Properties and Interfacial Electronic States of Nanostructures

Satoshi WATANABE
Department of Materials Engineering, the University of Tokyo
7-3-1 Hongo, Bunkyo-ku, Tokyo, 113-8656

1 Introduction

Design and control of novel nanoscale information and energy devices require us to deepen our understanding on complicated situations and phenomena at nanoscale. Keeping this in minds, we have been performing atomic/electronic level simulations (mainly based on density functional theory (DFT)), taking various nanostructures as target systems. In the followings, some of our results in the fiscal year 2017 are described.

2 Development of neural network interatomic potentials to study ion diffusion in amorphous materials

Ion diffusion behaviors in amorphous materials play important role in several novel devices such as resistive memories. To clarify such behaviors, atomistic simulations based on density functional theory (DFT) are powerful, but they need heavy computation for amorphous materials. So we have tried to construct interatomic potentials for efficient prediction of ion diffusion behaviors using neural network (NN).

We adopted the high-dimensional NN potential proposed by Belher and Parrinello [1]. To obtain the data used for training NN, DFT calculations were performed using VASP package.

Firstly, we have constructed a NN potential for amorphous Li_3PO_4 [2, 3]. The average errors of the NN potential, compared with the DFT calculations, are 48 meV and 41 meV in calculating energy barriers of diffusion paths and diffusion activation energy, respectively. Moreover, the NN potential was applied to simulations using much larger supercell (about 1,000 atoms) than the cell used in the training (about 120 atoms). The Li diffusivity evaluated by molecular (MD) simulations with the large cell agrees well with the experimental observation.

Second, we have developed a NN potential to study Cu diffusion in amorphous AlO_x system with the wide range of variation in density (2.7-3.3 g/cm^3) and atomic composition (O/Al ratio of 1.0-1.5) [3]. The accuracy of the NN potential in energy prediction was about 14 meV/atom in the whole range of density and composition variation. Preliminary MD simulations show that the Cu diffusion activation energies decreased from 1.02 eV to 0.79 eV with the decrease of AlO_x density from 3.1 to 2.7 g/cm^3, while the variation of O/Al ratio does not affect the Cu diffusion activation energy significantly.

3 Li defect formation and interfacial structures of γ-Li_3PO_4/metal stacked systems

Recently, a novel memory device had been proposed using Au/Li_3PO_4/Li (or Ni/Li_3PO_4/Li) stacked structures, which exhibit two different voltage states by applying voltages [4].

Cyclic voltammetry and alternating current impedance spectroscopy measurements suggest different metal-Li_3PO_4 interface structures between the two states. Though it is speculated that the Li diffusion must be the key in the change of the interface structure, microscopic details of the two states was unknown. Therefore, we have investigated the Li vacancy and interstitial formation at the interface using DFT calculations and one-dimensional continuum-model calculations [5]. As the simulation models, we adopted Au(111)/γ-Li_3PO_4/Au(111) and Li(001)/γ-Li_3PO_4/Li(001). Formation energies calculated via DFT were used in the continuum-model calculations [6].

Our calculation results show that in the Au case within the realistic range of Li chemical potential, Li interstitials stay at the interface, while Li vacancies do not. On the other hand, the stability of the two Li defects depends on the Li chemical potential in the Li case. In both cases, the region where the Li defects accumulate is within 1 nm or less from the interface. On the basis of our results, we suggest that the interstitial Li-ions formed at few Å from the Au(111) interface and the Li-Au alloying play a central role in the switching of the novel memory device.

References

[1] J. Behler and M. Parrinello: Phys. Rev. Lett. **98** (2007) 146401.

[2] W. Li, Y. Ando, E. Minamitani and S. Watanabe: J. Chem. Phys. **147** (2017) 214106.

[3] W. Li, Doctoral thesis, The University of Tokyo (2017).

[4] I. Sugiyama, R. Shimizu, T. Suzuki, K. Yamamoto, H. Kawasoko, S. Shiraki and T. Hitosugi: APL Mater. **5** (2017) 046105.

[5] K. Shimizu, W.Liu, W. Li, S. Kasamatsu, Y. Ando, E. Minamitani and S. Watatanbe: in preparation.

[6] S. Kasamatsu, T. Tada and S. Watanabe: Solid State Ionics **183** (2011) 20.

First-Principles Study of Excited Electron Dynamics and Optical Responses of Nanostructures

Kazuyuki WATANABE, Yasumitsu SUZUKI,
Yoshihiro UEDA, Kazuki UCHIDA, Tomoki SHINOZAKI
Department of Physics, Tokyo University of Science
1-3 Kagurazaka, Shinjuku-ku, Tokyo 162-8601

In this project we investigated the following five topics this year. 1) Angle-resolved secondary electron emission from atomic sheets, 2) plasmon excitation and electron emission of a carbon nanotube, 3) exact time-dependent exchange-correlation potential in electron scattering processes, 4) positron-stimulated ion desorption from $TiO_2(110)$ surface, and 5) electron transmission through mono- and bilayer graphene.

1) *Angle-resolved secondary electron emission from atomic sheets* [1]: Angle-resolved secondary electron emission (ARSEE) spectra of atomic sheets have been considered to reflect the unoccupied energy bands of the targets. However, far less is known about the dynamics of electron excitation from the valence bands to the unoccupied bands upon electron impact, leading to emission into the vacuum. We kept track of the electrons excited to the unoccupied bands and emitted to the vacuum in real time, position space, and k-space simultaneously by our homemade time-dependent density-functional theory (TDDFT) code, KENS. Parallelized calculations have been performed using System B. We have demonstrated that the calculated ARSEE spectra capture the unoccupied band structure of the atomic sheets. The excitation dynamics that lead to SEE have also been revealed by the time-dependent Kohn-Sham decomposition scheme. In this study the mechanism for the experimentally observed ARSEE from atomic sheets was elucidated with respect to both energetics and the dynamical aspects of SEE.

2) *Plasmon excitation and electron emission of a carbon nanotube* [2]: We studied the properties of electron excitation and emission of a finite carbon nanotube (CNT) under a linearly polarized femtosecond laser using our homemade real-space TDDFT code, RENS. Parallelized calculations have been performed using System B. We found a plasmon resonance in the near-infrared region of the optical absorption spectrum that is highly sensitive to the laser polarization direction. The laser polarization direction dependence of the plasmon excitation obtained is consistent with the properties of polarized optical absorption observed in experiments. In electron emission that occurs subsequent to electronic excitation, the yield of emitted electrons also shows a laser polarization direction dependence, and the kinetic energy spectrum of the emitted electrons is broadened in the high-energy regime due to the electron acceleration caused by plasmon-induced electric-field enhancement. These findings are of crucial importance for understanding the laser-CNT interaction, which is a prerequisite for applications of CNTs in electron emitters, nanodevices, and optoelectronic components and sensors.

3)*Exact time-dependent exchange-correlation potential in electron scattering processes* [3]: We calculated the exact exchange-correlation potential of time-dependent density functional theory in one-dimensional electron scattering system, and identified crucial peak and valley structures. These structures are completely missed by adiabatic approximations that, consequently, significantly underestimate the scattering probability. We also showed that a recently proposed nonadiabatic approximation, v^s_{xc}, correctly capture the approach of the electron to the target when the initial Kohn-Sham state is chosen judiciously, and it is more accurate than standard adiabatic functionals but ultimately fails to accurately capture reflection. These results explain the underestimation of scattering probabilities in some recent studies on molecules and surfaces. Part of the computations that required a lot of memory were performed on System B.

4) *Positron-stimulated ion desorption from* TiO_2*(110) surface* [4]: This is a joint work with an experimental group. We studied the positron-stimulated O^+ ion desorption process from a TiO_2(110) surface. The measured data indicate that the O^+ ion yields depend on the positron incident energy in the energy range between 0.5 keV and 15 keV. This dependence is closely related to the fraction of positrons which diffuse back to the surface after thermalization in the bulk. We calculated the electron and positron work functions and positronium affinity at TiO_2(110) surface using two-component DFT implemented in ABINIT code. By comparing the calculated positron binding energy and work function, we showed that thermalized positrons which diffuse back to the surface can be trapped by the surface induced image potential. Based on the experimental and computational results, we concluded that the ion desorption via positron-stimulation occurs dominantly by the annihilation of surface-trapped positrons with core electrons of the topmost surface atoms. All calculations were performed with ABINIT code on System B.

5) *Electron transmission through mono- and bilayer graphene* [5]: This is also a joint work with an experimental group. The experimental group proposed a virtual substrate method to characterize nanomaterials without the influence of underlying substrate signals from four interrelated measurements. We calculated elastic transmission coefficient of mono- and bilayer graphene by real-time TDDFT simulation with RENS code, which well corresponded with the virtual substrate measurements. Based on the experimental and computational results, we concluded that the virtual substrate method represents a benchmark to provide free-standing nanomaterial information from measurements of substrate-supported samples. All TDDFT calculations were performed on System B.

References

[1] Y. Ueda, Y. Suzuki, and K. Watanabe, Phys. Rev. B **97**, 075406 (2018).

[2] K. Uchida and K. Watanabe, Phys. Rev. B **96**, 125419 (2017).

[3] Y. Suzuki, L. Lacombe, K. Watanabe, and N. T. Maitra, Phys. Rev. Lett. **119**, 263401 (2017).

[4] T. Yamashita, S. Hagiwara, T. Tachibana, K. Watanabe, and Y. Nagashima, Materials Research Express **4**, 116303 (2017).

[5] B. Da, J. Liu, M. Yamamoto, Y. Ueda, K. Watanabe, N. T. Cuong, S. Li, K. Tsukagoshi, H. Yoshikawa, H. Iwai, S. Tanuma, H. Guo, Z. Gao, X. Sun, and Z. Ding, Nat. Commun. **8**, 15629 (2017).

First-principels study of anomalous thermoelectric effect on magnetic materials

Fumiyuki ISHII, Susumu MINAMI, Teguh Budi PRAYITNO, Yo Pierre MIZUTA
Faculty of Mathematics and physics, Institute of Science and Engineering, Kanazawa University
Kanazawa, 920-1192, Japan

Anomalous transport properties originated in Berry curvature is one of the key ingredients of new thermoelectric(TE) materials. For example, the anomalous Nernst effect (ANE), which is induced by the anomalous Hall effect (AHE) is one of the TE phenomena caused by the Berry curvature. ANE and AHE are reported in various magnetic materials[1, 2] which are not only ferromagnetic but also antiferromagnetic. However the magnitude of anomalous Nernst coefficient is quite small to apply it for TE generation device.

Our aim is to find and design materials with large ANE and clarify the origin of large ANE system. We have investigated two kind of systems as follows based on first-principles calculations based on density functional theory (DFT) implemented in OpenMX code[3]. We have constructed maximally localized Wannier functions (MLWF) using Wannier90 code[4] and evaluated the transport properties within the semiclassical Boltzmann transport theory with relaxation time approximation.

Magnetic half-Heusler compounds CoMSb (M=V, Cr, Mn)

We focused on the half-Heusler compounds CoMSb (M=V, Cr, Mn) and calculated ANE systematically. Half-Heusler intermetallic compounds have a face-centered cubic crystal structure with chemical composition XYZ and space group $F\bar{4}3m$. CoVSb and CoMnSb are known as ferromagnetic compounds with Curie temperatures of 58K and 490K, respectively[5, 6].

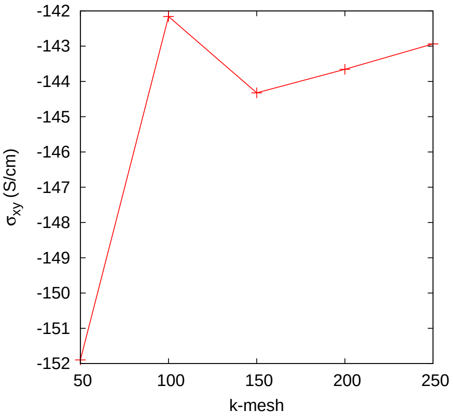

Figure 1: k-mesh dependence of anomalous Hall conductivity $\sigma_{xy}|_{T=0}$ for CoVSb at Fermi energy. σ_{xy} are calculated by using $k \times k \times k$ mesh in the Brillouin zone.

First, we checked the convergence of the anomalous Hall conductivity (AHC) in terms of k point sampling. Figure 1 shows k-mesh dependence of AHC σ_{xy} on CoVSb at Fermi energy. The evaluation of the AHC require a lot of k point sampling and it can be efficiently parallelized. We confirmed that over the 100 k-mesh is sufficient to obtain accurate results.

Figure 2 shows carrier concentration dependence of anomalous Nernst coefficient in CoMSb at 300K. Transport properties are calculated by using constant relaxation time approximation (τ = 3fs). The results show each materials have a peak of ANE near the Fermi energy. We also found that the peaks shift corresponding to the number of valence electron

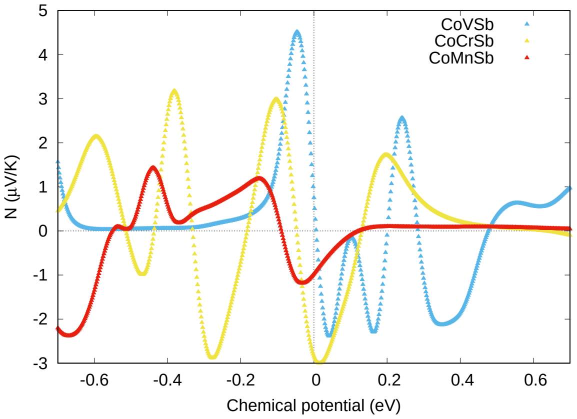

Figure 2: Anomalous Nernst coefficient at 300K. The Fermi energy is set to 0 eV.

of M. We investigated CoMnSb in details because of its applicability for an ANE-based TE module that can operate below room temperature. In conclusion, the origin of the large ANE on CoMnSb is the large Berry curvature on symmetry line of the Z-Uz in the Brillouin zone[7].

Topological half-Heusler compound YPtBi

We have calculated topological surface states for half-Heusler compounds YPtBi, which is known as a one of the topological semimetal by using band unfolding method. In this calculation, we used 46 atomic-layer slab model with a vacuum more than 15 Å. The calculation are considered three kind of terminated condition, namely the atom on the surface is Y, Bi, and Pt.

Figure 3 shows calculated surface state of Bi-terminated YPtBi. We obtained non-trivial topological surface sate around the Γ point and metallic surface state around the M point, which is correspond to the calculated and observed results[8].

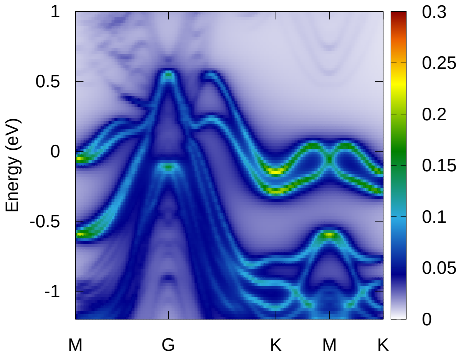

Figure 3: Calculated surface state of Bi-terminated YPtBi. The intensity spectra are calculated by projecting the band onto the 10 atomic-layer unit cell.

References

[1] K. Hasegawa, et al., Appl. Phys. Lett. **106** (2015) 252405.

[2] M. Ikhlas et al., Nat. Phys. **13** (2017) 1085.

[3] T. Ozaki et al., OpenMX, http://www.openmx-square.org.

[4] A. A. Mostofi et al., Comput. Phys. Commun. **178**, (2008) 685.

[5] M. Otto et al., J. Magn. Magn. Mater. **70** (1987)33.

[6] M. Terada et al., J. Phys. Soc. Jpn **32** (1972) 91.

[7] S. Minami, F, Ishii, Y. P. Mizuta, and M. Saito, arXiv:1804.00297.

[8] Z. K. Liu et al., Nat. Commun. **7** (2016) 12924.

First-principles calculations of spin textures at the surfaces and interfaces

Fumiyuki ISHII, Megumi SUGITA, Hikaru SAWAHATA,
Yo Pierre MIZUTA, Naoya YAMAGUCHI
Faculty of Mathematics and Physics, Institute of Science and Engineering, Kanazawa University
Kanazawa, 920-1192, Japan

We have studied the systems with special spin structures applicable to spintronics or thermoelectric conversion based on first-principles density functional calculations using OpenMX. This year, we focused on surfaces/interfaces with spin splittings such as Rashba spin splittings that can lead to spin-to-charge conversion (from a spin current to a charge current), and investigated topological insulators, and skyrmions. We also improved the code to calculate spin textures and enhanced the code of the band unfolding scheme in OpenMX to analyze spin textures for unfolded band structures.

Rashba Effect

Spin-to-charge conversion due to the Rashba effect, that is, the inverse Rashba-Edelstein effect (IREE) was observed in two-dimensional electron gas (2DEG) at various interfaces [1, 2]. The efficiency of IREE may become higher, as the Rashba coefficient, the strength of the Rashba effect, α_R is larger [1]. Therefore, the 2DEG with large spin splittings are promising candidates for such spintronic materials. The Rashba coefficient α_R can be controlled by a built-in electric field at surfaces and interfaces, i.e. electric polarization. For $SrTiO_3$, there is the strain-induced polarization, which can be controlled by the epitaxial strain [3].

In this project, we investigated the Rashba effect for interfaces between perovskite-type oxides ($PbTiO_3$, $BiAlO_3$) and noble metals (Cu, Ag, Au) and the effect of strain on $LaAlO_3/SrTiO_3$ interfaces and $SrTiO_3$ surfaces. For a tensile-strained $LaAlO_3/SrTiO_3$ interface, there is the strain dependence of the spin splitting (Fig. 1) and for the tensile strain of 5%, we found the persistent spin helix state, which has a long spin life time [4]. For a compressive-strained $SrTiO_3$ surface, we found the 2DEG with a Rashba spin splitting of $\alpha_R = 155.7$ meV·Å (Fig. 2) [5].

In order to investigate the Rashba effect at Bi_2O_3/M (M=Cu, Ag, Au) interfaces, we also calculated the electronic structures and spin textures for the realistic model (>100 atoms) and the simple model based on Bi/M (M=Cu, Ag, Au) surface alloy structures, as for an bismuth atom, an oxigen atom is located at a two-fold bridge site randomly.

For the Bi/M-surface-alloy-based model, the system was modeled by using the supercell method, and thus we used the unfolding method to compare the calculated band structure with that for a $M(111)$ surface. Besides, we enhanced the unfolding scheme in OpenMX so that the spin components could be analyzed and we confirmed that there were spin splittings in the unfolded band structures.

Calculating fine spin textures or unfolding band structures along a **k**-path including many **k**-points, especially for the realistic system with the large number of atoms, requires large computational resources (e.g. memory) and we improved our calculation code of spin textures in terms of parallelization for **k**-points by changing the schemes and data structures from those for small computers to those for supercomputers. We investigated the trend of α_R of Bi_2O_3/M using the realistic model, and found the sign change of α_R between systems with different M. These results support the experiments and are published in a collaboration work with the experimental group [6].

Anomalous Nernst Effect

We focus on the anomalous Nernst effect (ANE), heat-to-electricity conversion in transverse direction, driven by an emergent magnetic field originating from spontaneous inhomogeneous magnetization. We have so far found from computations on some models that, in the so-called 2D skyrmion crystal (SkX) phase, where skyrmions are crystallized in two dimensions, the crystal-momentum component of effective magnetic field gives rise to the band structure that could generate large ANE when chemical potential is properly tuned[7]. Although this behavior was most clearly confirmed in the simplest model of square SkX with single s-orbital per site, our subsequent computations on more realistic models of transition-metal oxides also showed possible large ANE[8]. A sizable transverse thermoelectric coefficient is predicted to arise, by means of first-principles calculations, in a Skyrmion crystal assumed on EuO monolayer where carrier electrons are introduced upon a quantum anomalous Hall insulating phase of Chern number C = 2. This encourages future experiments to pursue such an effect.

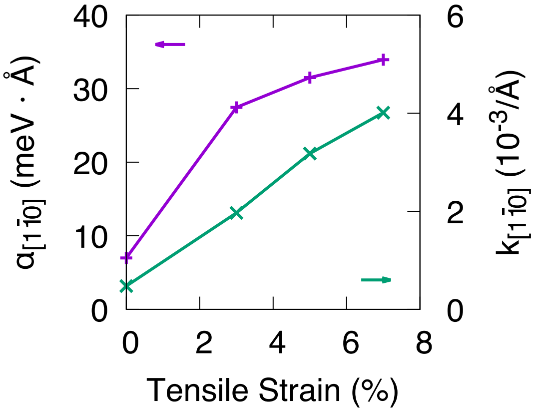

Figure 1: Strain dependence of the spin-orbit coefficient and the momentum offset along $[1\bar{1}0]$-direction in a $LaAlO_3/SrTiO_3$ interface.

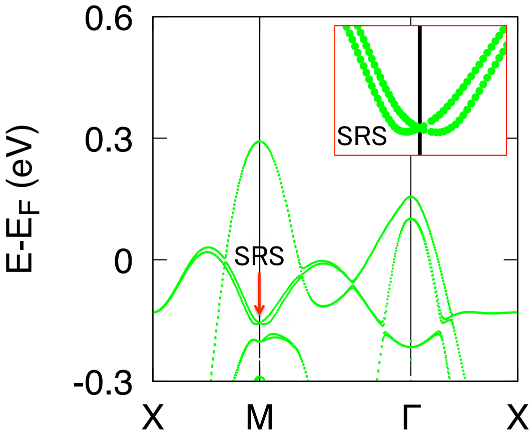

Figure 2: Surface-projected band structures for a strained $SrTiO_3$ surface. The inset shows the enlarged view for surface Rashba states.

References

[1] J. C. Rojas Sánchez et al., Nat. Commun. **4**, 2944 (2013).

[2] E. Lesne et al., Nat. Mater. **15**, 1261 (2016).

[3] J. H. Haeni et al., Nature **430**, 758 (2004).

[4] N. Yamaguchi and F. Ishii, Appl. Phys. Express **10**, 123003 (2017).

[5] N. Yamaguchi and F. Ishii, *submitted.*

[6] H. Tsai, S. Karube, K. Kondou, N. Yamaguchi, F. Ishii and Y. Otani, Sci. Rep. **8** 5564 (2018).

[7] Y. P. Mizuta and F. Ishii, Scientific Reports **6**, 28076 (2016).

[8] Y. P. Mizuta, H. Sawahata, and F. Ishii, arXiv:1803.08148.

Ab initio molecular dynamics simulation of graphene/ionic liquids interfaces

Tatsuhiko OHTO

Graduate School of Engineering Science,

Osaka University, 1-3 Machikaneyama, Toyonaka, Osaka 560-8531

Ab initio MD (AIMD) is a powerful tool to describe heterogeneous systems such as the water/solid interface, Although AIMD is computationally expensive, it describes electronic states beyond classical force fields,[1] which is important for interfaces. We calculated graphene/ionic liquid interfaces using the CP2K code [2].

We studied the interfacial structure of room temperature ionic liquids (RTILs).[3] RTIL interfaces controls many of the unique properties of RTILs, such as the high capacitance of RTILs and the efficiency of charge transport between RTILs and electrodes. RTILs have been experimentally shown to exhibit interfacial molecular layering structures over a 10 Å length scale. However, the driving force behind the formation of these layered structures has not been resolved. Here, we report *ab initio* molecular dynamics simulations of imidazolium RTIL/air interfaces along with force field molecular dynamics simulations. We find that the π+–π+ interaction of imidazolium cations enhances the layering structure of RTILs, despite the electrostatic repulsion. The length scales of the molecular layering at the RTIL/air and RTIL/graphene interfaces are very similar, manifesting the limited effect of the substrate on the interfacial organization of RTILs.

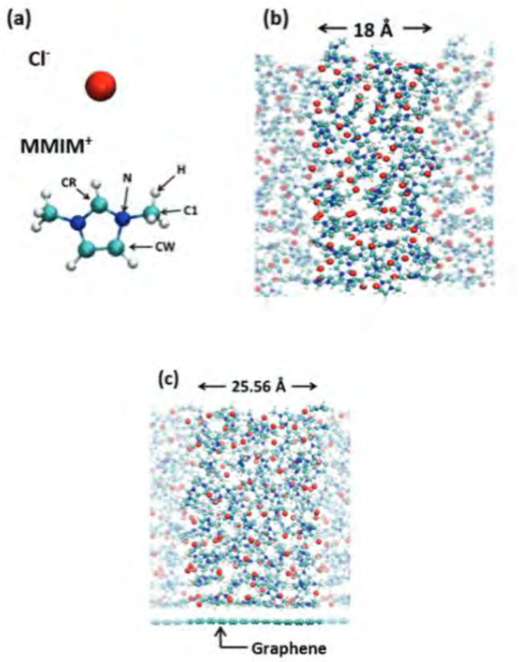

Fig. 1: Structures of RTIL, RTIL-air and RTIL-graphene interfaces.

References

[1] T. Ohto et al. Phys. Chem. Chem. Phys. **19**, 6909 (2017).

[2] The CP2K developers group, http://cp2k.berlios.de/

[3] T. Fujie et al. Phys. Chem. Chem. Phys. **19**, 2805 (2017)

Ab initio molecular dynamics simulation of doped-graphene/water interfaces

Tatsuhiko OHTO

Graduate School of Engineering Science,

Osaka University, 1-3 Machikaneyama, Toyonaka, Osaka 560-8531

Ab initio MD (AIMD) is a powerful tool to describe heterogeneous systems such as the water/solid interface, Although AIMD is computationally expensive, it describes electronic states beyond classical force fields,[1] which is important for interfaces.

We have simulated sum-frequency generation (SFG) spectra of isotopically diluted water at the water-graphene and water-hexagonal boron-nitride (hBN) sheet interfaces, using ab initio molecular dynamics simulations. The simulations themselves were performed using ISSP several years ago and recently we have submitted a paper.[2] A sharp 'dangling' O-D peak around ~2640 cm-1 appearing in both simulated SFG spectra evidences that both graphene and hBN are hydrophobic. The dangling O-D peak is 10 cm^{-1} red-shifted at the water-hBN interface relative to the peak at the water-graphene interfaces. This frequency difference manifests a stronger O-D…N intermolecular interaction between water and hBN than a O-D…C interaction between water and graphene.

To modify the hydrophobic interaction, we calculated doped-graphene water interfaces using the CP2K code [3]. We prepared 2 % B-doped, 2 % N-doped and 10 % N-doped graphene sheets. We tried to accumulate the 80 ps trajectory for each system and completed 50 % of AIMD runs. We will continue running the AIMD and analyze the results after completing the AIMD simulations.

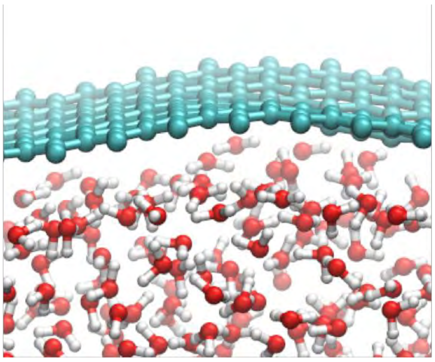

Fig. 1: Structures of the graphene-water interface.

References

[1] T. Ohto et al. Phys. Chem. Chem. Phys. **19**, 6909 (2017).

[2] T. Ohto et al. submitted.

[3] The CP2K developers group, http://cp2k.berlios.de/

Ab initio phonon calculations for $Ca_5Ir_3O_{12}$

Kazuma NAKAMURA
Quantum Physics Section, Kyushu Institute of Technology
1-1 Sensui-cho, Tobata, Kitakyushu, Fukuoka, 804-8550

The title compound has recently attracted attention as a thermoelectric material because it has a relatively high Seebeck coefficient. In this study, we report an ab initio study about electronic and phononic properties for $Ca_5Ir_3O_{12}$. In particular, we investigated the effect of spin-orbit interaction (SOI) on the low-energy properties [1].

Density functional calculations with plane-wave basis sets were performed using the xTAPP code [2], where the ultrasoft pseudopotential and the generalized gradient approximation (GGA) of the exchange correlation potential were employed. The cutoff energies in the wavefunction and charge densities were 64 and 256 Ry, respectively, and the SOI was explicitly considered. To study the effects of SOI, we performed the usual GGA calculation and compared it with the result including the SOI. Below, we refer to the former as GGA and to the latter as SO-GGA. The atomic and lattice parameters were optimized with an 8×8×8 k-point sampling, and we found that SO-GGA reproduces the experimental crystal structure quite well. The Fermi-surface calculations were performed with the dense 21×21×63 k-point sampling to obtain the detailed surface structure [3]. Phonon calculations were performed using 11×11×11 k-point sampling for a 1×1×3 supercell [4].

Figure 1(a) shows our calculated band structure. To see the SOI effect, the SO-GGA band (thick red curves) is compared with the GGA band (thin blue curves) in Fig. 1(b). An appreciable difference can be observed in the low-energy bands; the GGA result exhibits metallic bands, particularly along the L-M or H-K lines. When the SOI is switched on, the metallic bands are split and a pocket-like band structure appears. The gap size due to the SOI is about 0.3 eV, which is comparable to the valence bandwidth 0.5 eV.

Figures 1(c) and 1(d) show the Fermi surfaces based on the SO-GGA and GGA, respectively. We see that the GGA Fermi surface is contributed from the two bands (indicated in dark-blue and bright-red colors), while the SO-GGA Fermi surface is basically formed by the one band; the SOI makes the bright-red colored GGA Fermi surface disappear. In the SO-GGA Fermi surface, since the SOI resolves the band degeneracy, the Fermi surfaces are seemingly two (dark-blue and bright-blue colored surfaces); however, these two are originated from the same band. Also, in the SO-GGA Fermi surface, we see a sheet structure along the c*-axis (the Γ-A line), which indicates a nesting trend along this direction. We note that the SOI is relevant to the narrowing of the sheet separation between the blue colored Fermi surfaces.

Figures 2(a) and 2(b) are our calculated phonon dispersions with and without SOI, respectively, and Fig. 2(c) is a comparison of two densities of states. Considering the SOI, the density of state is blue shifted as a whole, and a gap is formed around 10 THz. We found that phonon frequencies at the Γ point are in a good agreement with the Raman measurement.

As another achievement, we have released a new software RESPACK [5] that is a

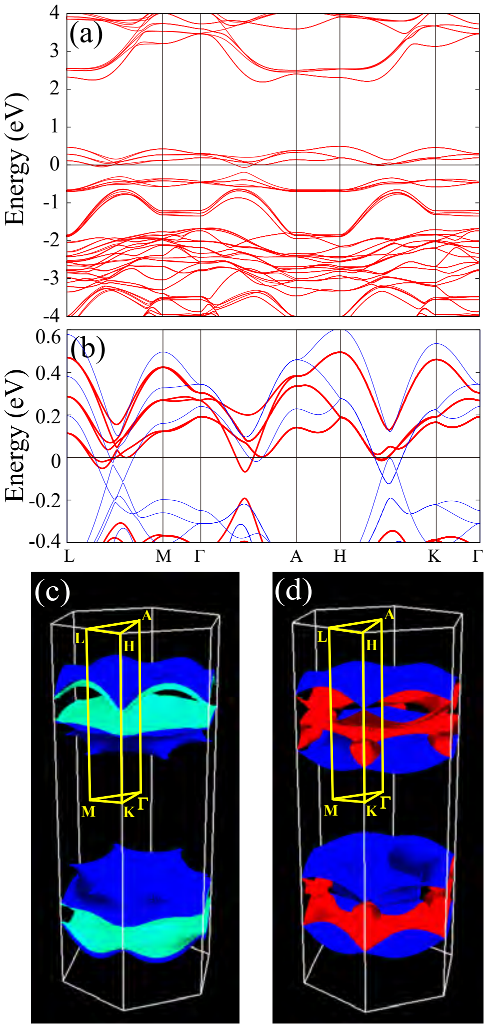

Figure 1: (Color online) (a) Ab initio electronic band structure considering the SOI in $Ca_5Ir_3O_{12}$. The energy zero is the Fermi level. (b) A zoom of the low-energy band structure, where the SO-GGA result (thick red curves) is compared with the usual GGA result (thin blue curve). (c) Calculated Fermi surface for SO-GGA and (d) GGA.

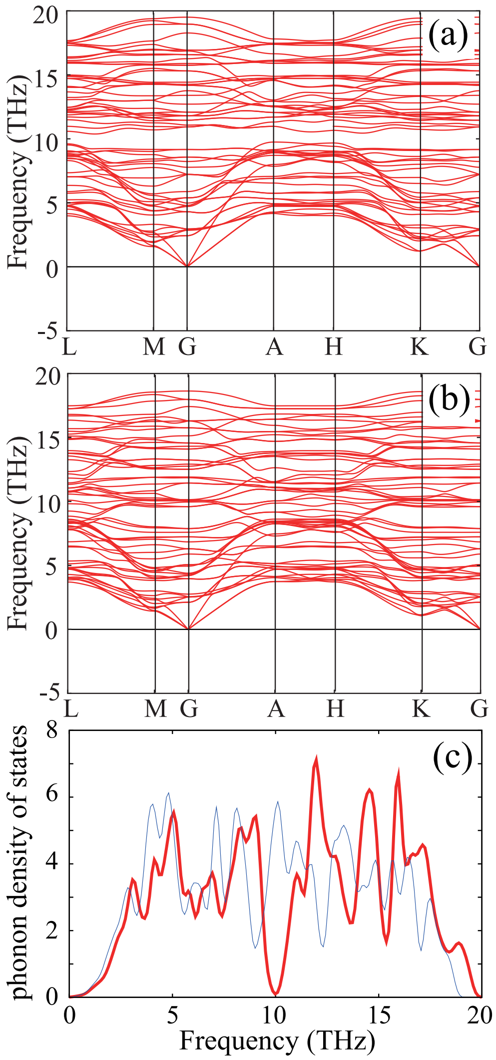

Figure 2: (Color online) (a) Ab initio phonon dispersion with the SOI in $Ca_5Ir_3O_{12}$. (b) The result without SOI. (c) Calculated phonon density of states, where the SO-GGA result (thick red curves) is compared with the usual GGA result (thin blue curve).

first-principles calculation program to evaluate the maximally localized Wannier functions, the RPA response functions, and frequency-dependent electronic interaction parameters.

References

[1] K. Matsuhira, K. Nakamura, Y. Yasukuni, Y. Yoshimoto, D. Hirai, Z. Hiroi: J. Phys. Soc. Jpn. **87** (2018) 013703.

[2] http://xtapp.cp.is.s.u-tokyo.ac.jp

[3] http://fermisurfer.osdn.jp

[4] https://atztogo.github.io/phonopy

[5] https://sites.google.com/view/kazuma7k6r

First-principles study of quantum transport in nanostructures

NOBUHIKO KOBAYASHI
Institute of Applied Physics, University of Tsukuba
1-1-1 Tennodai Tsukuba Ibaraki 305-8573

1 Introduction

An atomic-scale understanding of electron transport properties in materials is an important issue in materials science and nanotechnology. Theoretical investigations on transport properties are indispensable for the recent developments of high-performance electronic devices. Quantum nature is essential in nanoscale systems, and atomistic analysis based on detailed electronic states calculations are indispensable to discuss the transport property. In order to analyze transport properties, we have developed the nonequilibrium Green's function (NEGF) method, and the O(N) time dependent wave-packet diffusion (TD-WPD) method on the basis of the density functional theory (DFT). Using these methods, we have investigated charge, head and spin transport properties of materials. [1]

2 O(N) TD-WPD method and application to organic semiconductors

Organic semiconductors have attracted much attention for their applications to flexible, lightweight, and low-cost electronic devices. Organic semiconductors are crystals that are assemblies of π-conjugated molecules weakly bonded by van der Waals interactions, and single crystallization has been achieved, enhancing the mobility. It is now expected that the mechanism of carrier transport in organic semiconductors can be elucidated and that materials exhibiting high mobility can be developed by novel molecular synthesis.

We developed the O(N) TD-WPD method for the quantum transport calculation of huge systems of up to 100 million atoms a decade ago.We calculated the conductance and the mobility of the system with micron-order lengths at room temperature based on the Kubo-Greenwood formula. Using this method we can study the transport properties from diffusive to ballistic regimes including the effect of realistic electron-phonon scattering, and determine the mean free path and relaxation time from an atomistic viewpoint. We performed DFT calculations of electronic structures and interactions between molecules of single-crystal organic semiconductors including the effect of the van der Waals interaction, and applied the TD-WPD method to the analysis of transport properties of the organic semiconductors. We analyzed the transport properties of various organic semiconductors such as pentacene, rubrene, C8-BTBT, DNTT, and C10-DNBDT. We reveal the mobility and the temperature-dependent behavior from band-like to thermally activated behavior due to extrinsic disorder effects, which correspond to experimental observations.[2]

3 NEGF method and application to thermoelectricity

We have developed an efficient numerical calculation code for the ab-initio electron transport based on the DFT and NEGF formalism. We have applied the method to analyses of thermoelectricity of magnetic semiconductors.

Thermoelectric materials have attracted considerable attention from viewpoints not only of materials science but also of applications for energy harvesting by waste heat, and intensive works have been devoted to enhance conversion efficiency from thermal energy into

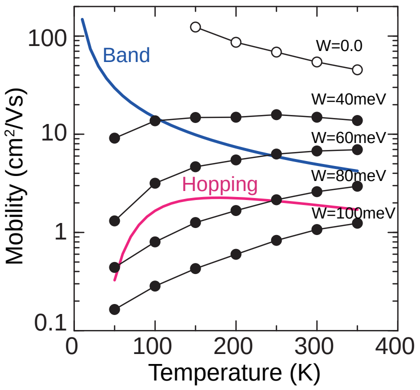

Figure 1: Calculated mobility of a pentacene single crystal along the a axis as a function of temperature for several magnitudes of static disorder W. [2]

electricity. The efficiency is expressed as a function of the figure of merit $ZT = \sigma S^2 T/\kappa$, where σ, S, κ and T are the electrical conductivity, the Seebeck coefficient, the thermal conductivity and the temperature, respectively, and the thermoelectric power factor is written as σS^2. Enhancement of thermoelectric efficiency is not an easy task since the Seebeck coefficient, the electrical conductivity, and the thermal conductivity are not independent of each other. There is the trade-off between σ and S, and materials with high electric conductivity tend to have high thermal conductivity.

We analyze the thermoelectric properties of a magnetic semiconductor CuFeS2 by NEGF-DFT. The electronic transport properties, Seebeck coefficient, and the figures of merit in doped compositions are estimated. The results show that they obtain their maximum values around the electronic band edge and suitable doping enhances the thermoelectric properties of CuFeS2. We theoretically demonstrate the enhancement in the figure of merit by doping, which is in agreement with experimental work, and show further enhancement by the optimized doping.[3, 4]

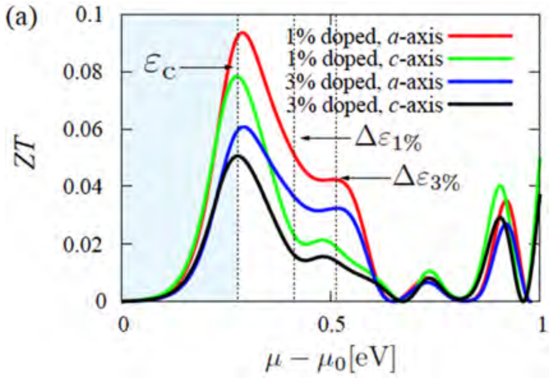

Figure 2: Figures of merit ZT of CuFeS2 as a function of the chemical potential at 300 K [4]

References

[1] N. Kobayashi, H. Ishii, K. Hirose, Jpn. J. Appl. Phys. (2018) in press.

[2] H.Ishii, N.Kobayashi, K.Hirose, Phys. Rev. B 95, 035433 (2017)

[3] H.Takaki, K.Kobayashi, M.Shimono, N.Kobayashi, K.Hirose, N.Tsujii, T.Mori, Appl. Phys. Lett. 110, 072107 (2017)

[4] H.Takaki, K.Kobayashi, M.Shimono, N.Kobayashi, K.Hirose, N.Tsujii, T.Mori, Materials Today Physics 3 85e92 (2017).

The Study on the Electronic State of Reduced Anatase TiO_2 Nanocrystal

Kenji YASUOKA
Department of Mechanical Engineering,
Keio University, Kohoku, Yokohama, Kanagawa 223-8522

TiO_2, a wide-gap semiconductor, have attracted considerable attention due to its potential applications as solar cell, photocatalysis and biocompatible materials.[1] Among three major polymorphs of TiO_2, rutile, anatase, and brookite, anatase is known to be the most favoured for photocatalytic reactions. Reactivity of anatase is known to be further enhanced by preparing it in a nanocrystalline structure. In the previous studies, both experimental and computational approach has been adopted clarify the underlying mechanism.[2] However the polaronic nature of excess electrons in TiO_2 made this difficult.

We have overcome this difficulty by adopting hybrid functional (HSE06) for exchange-correlation functional in density functional theory. More than 20 defect configurations were prepared and optimised using the HSE06 throughout the calculation. Adopting multi-leveled parallelisation, this calculation was performed on multiple computer nodes by taking advantages of the node-node data transmission technology such as the "enhanced hypercube" topology and 4× FDR InfiniBand 2× used in the System B.

As a result, different defect structure have shown different excess electron structures (Fig 1). These excess electrons formed polarons and created different band gap width according to their spatial distribution. This result indicates the possibility to tune the reactivity of TiO_2 nanocrystals through controlling the defect configurations.

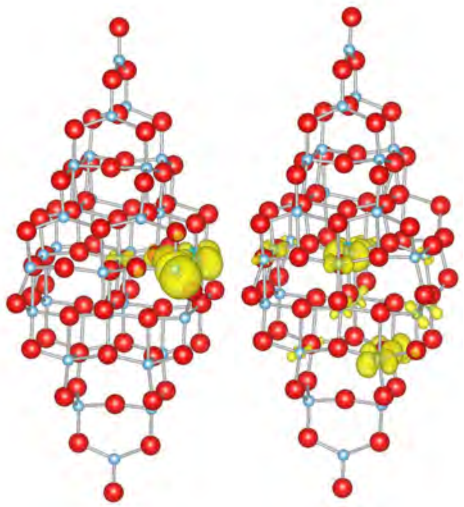

Fig. 1: Representative excess electron structures. (Left) Two excess electrons distributed in the close proximity (left) and apart (right) from each other.

References

[1] U. Diebold: Surf. Sci. Rep. **48** (2003) 53.

[2] K. Zhang and J. H. Park: J. Phys. Chem. Lett. **8** (2017) 199.

Structural transition analyses on nano- and bio-systems using dissimilarity

Yasuteru SHIGETA

Center for Computational Sciences,

University of Tsukuba, 1-1-1 Tennodai, Tsukuba, Ibaraki 305-8577

Several biological functions, such as molecular recognition, enzyme catalysis, signal transduction, allosteric regulation, and protein folding, are strongly related to conformational changes of proteins. These conformational changes are induced as slow dynamics upon collective motions, including biologically relevant large-amplitude fluctuations of proteins. Although molecular dynamics (MD) simulation has become a powerful tool for extracting conformational transitions of proteins, it might still be difficult to reach time scales of the biological functions, because the accessible time scales of MD simulations are far from biological time scales, even if straightforward conventional MD (CMD) simulations using massively parallel computers are employed. Thus, it is desirable to develop efficient methods to achieve canonical ensembles with low computational costs.

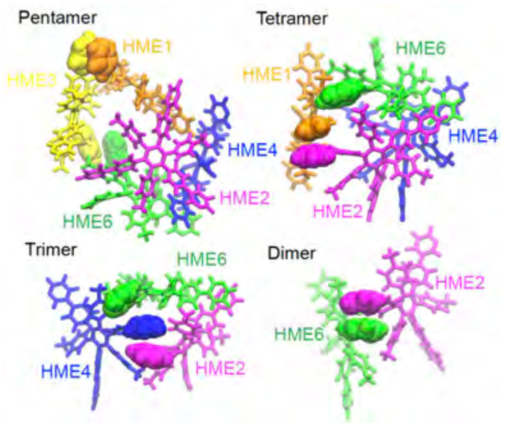

Figure 1. Representative oligomeric structures ($\mathbf{1}_n$: n=2-5) during a dissociation pathway of nanocube ($\mathbf{1}_6$) which consists of six gear-shaped amphiphile molecules (**1**).

For this aim, we have developed several enhanced conformational search techniques of biomolecules [1] and extended it to refer structural dissimilarity [2] to induce structural transitions of a given system by avoiding already sampled area. Our basic strategy is as follows: (i) selection of initial seeds (initial structures) for the conformational sampling in restarting MD simulations. Here, the seeds should be selected as candidates with the high potential to transit. (ii) Resampling from the selected seeds by initializing velocities in restarting short-time MD simulations [1]. A cycle of these simple protocols might drastically promote the conformational transitions of biomolecules.

By self-organization processes, six gear-shaped amphiphile molecules (**1**) form the hexameric structure of a nanocube ($\mathbf{1}_6$) [3]. Structural dissimilarity sampling (SDS) simulations [2] of $\mathbf{1}_6$ in a 25% aqueous methanol were conducted to extract dissociation pathway of $\mathbf{1}_6$ into monomers step-by-step as the reverse . Our MD study unveiled that a programed dynamic ordering exists in the dissociation processes of a nanocube. According to the dissociation processes, it is proposed that the triple π-stacking among three 3-pyridyl groups and CH-π or other hydrophobic interactions were sequentially formed at stable and transient oligomeric states in the self-organization processes, i.e. $\mathbf{1}_2$ (dimer), $\mathbf{1}_3$ (trimer), $\mathbf{1}_4$ (tetramer), and $\mathbf{1}_5$ (pentamer). By subsequent analyses on the stability of these oligomers, it was found that $\mathbf{1}_3$ and $\mathbf{1}_4$ are stable intermediate oligomers, whereas $\mathbf{1}_2$ or $\mathbf{1}_5$ are transient ones. Thus, the formations of $\mathbf{1}_3$ from three monomers and of $\mathbf{1}_6$ from $\mathbf{1}_4$ and two monomers via corresponding transients are time-consuming steps in forming the nanocube [4].

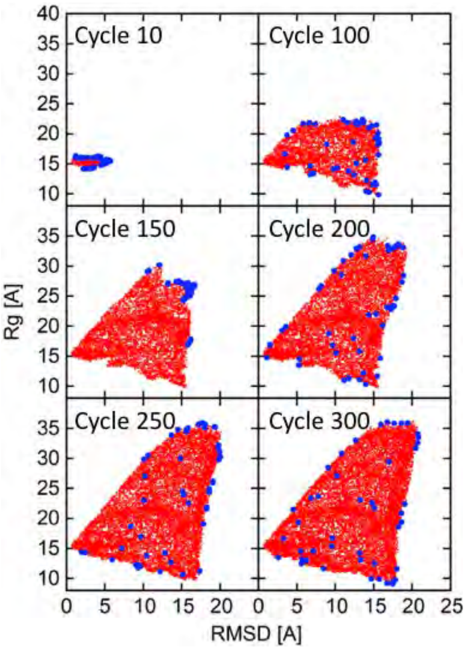

Figure 2 Accumulated trajectories mapped on to RMSD and R_g [Å] during dissimilarity sampling

We have also applied the dissimilarity sampling method to the dissociation of cytochrome *c* dimer [5]. As illustrated in Fig. 1, the sampled area spanned by root-mean-square deviation (RMSD) and a radius of gyration (R_g) spreads over. However, the dissociation of Cyt *c* dimer did not occur during 300 cycles. Although the sampled area were fully sampled as cycles of structure sampling went, our conformational sampling method fail to find the dissociation pathway of Cyt *c* dimer owing to improper choice of reaction coordinates (RCs). To remedy the drawback, we now try to choose the effective RCs automatically [6] to describe the dissociation pathway of Cyt *c* dimer.

References

[1] R. Harada, Y. Takano, T. Baba, Y. Shigeta: Phys. Chem. Chem. Phys. **17** (2015) 6155.

[2] R. Harada, Y. Shigeta: J. Chem. Theor. Compt. **13** (2017) 1411.

[3] S. Hiraoka, K. Harano, M. Shiro, M. Shionoya: *J. Am. Chem. Soc. 130 (***2008**) 14368.

[4] R. Harada, T. Mashiko, M. Tachikawa, S. Hiraoka, Y. Shigeta: Phys. Chem. Chem. Phys. in press.

[5] S. Hirota, Y. Hattori, S. Nagao, M. Taketa, H. Komori, H. Kamikubo, Z. Wang, I. Takahashi, S. Negi, Y. Sugiura, M. Kataoka, Y. Higuchi; *Proc. Nat. Acad. Sci. U.S.A.* **107** (2010)12854.

[6] R. Harada, Y. Shigeta: J. Chem. Theor. Compt. submitted.

First-Principles Calculation for Positron and Muon Experiments as Measurements of Crystals

Mineo SAITO

Institute of Science and Technology, Kanazawa University

Kakuma, Kanazawa, 920-1192 Japan

The spin-polarized positron annihilation technique is expected to be a useful tool to detect spin states in materials [1]. Analysis based on first-principles calculations is necessary to get useful information from experimental results. We study the positron annihilation in the Zn vacancy in ZnO that induces ferromagnetism.

We find that the vacancy has the C_{3v} symmetry and is spin polarized. The defect level E is found to be occupied by two electrons and we thus conclude that the electronic ground state belongs to $^3A_2$. Since the E state is partially occupied by electrons, the Jahn-Teller distortion of the E vibrational mode is expected to lower the symmetry and to lead to the spin singlet state. We however find that the Jahn-Teller energy is very small, thus the above mentioned spin triplet state is the most stable. The distance between nearest O atoms is found to be 3.60Å, which is much larger than the ideal one (3.31Å). This outward relaxation is expected to be the origin of the small Jahn-Teller effect and leads to the sp^2 like bond angle (117.3°). Therefore the spin density originates from the p-orbitals of O atoms as shown in Fig. 1. The calculated positron lifetimes for the majority (207ps) and minority (216ps) spins are found to be substantially different .

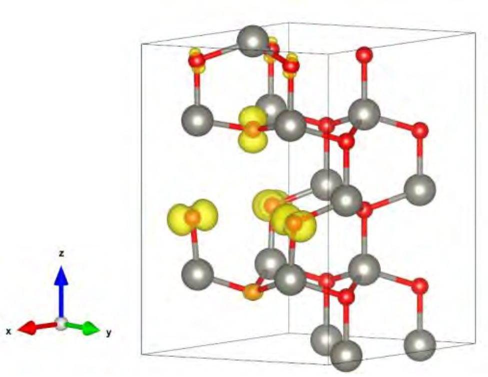

Fig. 1 Spin density of the Zn vacancy in ZnO.

We also study the Fermi contact term of muon in Si by using up to the 512 site supercell and find that a large unit supercell is necessary to obtain the converged result.

References

[1] M. Maekawa et al., Appl. Phys. Lett., 110, 172402 (2017).

Development and application of a new method for material structure prediction supported by experimental data

Shinji TSUNEYUKI

Department of Physics, School of Science,

The University of Tokyo, 7-3-1 Hongo, Bunkyo-Ku, Tokyo 113-0033

Institute for Solid State Physics,

The University of Tokyo, Kashiwa-no-ha, Kashiwa, Chiba 277-8581

Theoretical prediction of crystal structure from its chemical composition and physical conditions has been a long-standing problem of physical sciences [1]. There have been so many attempts in this direction and some of them have made a great success such as the prediction of high-temperature superconducting phases of sulfur hydride with the genetic algorithm [2] and the particle swarm optimization [3]. And yet the number of atoms in the unit cell reachable with these algorithms are limited, and we need to develop alternative approaches for theoretical prediction of new materials.

In this project, we are developing a method of structure prediction supported by experimental data. The method is designed to utilize powder diffraction data whose range of diffraction angle is limited by experimental setup or whose quality is insufficient for Rietveld analysis just like ultra-high-pressure experiments. In this method, instead of finding the global minimum of the multi-dimensional potential energy surface $E(\mathbf{R})$ as a function of the atomic positions **R**, we define the effective potential $F(\mathbf{R})$ defined as the sum of $E(\mathbf{R})$ and a penalty function which increases when the simulated diffraction pattern deviates from the experimental one:

$$F(\mathbf{R}) = E(\mathbf{R}) + \alpha N(1-\lambda),$$

$$\lambda = \sum_{\theta_{\mathrm{obs}}} I(\theta_{\mathrm{obs}}) \Big/ \int I(\theta)d\theta.$$

Here, $I(\theta)$ is the diffraction intensity of the simulated crystal and so is a function of **R**, N is the number of atoms in the simulation cell, and α is a control parameter. The sum and integral for so-called crystallinity λ are taken within the

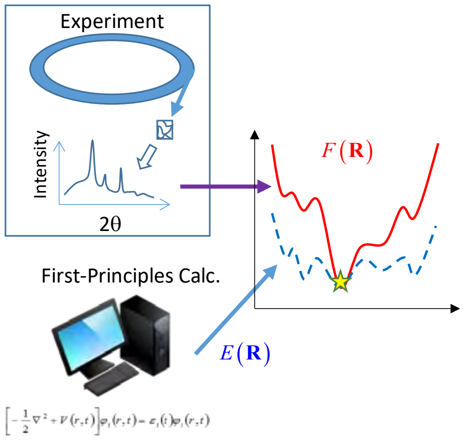

Fig.1 Schematic view of the data assimilation for the prediction of crystal structures with incomplete diffraction data.

range of the experimentally available diffraction angle θ, while θ_{obs} is the angle of each diffraction peak observed within the range. λ becomes unity when the simulated structure reproduces the experimentally observed diffraction data. The global minimum of $E(\mathbf{R})$ coincides with that of $F(\mathbf{R})$, while other local minima of $E(\mathbf{R})$ becomes less stable in $F(\mathbf{R})$ due to the penalty $\alpha N(1-\lambda)$ so that we can find the global minimum of $F(\mathbf{R})$ more easily.

We performed simulated annealing with the effective potential $F(\mathbf{R})$ for polymorphs of SiO_2 (low quartz, low cristobalite, coesite) and carbon (diamond, graphite) to find that each crystal structure can be obtained with high probability even if we use the diffraction data of a very limited range of $20° < \theta < 45°$ [4]. It should be noted that λ does not contain the information on the diffraction peak intensity except for the diffraction angle. It means that the method is robust against the noise and the preferred orientation effect which are often problematic when the sample for the diffractometry is small.

The present method is in a sense a realization of data assimilation in materials science. Data assimilation is often used in the simulation for the weather forecast, where the solution of the Navier-Stokes equation is adjusted to reproduce the temporal sequence of weather data at discrete observation points. In the present method, limited information on the diffraction angle helps the structure simulation. The same idea could be, in principle, applied to materials simulation with various experimental data such as the scanning tunneling microscope or the transmission electron microscope.

References

[1] J. Maddox, Nature 335, 201 (1988).

[2] D. Duan, Y. Liu, F. Tian, D. Li, X. Huang, Z. Zhao, H. Yu, B. Liu, W. Tian, and T. Cui, Sci. Rep. 4, 06968 (2014).

[3] Y. Li, J. Hao, H. Liu, Y. Li, and Y. Ma, J. Chem. Phys. 140, 174712 (2014).

[4] N. Tsujimoto, D. Adachi, R. Akashi, S. Todo and S. Tsuneyuki, to appear in Phys. Rev. Mat.

DFT studies on next-generation battery, solar cell and catalyst

Yoshitaka TATEYAMA

Center for Green Research on Energy and Environmental Materials (GREEN), National Institute for Materials Science (NIMS), 1-1 Namiki, Tsukuba, Ibaraki 305-0044; Elements Strategy Initiative for Catalysts & Batteries (ESICB), Kyoto University, Goryo-Ohara, Nishikyo-ku 615-8245.

We have addressed the mechanisms, and as well conducted materials search for next-generation batteries [1], solar cells [2] and catalysts [3], with cutting-edge DFT calculation techniques. In this report, we mainly describe the novel Na-excess cathodes for Na-ion batteries [1].

Increasing the capacity of Na ions batteries is a highly desired industrial goal. One possible way of achieving such an increase is evoking reversible oxygen redox that would add extra capacity to that of transition metal (TM) redox. To understand the atomistic origin of the O redox, we carried out a comprehensive density functional study of the electronic properties of the $R\bar{3}m$ Na_2RuO_3 (space group 166) and $R\bar{3}$ Na_1RuO_3 (space group 148) as shown in Figure 1. It was speculated that these compounds undergo reversible O redox which increases the capacity by 40% beyond the TM redox capacity to an impressive value of 180 mA.h/g. We then screened the full range of ternary $R\bar{3}$ compounds that consist of Na, O and *4d* transition metal (TM) elements in search for candidate compositions with higher electrochemical potential and larger capacity for sodium ion battery cathode applications.

Computationally, we treated the exchange-correlation functional with GGA+U formalism. U term was particularly fine-tuned to reproduce the electrochemical potential of Na extraction in the Na_xRuO_3 compound for which measurements exist. We found that U = 2 eV fulfils this criterion and moreover it produces an electronic structure that resembles the one obtained with higher level HSE03 functional.

We could reproduce theoretically the voltage plateaus detected in the Na_xRuO_3 cathode (x = 0.5–2) and demonstrate that O's significant participation in the redox reaction was the origin of the extra capacity that has been observed experimentally. We also found that O–O distance was maintained at ~2.5 Å during the desodiation process. Furthermore, our results regarding the survey of Na_1TMO3 compounds revealed that in descending order Na_1NbO_3, Na_1AgO_3, Na_1PdO_3 and Na_1RhO_3 had O populations of 4.94 e/O, 4.66 e/O, 2.10 e/O and 1.5 e/O near the Fermi level, respectively, all being higher than that of

Na$_1$RuO$_3$. Consequently, in all these compounds O's participation in the redox mechanism is predicted to be more prominent. The case of Na$_1$NbO$_3$ is particularly interesting as its high capacity originates entirely from reversible O redox as Nb adopts *d^0* configuration in this compound. Given the affordability of Nb metal and the robust stability of $R\bar{3}$ Na$_1$NbO$_3$ phase, we predict that Na$_1$NbO$_3$ is a prime candidate for Na ion battery applications.

In compounds with $R\bar{3}$ structure, the availability of O electrons for redox reaction originates from the local coordination environment. In these compounds, O ions are coordinated by two TM ions and two Na ions. Consequently, O under-coordination elevates some of un-hybridised or orphaned O *2p* states closer to the Fermi level and thus facilitates continuous O redox over a wide range of Na concentrations. Although this mechanism, to some extent, resembles the exclusive reversible O redox in 3d transition metal oxides, however, due to weaker localisation effects of *4d* transition metals, some TM–O hybridisation always exists. This hybridisation together with relatively large O–O separation prevents the detrimental O$_2$ evolution in these compounds.

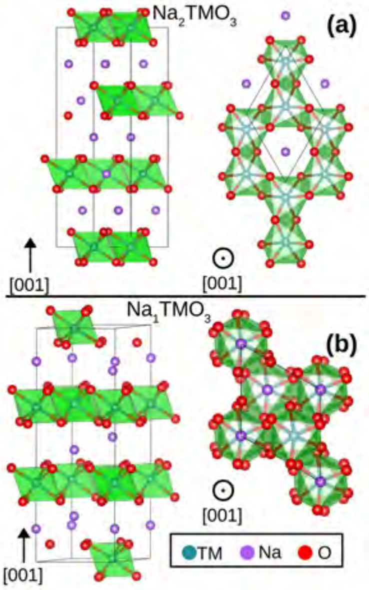

Fig. 1: The structures of surveyed Na$_x$TMO$_3$ Compounds. Space group 166 ($R\bar{3}m$) is presented in (a) while space group 148 ($R\bar{3}$) is presented in (b). Note the difference in Na content.

References

[1] M. H. N. Assadi, Masashi Okubo, Atsuo Yamada, Yoshitaka Tateyama, J. Mater. Chem. A 6, 3747-3753 (2018).

[2] Jun Haruyama, Keitato Sodeyama, Ikutaro Hamada, Liyuan Han, Yoshitaka Tateyama, J. Phys. Chem. Lett. 8, 5840-5847 (2017).

[3] Seiji Kasahara, Keisuke Natsui, Takeshi Watanabe, Yasuyuki Yokota, Yousoo Kim, Shota Iizuka, Yoshitaka Tateyama, Yasuaki Einaga, Anal. Chem. 89, 11341-11347 (2017).

.

Atomic structure and electromagnetic properties of oxide interfaces

Chunlin Chen[1], Deqiang Yin[1], Hongping Li[1], Kazutoshi Inoue[1], Yuichi Ikuhara[1,2]
[1]*Advanced Institute for Materials Research, Tohoku University, Sendai, Miyagi, 980-8577*
[2]*Institute of Engineering Innovation, The University of Tokyo, Yayoi, Tokyo, 113-8656*

Clarifying how the atomic structure of interfaces/boundaries in materials affects the electronic and magnetic properties is of fundamental interest in materials science. By combining atomistic first-principles calculations with atomic-resolution transmission electron microscopy (TEM), we systematically investigated the atomic structure and electromagnetic property of the perovskite-related $\mathrm{Sr}_n\mathrm{Nb}_n\mathrm{O}_{3n+2}$ compounds [1] and $\mathrm{Fe_3O_4}$ twin boundaries (TBs) [2]. We performed the density functional theory (DFT) calculations using the projector augmented wave (PAW) method as implemented within Vienna ab Initio Simulation Package (VASP) with the DFT+U formulation. The valence-electron wave functions were expanded in a plane wave basis with energies up to 400 eV. All of the atoms in the system were fully relaxed with the conjugate gradient algorithm until the magnitude of the Hellmann-Feynman force on each atom and the total energies converged to less than 0.05 eV/Å and 1.0×10^{-4} eV, respectively. The Brillouin zone integration was performed via the tetrahedron method with the Blöchl correction.

The physical origin has been unknown for the transition of electrical properties from the 3D isotropic conductivity in $\mathrm{SrNbO_3}$ to the quasi-1D metallic conductivity in $\mathrm{Sr}_n\mathrm{Nb}_n\mathrm{O}_{3n+2}$. The generalized gradient approximation (GGA) within the Perdew and Wang (PW91) scheme was employed to describe the exchange-correlation functional with an $8\times6\times2$ Monkhorst-Pack k-point grid. The effective Hubbard parameter ($U_{\text{eff}} = 7.8$ eV) was used to consider the effect of the localization of Nb-4d electrons. We have demonstrated that the local electrical conductivity in the $\mathrm{Sr}_n\mathrm{Nb}_n\mathrm{O}_{3n+2}$ compounds directly depended on the configuration of the $\mathrm{NbO_6}$ octahedra in local regions [1].

On the other hand, by combining atomistic spin-polarized first-principles calculations and atomic-resolution TEM with differential phase contrast imaging, we investigated the atomic and electronic structures of individual $\mathrm{Fe_3O_4}$ TBs to systematically determine their magnetic couplings. The Perdew-Burke-Ernzerh GGA schemewas employed with an $7\times5\times1$ Monkhorst-Pack k-point grid. The effective Hubbard parameter ($U_{\text{eff}} = 3.8$ eV) was used. The magnetic coupling across the $\mathrm{Fe_3O_4}$ TBs can be either antiferromagnetic or ferromagnetic, which directly depends on the TB atomic core structures and resultant electronic structures within a few atomic layers [2].

References

[1] C. Chen, D. Yin, K. Inoue, F. Lichtenberg, X. Ma, Y. Ikuhara, J. G. Bednorz: ACS Nano **11** (2017) 12519.

[2] C. Chen, H. Li, T. Seki, D. Yin, G. Sanchez-Santolino, K. Inoue, N. Shibata, Y. Ikuhara: ACS Nano **12** (2018) 2662.

Development & Application of Rational Drug Design using the Forth Innovation Methodology

Yuta Yamamoto[1], Shogo Nakano[2], and Hiroaki Tokiwa[1]

[1]Rikkyo University, 3-34-1 Nishi-Ikebukuro, Toshima, Tokyo 171-8501

[2]University of Shizuoka, 52-1 Yada, Suruga-ku, Shizuoka 422-8526

We have identified a short chain dehydrogenase like l-threonine 3-dehydrogenase (SDR-TDH) from metagenome data (mtTDH) by database mining based on the forth innovation methodology. Its enzymatic properties suggested that mtTDH has unique characteristics relative to other SDR-TDHs, including two mesophilic and thermophilic SDR-TDHs identified in this study. The activation energy of mtTDH was the lowest of those of the SDR-TDHs, indicating that it is a psychrophilic enzyme. Size-exclusion chromatography analysis revealed mtTDH is a monomer. We could also determine crystal structures of mtTDH in apo, binary, and two ternary complexes (L-Ser- and L-Thr-soaked forms) at resolutions of 1.25–1.9 Å.[1] *Ab initio* computational analysis using the fragment molecular orbital (FMO) calculations and the molecular dynamics (MD) simulation revealed the molecular mechanism of switching between the open and closed states induced by substrate binding and product release. We used the programs PAICS and AMBER14 for the FMO and MD calculations, respectively. Furthermore, six residues and two water molecules at the active site contributing to product release were assigned. The residues could be categorized into two groups on the basis of the enzymatic properties of their variants. The former group appeared to affect L-Thr dehydrogenation directly, because the K_{cat} value of their variants was >80-fold lower than that of wild-type mtTDH. On the other hand, the latter group contributes to switching between the open and closed states, which is important for the high substrate specificity of SDR-TDH for l-Thr: the K_{cat} and K_{m} toward L-Thr values of variants in these residues could not be determined because the initial velocity was unsaturated at high concentrations of L-Thr. On the basis of these findings, we proposed a product release mechanism for SDR-TDH associated with specific structural changes.

References

[1] T. Motoyama, S. Nakano, Y. Yamamoto, H. Tokiwa, Y. Asano, and S. Ito, *Biochemistry,* **56(43)**, 5758-5770 (2017)

DOI: 10.1021/acs.biochem.7b00832.

Development of High-performance Perfluoro Polymer Electret

Seonwoo KIM and Yuji SUZUKI
Department of Mechanical Engineering, The University of Tokyo
Hongo, Bunkyo-ku, Tokyo 113-8656

Electret is a dielectric with quasi-permanent charge. The charges trapped in proper electret materials can be stably stored and able to generate an external electrostatic field for tens of years. In recent years, a vibration-driven electret energy harvester attracts much attention, because it can convert ambient low-frequency vibration into electricity. High-performance electret materials have been desired, since the maximum power output of electret energy harvester is proportional to the electret surface potential squared [1]. Also, long-term stability of trapped charge determines the lifespan of the device. Although high-performance electrets have been reported in recent years [2], they are discovered from experimental trials, while its properties were unpredicted. In order to develop a new high-performance electret, it is necessary to understand underlying physics.

In the present study, we made numerical simulations to understand electron trapping phenomenon in polymer electrets using quantum mechanical analysis. An amorphous polymer electret CYTOP (AGC Co., Ltd) is mainly assumed, focusing on the electron trap site and the trap energy for different end groups.

Density functional theory with long-range correction (LC-DFT) calculation is adopted to analyze the electronic state of CYTOP molecules. The LC-BLYP density functional is used to solve Kohn-Sham equation with 6-31+g* basis sets. Three types of CYTOP with different end group are studied as shown in Fig. 1; CTL-S has trifluoromethyl end, CTL-A has carboxyl end, and CTL-M has amidosyl end. Conventionally-used bulk polymer electrets (PE, ETFE, PTFE) are also analyzed for comparison. Fig. 2 shows distribution of electrons trapped in electret tetramers. The electron trapped in PE does not lie on the structure, showing the molecule is electrophobic. On the other hand, clear electrophilicity can be found in fluorine-rich part of ETFE and PTFE. For CYTOP molecules, the trapped electron populates near

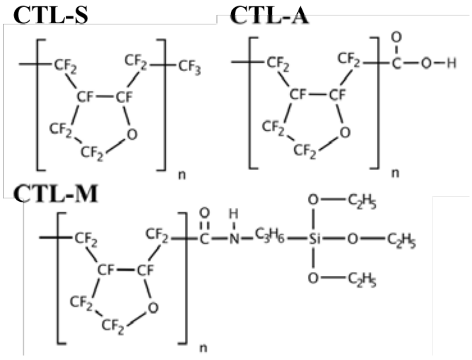

Fig 1. Chemical structure of CYTOP polymers

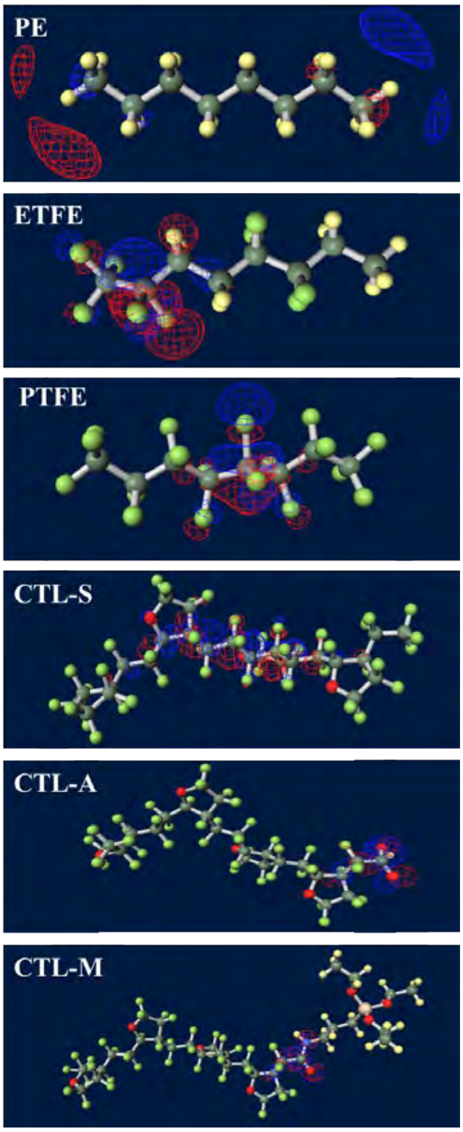

Fig 2. Distribution of trapped electron in electret tetramers (Green: fluorine, Blue: nitrogen, Red: oxygen, Khaki: carbon, Yellow: hydrogen, Pink: silicon)

end group (-COOH of CTL-A and -CONH of CTL-M), implying that the end group attracts the electron even more than perfluorinated back-bone structure itself. The orbital energies of each molecules are calculated. The energy of orbital where the electron is trapped is used to estimate the electron affinity (EA) following Koopmans' theorem. Calculated EAs have order as follows: CTL-M (5.83 eV) > CTL-A (4.7 eV) > CTL-S (4.39 eV) > PTFE (3.56 eV) > ETFE (3.02 eV) > PE (-1.93 eV). Acquired EAs of CYTOP make qualitative agreement with the thermally stimulated discharge (TSD) current peaks [2]. Note that the order of PE, ETFE, PTFE is also in accordance with that of TSD peaks. However, their trap energy cannot be fully described by present simulation because their performance as electret depends on not only by its single molecular EA but also by their morphology. Although our analysis on single molecule cannot perfectly interpret the real system of electret, we expect our method can be used as an indicator to predict performance of amorphous polymer electrets.

The computation is performed with SGI ICE XA ISSP system B F4cpu nodes, using quantum mechanical simulation package NWChem [3]. Every computation was held with 4 nodes (96 CPUs). In case of CYTOP tetramers, the calculation cost was approximately 9200 hours of CPU time for each case. For PE, ETFE and PTFE, 7000 hours of CPU time was necessary in total.

References

[1] Y. Suzuki: IEEJ Trans. Electr. Electron. Eng. 6 101–11

[2] K. Kashiwagi et al.: J. Micromech. Microeng. **21** (2011) 125016.

[3] M. Valiev et al.: Comput. Phys. Commun. **181** (2010) 147.

Singlet-triplet splitting of thermally activated delayed fluorescence molecules

Yoshifumi NOGUCHI

Department of Applied Chemistry and Biochemical Engineering, Graduate School of Engineering, Shizuoka University, Johoku 3-5-1, Hamamatsu, Shizuoka 432-8561, Japan

Thermally activated delayed fluorescence (TADF) in which triplet exciton transits to higher energy singlet exciton via a reverse intersystem crossing (RISC) is a key mechanism to achieve high efficiency in third generation organic light-emitting diodes (OLEDs) [1]. TADF molecules with nearly zero energy difference between the singlet and triplet excitons or singlet-triplet splitting (Δ^{ST}) are required for RISC. A great deal of efforts have been invested in the experimental cycle involving design → synthesizing → measurement to detect *good* TADF molecules. Although certain some simulations within the time-dependent density functional theory (TDDFT) have been applied to TADF molecules for the purpose of reducing the experimental effort, the theoretical attempts have been hampered by the peculiarity of TADF molecules of which the charge transfer excitation occurs in small-middle molecules size. That is, conventional functionals such as the (semi-)local and range-separation type functionals fail to describe the optical properties of TADF molecules. In addition, according to Ref. [2], in case that the hybrid functional is used, the mixing parameters should be optimized individually for each molecule and for singlet and triplet excitations.

In this study, we proposed an efficient computational method capable of simulating accurate Δ^{ST} in TADF molecules within the available computational facilities from first-principles. Our method evaluates Δ^{ST} as an expectation value of bare exchange Coulomb interaction, $< i|2v^{ex}|i >$, where $|i >$ is the exciton wave function ($= \sum_{e,h} A^{i}_{e,h} \psi_e(r_1)\psi^{*}_h(r_h)$) at the i-th exciton level [3]. We applied it to eighteen TADF molecules composed of 30-110 atoms, and confirmed that our method is sufficiently accurate for Rydberg and charge transfer-type excitons and slightly less accurate for local excitons [4].

References

[1] H. Uoyama, et. al.: Nature **492**, 234 (2012).

[2] S. Huang, et. al.: J. Chem. Theory Compt., **9** 3872 (2013).

[3] D. Hirose, Y. Noguchi, and O. Sugino: J. Chem. Phys. **146** (2017) 044303.

[4] Y. Noguchi and O. Sugino: J. Phys. Chem. C. **121** 20687 (2017).

Reduction of Rare Metals in Fuel Cell Catalysts and Hydrogen Permeable Membrane

Yuji KUNISADA
Center for Advanced Research of Energy and Materials, Faculty of Engineering,
Hokkaido University, Sapporo, Hokkaido 060-8628

We investigated the catalyst atom adsorption and diffusion properties on non-metal element doped graphene and hydrogen adsorption and diffusion properties on the surfaces and in the interfaces of ceramic materials, with the aid of the first principles calculation based on the density functional theory (DFT).

At first, we investigated adsorption and diffusion properties of Pt and Fe atoms on non-metal element doped graphene. We performed the total energy and electronic structure calculations using The Vienna Ab initio simulation package (VASP). We installed parallelized VASP with Intel® MPI Library and Intel® Math Kernel Library. We found that the adsorption energies of both Pt and Fe atoms increase by non-metal element doping into graphene lattice. From the electronic structure analysis, we revealed that Pt atoms form covalent bonds with graphene, while Fe atoms adsorb on graphene with the attractive Coulomb interaction. We also calculated the dopant dependence of diffusion properties of Pt and Fe atoms. From these calculations, we found that the non-metal dopants in graphene can prevent the surface diffusion of Pt and Fe atoms.[1,2]

We also investigated the hydrogen adsorption and diffusion properties on the surfaces and in the interfaces of TiN and HfN. We found that the nanocrystalline TiN and HfN membrane show high hydrogen permeability from experiments. We revealed that hydrogen atoms become hydride ions on surfaces and in interfaces of these materials using DFT calculations. [3,4]

References

[1] S. Hasegawa, Y. Kunisada, N. Sakaguchi: J. Phys. Chem. C 121 (2017) 17787.

[2] S. Hasegawa, Y. Kunisada, N. Sakaguchi: e-J. Surf. Sci. Nanotech. accepted.

[3] C. Kura, Y. Kunisada, E. Tsuji, C. Zhu, Hi. Habazaki, S. Nagata, M. Patrick Müller, R. A. De Souza, Y. Aoki: Nat. Ener. 2 (2017) 786.

[4] C. Kura, S. Fujimoto, Y. Kunisada, D. Kowalski, E. Tsuji, C. Zhu, H. Habazaki, Y. Aoki: J. Mater. Chem. A 6 (2018) 2730.

First-principles calculations of magnetic ultrathin films on surfaces

Yoshihiro GOHDA
Department of Materials Science and Engineering, Tokyo Institute of Technology
J1-3, Nagatsuta-cho 4259, Midori-ku, Yokohama 226-8502, Japan

Low-dimensional ferromagnetic nanostructures are of fundamental interest. However, ferromagnetism in realistic two-dimensional atomic structures is quite rare, because any finite-temperature magnetic order is prohibited for the isotropic two-dimensional Heisenberg model due to the Mermin-Wagner theorem. In addition, the stability of ferromagnetism in two-dimensional ferromagnetic structures is partially due to the surface magnetic anisotropy. Therefore, it is important not only to examine the magnetic order of the groud state, but also to analyze the magnetic anisotropy. Even though MnN monolayer films on Cu(001) have been reported to have an antiferromagnetic order [1], monolayer films of Mn compounds exhibiting the ferromagnetism have not been reported.

In this study, we demonstrate ferromagnetism in new two-dimensional strcutures on nonmagnetic transition-metal (TM) surfaces [2]. First-principles calculations were performed on the basis of density functional theory with the generalized gradient approximation by the OpenMX code [3]. We have found that MnB/TM(001) and MnC/TM(001) are ferromagnetic, whereas MnN/TM(001) is antiferromagnetic, irrespective of the kind of TM we studied. In Fig. 1, we show the calculated partial density of states (PDOS) of the Mn 3*d* states in MnB/Ag(001). The high PDOS of the nonmagnetic state at the Fermi energy ε_F is avoided by the exchange splitting in the ferromagnetic state, which is the characteristic of the itinerant ferromagnetism. With the detailed analysis, we have identified the ferromagnetism in MnB/TM(001) and MnC/TM(001) comes from the double-exchange mechanism, whereas the antiferromagnetism in MnN/TM(001) originates from the superexchange. We also investigated the local magnetic anisotropy energy using second-order perturbation theory [2, 4]. We have clarified the main contributions to the in-plane anisotropy in MnB/Pd(001) as hybridization between Mn and Pd states.

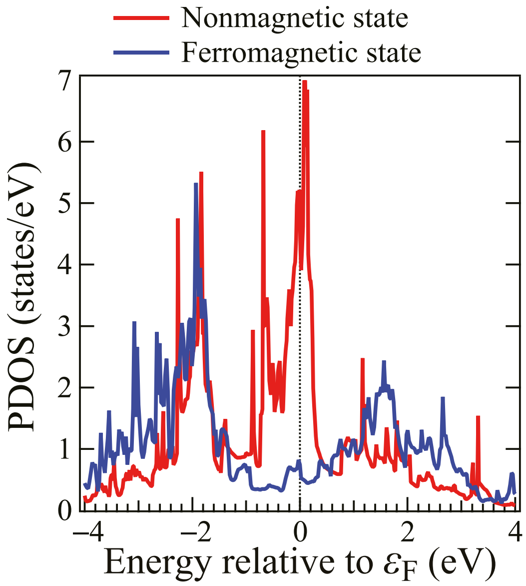

Figure 1: The calculated PDOS of the Mn 3*d* states in MnB/Ag(001) for the nonmagnetic state as well as the ferromagnetic state plotted as the summation of the majority- and minority-spin states.

[1] X. D. Liu, B. Lu, T. Iimori, K. Nakatsuji, and F. Komori, Phys. Rev. Lett. **98**, 066103 (2007); K. Nakatsuji, S. Nakamura, T. Tanaka, Y. Gohda, *et al.*, in preparation.

[2] S. Nakamura and Y. Gohda, Phys. Rev. B **96**, 245416 (2017).

[3] T. Ozaki, Phys. Rev. B. **67**, 155108 (2003).

[4] Z. Torbatian, T. Ozaki, S. Tsuneyuki, and Y. Gohda, Appl. Phys. Lett. **104**, 242403 (2014).

First-Principles DFT Calculations for Transition-Metal Oxides

Kunihiko YAMAUCHI
ISIR-SANKEN, Osaka University, Ibaraki, Osaka 567-0047

Transition-metal oxides show fascinating physical properties such as high temperature superconductivity, magnetism, ferroelectricity and even topological property. As aiming at finding novel multifunctional materials, we have explored spin-crossover phenomenon in $LaCoO_3$-related system. In $LaCoO_3$, Co^{3+} (d^6) ion shows the low-spin state (S=0) at the ground state in the rhombohedral structure. On the other hand, it has been reported that Co ion shows intermediate spin state (S=1) when the uniaxial pressure is applied. In order to understand the relation between Co spin state and the structural distortion, we first analyzed the phonon modes of the distorted crystal structure with respect to the ideal cubic perovskite structure via group theory. Then the electronic structure and the Co spin state were calculated under the several distortion modes via first-principles approach. Finally, we found that intimidate spin state can be invoked by combination between two modes, i.e., R_3^- mode which induces cooperative Jahn-Teller distortion and Γ_3^+ mode which modulates c/a ratio. The resulted distortion stabilizes the orbital ordering of Co e_g electrons as shown in Fig.1.

We also studied the electronic states in iridiates. Among them, Na_4IrO_4 exhibits unusual square planar coordination of IrO_4. In the square planar crystal field, Ir 5d state adopts an intermediate spin state as leading to the strong single-site anisotropy.[1] Here, spin-orbit coupling plays a minor role in shaping the electronic structure, but leads to strong magnetocrystalline anisotropy.

Some of iridates are known to show the "$J_{\rm eff}$=1/2" Mott insulating state. In order to explore the metal-insulator transition, rutile-based IrO_2/TiO_2 superlattices were theoretically designed. The heterostructure exhibit a thickness-controlled metal-to-insulator transition, crucially related to the connectivity among IrO_6 octahedra.

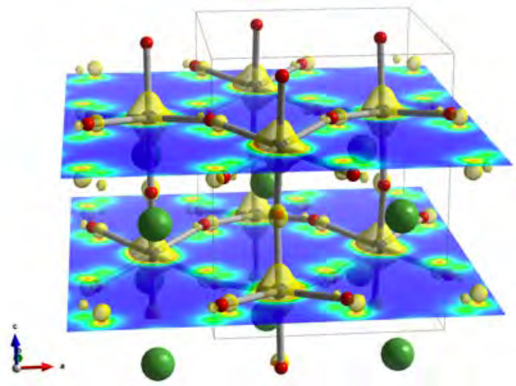

Figure 1: Orbital ordering of Co e_g state with intermediate spin state in monoclinic $LaCoO_3$.

References

[1] Xing Ming, Carmine Autieri, Kunihiko Yamauchi, and Silvia Picozzi, Phys. Rev. B **96**, 205158 (2017).

[2] Xing Ming, Kunihiko Yamauchi, Tamio Oguchi, Silvia Picozzi, arXiv:1702.04408 (2017).

Large scale ab initio calculations on the fundamental processes of solar energy convergence devices and on designing principles for new materials

Koichi YAMASHITA

Department of Chemical System Engineering, School of Engineering,
The University of Tokyo, 7-3-1, Hongo, Bunkyo-ku, Tokyo 113-8656

Water-splitting photocatalyst materials are required to have suitable band positions, band gap, and carrier effective masses. Recently, arrangements of N^{3-} and O^{2-} anions in perovskite-type oxynitride crystals, i.e., anion ordering, have been found to be specific and controllable, but further discussions are required to show guidelines to tune electronic properties by anion ordering. Thus, we aim to clarify the relationship between the anion ordering and perovskite oxynitride band structures by means of first-principles calculations.

We performed density-functional theory (DFT) calculations of electronic properties of $MgTaO_2N$ by Vienna ab-initio simulation package (VASP) to discuss its applicability to water-splitting photocatalyst, in consideration of such structural factors as octahedral tilting, anion ordering, and the interplay between perovskite and ilmenite polymorphs. Most of the configurations of the perovskite-type $MgTaO_2N$ were more suitable for water-splitting than ilmenite-type $MgTaO_2N$ polymorphs due to their favorable band edge position and effective masses (Figure 1). We found the strong correlation between the conduction band structures and octahedral tilting—configurations with more tilted octahedra had larger overlap between Ta-5d and anion-2p bands, resulting in bandgap opening and band dispersion reduction. There-fore, reducing octahedral tilting (e.g. via A-site doping) is highly desirable in the perovskite-type $MgTaO_2N$ material design for photocatalytic applications [1].

We have also studied organic-inorganic hybrid perovskite (OIHP) solar cells, namely lead halide perovskites ($APbX_3$: A and X are a monovalent cation and a halogen, respectively). OIHP solar cells are attracting much interest for their high photoconversion efficiency, but it is not sufficiently understood why OIHP has such remarkable properties.

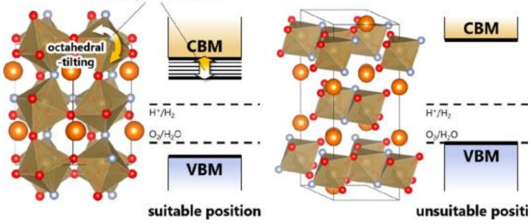

Figure 1: Schematic illustration of structures and band edge positions of perovskite- and ilmenite-type $MgTaO_2N$. Reprinted from [1].

We already investigated charge carrier trapping at defects on surfaces or grain boundaries, and proposed that moderate condition—the balance between Pb-rich and I-rich ones—is the best choice in terms of the defect formation energies [2]. In this year we approached the origin of high charge separation efficiency of OIHPs by DFT calculations and ab initio molecular dynamics simulations implemented in VASP, which revealed that inorganic frame dynamics induced charge separation [3]. We investigated lead iodide perovskites, $APbI_3$ (A is methyl ammonium, formamidinium, guanidinium, or cesium; in descending order of dipole moment), under two conditions: inorganic frames were fixed or all atoms moved (type I and II, respectively). We calculated the overlap integrals of valence band maxima (VBM) and conduction band minima (CBM), which revealed that type II condition tended to have less overlap integrals independently of A-site cations. Then we evaluated electrostatic potentials contributed by holes and electrons at VBM and CBM levels, respectively, which revealed that the overlap integrals and the potentials were highly correlated, and that the total potentials were dominantly governed by inorganic frames.

References

[1] A. Kubo, G. Giorgi, and K. Yamashita: J. Phys. Chem. C **121** (2017) 27813–27821.

[2] H. Uratani and K. Yamashita: J. Phys. Chem. Lett. **8** (2017) 742–746.

[3] H. Uratani and K. Yamashita: J. Phys. Chem. C **121** (2017) 26648–26654.

Theoretical studies on the energy storage materials

Atsuo YAMADA
Department of Chemical System Engineering,
The University of Tokyo, Hongo, Bunkyo-ku, Tokyo 113-8656

Pseudocapacitive energy storage at the electrochemical double layer can provide efficient devices to allow huge power and excellent reversibility. RuO_2 is one of the benchmarking materials that has been widely studied. It utilizes the fast redox reaction of Ru accompanied by the electroadsorption of protons,

$$RuO_a(OH)_b + \delta H^+ + \delta e^- \leftrightarrows RuO_{a-d}(OH)_{b+d}$$

However, detailed analysis of the reactions has not yet been achieved either theoretically or experimentally due to a lack of structural information on electrochemical interface. Recently structures of RuO_2/water interface were first provided using a theoretical scheme that considers the effects of electrode potential and pH [1]. In the present study, based on the provided structures, charge storage mechanism was calculated as a function of electrode potential at fixed pH = 0 to analyze the electron orbitals contributing to the pseudocapacitive reaction.

We demonstrated the extensive and unique contribution of oxygen orbitals at specific surface sites to pseudocapacitive reactions depending on the electrode potential. In potential region between −0.5 V and −0.1 V vs. RHE where averaged formal valence of surface Ru changes from Ru(III) to Ru(IV), Bader charge changes of Ru and O atoms at br sites are +0.52e, +0.26e. Moreover, in the higher potential region between 1.1 V and 1.5 V vs. RHE where averaged formal valence of surface Ru changes from Ru(IV) to Ru(V), Bader charge changes of Ru and O atoms at cus sites are 0.32e and 0.65e. Surprisingly large contributions of O 2p orbitals are observed; more of the electrons are extracted from O rather than Ru [2].

All the calculations were performed using GPAW code together with GGA/RPBE functional and PAW method. The k-points were sampled using a (4 × 4 × 1) mesh and electronic structures were calculated by thefinite difference method with a grid parameter of 0.20 ± 0.01 Å.

References

[1] E. Watanabe et al : *J. Phys. Chem. C.* **120** (2016) 8096.

[2] E. Watanabe, H. Ushiyama, K. Yamashita, Y. Morikawa, D. Asakura, M. Okubo and A. Yamada: *J. Phys. Chem. C.* **121** (2017) 18975

Prediction of properties of organic ferroelectrics and piezoelectrics by first-principles calculation

Shoji ISHIBASHI
Research Center for Computational Design of Advanced Functional Materials (CD-FMat),
National Institute of Advanced Industrial Science and Technology (AIST)
Tsukuba, Ibaraki 305-8565

Organic ferroelectrics and piezoelectrics are promising materials since they contain neither toxic nor rare elements. In addition, they are flexible and printable. Recently, we have experimentally found that organic antiferroelectrics undergo the antiferroelectric-to-ferroelectric transition by applying a electric field for squaric acid (SQA), [H-55dmbp][Hca] (55dmbp = 5,5'-dimethyl-2,2'-bipyridine; H2ca = chloranilic acid) [1], and 2-Trifluoromethylnaphthimidazole (TFMNI) [2]. Usually, an antiferroelectric consists of two sublattices oppositely polarized. We evaluated the total polarization values for ferroelectric SQA and [H-55dmbp][Hca] by calculating polarization of one sublattice and doubling it for each compound. We used the experimentally obtained sublattice structures for the antiferroelectric phases. As for the hydrogen positions, they were computationally optimized. The obtained polarization values are in good agreement with the experimental results [1]. As for TFMNI, the crystal structure of the ferroelectric phase under a electric field has been successfully obtained [2]. We evaluated the spontaneous polarization using the experimental structure of the ferroelectric phase with the hydrogen positions computationally optimized. The obtained value is in good agreement with the experimental result.

The above calculations have been done with the GGA-PBE functional on the experimental structures with only the hydrogen positions computationally optimized. For SQA, we have tried to optimize computationally the whole of the crystal structure. In addition to the standard LDA and GGA-PBE functionals, we applied the vdW-DF-cx and rvv10 functionals, which are recent versions of the van der Waals DFT. Among the four functionals, the rvv10 reproduces the low-temperature structure of SQA best. We, therefore, applied the rvv10 for further calculations. By computationally applying a electric field, we have succeeded in simulating the antiferroelectric-to-ferroelectric transition in SQA [3]. Depending on the electric-field direction, two different ferroelectric phases have been obtained. One of them is thought to correspond to the experimentally-obtained phase [1] while the other is yet to be experimentally confirmed.

We utilized the System B of the Supercomputer Center, the Institute for Solid State Physics, the University of Tokyo for some calculations.

References

[1] S. Horiuchi, R. Kumai, and S. Ishibashi: Chem. Sci. **9** (2018) 425.

[2] K. Kobayashi, S. Horiuchi, S. Ishibashi, Y. Murakami, and R. Kumai: J. Am. Chem. Soc. **140** (2018) 3842.

[3] S. Ishibashi, S. Horiuchi, and R. Kumai: submitted to Phys. Rev. B.

Large-scale computational simulations of non-equilibrium transport phenomena

Yoshihiro Asai, Marius Bürkle, Jun-ichi Ozaki
Research Center for Computational Design of Advanced Functional Materials,
National Institute of Advanced Industrial Science and Technology (AIST),
Central 2, Umezono 1-1-1, Tsukuba, Ibaraki 305-8568

We studied the following subjects in the non-equilibrium transport problem using large-scale computational simulations:

1-1) Thermoelectric transport (Electrons and Phonons) calculation based on the first-principles DFT calculations.
1-2) Comparing first-principles transport results with scanning tunneling microscope break junction measurements of molecular devices.
1-3) The resistive switching mechanism and the topological physics of GeTe–Sb_2Te_3 interfacial phase change memory material are discussed based on the first-principles DFT calculations.
2-1) Time-dependent density matrix renormalization group study of the electric conductance of strongly correlated Hubbard chain.
3-1) Electronic properties of silicon-based nanocrystals in the quantum confinement regime.

In the following we outline these subjects and give the main results:

1-1) Ballistic electron and phonon transport calculations for metallic nano-contacts. We studied the difference of the thermoelectric transport properties for mono and multi-valent metals investigating the validity of the Wiedemann-Franz law in the quantum transport regime. We can show that depending on conformation and type of metal violations of the Wiedemann-Franz law can be up to 20%, even in the Ballistic regime and without significant phonon contribution.【1】

1-2) Using accurate first-principle (DFT+$\sum$) based calculations we investigate the gate-dependence of the transport properties for different isomers of molecular conductors. This enables us to probe the transmission properties locally in energy space. Our first-principles results are used to elucidate the corresponding results experimental findings which show a clear dependence of the transport properties on the gate voltage.【2】

1-3) The first-principles calculations of the current voltage characteristic of the possible 'on' and 'off' states of the GeTe–Sb2Te3 interfacial phase change memory (iPCM) material were used to identify the memory mechanism. The spectrum function in the channel area and the transmission probability function were used to discuss the important wave number for the memory as well as the role played by the topological physics.【3】

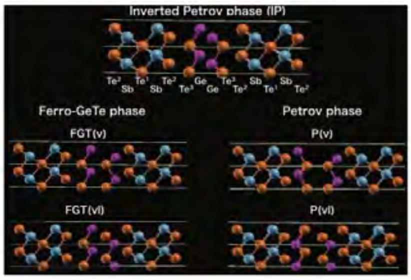

Fig.1 Model structure of the iPCM memory device material.

2-1) The time-dependent density matrix renormalization group【4】was used to discuss the length dependent conductance of the Hubbard chain. The contact effect is included the calculation, otherwise not included previously in the Tomonaga-Luttinger liquid (TLL) based theory. Unlike the TLL based theory predicting the perfect transmission leading to the unit conductance $G_0=2e^2/h$ in the infinite chain limit of the strong correlation regime, our calculation predicts a non-perfect transmission there, which we obtain after the damped oscillation in the finite length region.【5】 We presume it being due to the inelastic component of the strong Coulomb repulsion and the renormalization of the single particle energy.

3-1) Nanocrystals in the quantum confinement regime are a promising candidates for third generation solar cells as they allow to tune their band-gap over a wide range. The gap can be tailored by an appropriate combination of size and surface functionalization. Using first-principles calculations and a quasi-band structure approach we mapped the band-gap of silicon nanocrystals as shown in Fig.2. Our theoretical predictions have been confirm by experiment.【6】

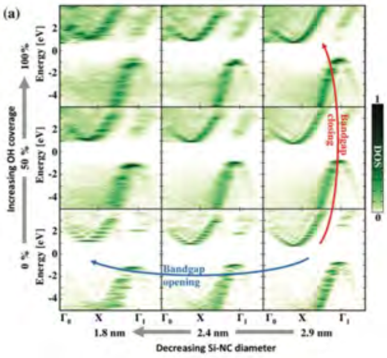

Fig.2 Quasi-band structure obtained from DFT calculations for 0%, 50%, and 100% OH coverage (for brevity 25% and 75% have been omitted), where the energy origin has been set into mid gap. We derived the bandgap as a function of the Si-NC diameter and the OH coverage, which agrees with the experimental results.

References

[1] M. Buerkle and Y. Asai, in preparation

[2] Y. Li, M. Buerkle, G. Li, A. Rostamian, D.R. Bowler, T. Miyazaki, Y. Asai, G Zhou, and N.J. Tao, in preparation

[3] H Nakamura, I. Rungger, S. Sanvito, N. Inoue, J. Tominaga and Y. Asai, *Nanoscale*, **9**, 9386 (2017).

[4] S. R. White and A. E. Feiguin, *Phys. Rev. Lett.* **93**, 076401 (2004).

[5] J. Ozaki and Y. Asai, in preparation

[6] M. Buerkle, M. Lozach, C. McDonald, D. Mariotti, K. Matsubara, Vladimir Svrvcek, *Adv. Funct. Mater.* **27**, 1701898 (2017)

Exploration of hydrogen-1s metallic state and superconductivty in oxyhydride compounds

Ryosuke AKASHI
Department of Physics, University of Tokyo
Hongo, Bunkyo-ku, Tokyo 133-0033

In this project, we pursued metallic states formed by 1s orbitals of hydrogen, especially focusing on the superconductivity. It has actually been long since the possible high-temperature superconductivity has been predicted in compressed elemental hydrogen and hydrogen compounds [1, 2]. Theoretically it is a trivial consequence of the BCS formula [3],

$$T_{\rm c} \simeq \omega {\rm exp}\left[-\frac{1}{\lambda}\right], \tag{1}$$

with ω and λ being the frequency of the phonon mode that mediates the superconducting pairing and its pairing strength, respectively: Namely, if the mass of the ions is small, ω is large and so is $T_{\rm c}$. What is difficult is to realize the compressed situation required for the metallization. The recent discovery of the 200 K superconductivity in H_2S [4] proved that the predicted high T_c phase can indeed occur, but the required pressure was above 100 GPa, which renders difficult further studies on this phase, as well as its practical applications. We therefore focused on how to metallize the hydrogen electronic states more efficiently, from the computational viewpoint.

Recently, some of our colleagues have predicted transition metal oxyhydride ATiO$_2$H (A =Li, Na, K, Rb, Cs), that could be synthesizable in ambient pressure [5, 6]. According to the electronic structure calculation, the valence-top states involve the hydrogen-1s orbitals. To see the possibility of hole-doping in these states, using System B (Sekirei), we calculated the lattice-dynamical properties of the doped ATiO$_2$H. For the uniformly hole-doped case, we found sensitive dependence of the phonon dispersion on the $\mathbf{q}$ point. Namely, as the $\mathbf{q}$ for the dynamical matrix increases significant softening occurs around the X point in the orthogonal Brillouin Zone (Fig. 1), which seems to reflect the nesting property of the valence band. We also examined if this softening character persists in the chemically doped supercell configuration. This result has been presented in American Physical Society Annual Meeting in 2018, and the paper is in preparation [7].

We also studied of H-S systems under pressure to further understand the pressure induced transformation in the compressed H_2S. Through the first-principles structure search by a genetic algorithm, we found various thermodynamically stable sulfur-rich phases. Among them, we calculated with System B the electron-phonon coupling properties of HS_2 and H_5S_8, which are stabilized under pressure around 100 GPa. The result shows that sulfur phonon modes dominate the superconducting coupling, which yield $T_{\rm c}$ around 10 K [8]. Also, in the course of this work, we found a hidden relation between some previously found thermodynamically stable H_3S phases. Extending that relation, we theoretically formed numerous phases. The first-principles structure optimizations performed in System B have confirmed that these phases energetically competes with the previously known sturctures [9]. These results give us an insight into what happens through the pressure induced transition in hydrogen sulfide, which could be useful for systematic exploration of the superconducting hydrogen compounds.

The first-principles electronic structure calculations were done with the plane-wave basis code package QUANTUM ESPRESSO (5.0.3)(Ref.

[10]). The phonon and electron-phonon properties were calculated with the PHonon program in this package, which is based on the density functional perturbation theory [11]. The Brillouin-Zone integration for the metallic systems were done with the optimized tetrahedron method [12]. The GGA-PBE [13] and PBEsol [14] exchange-correlation potentials were used for the H_xS and $A\mathrm{TiO_2H}$ systems, respectively. Parallelization was performed with respect to **k** points (-*npool* option) as implemented in *ph.x* code. The calculations were mainly done in System B. Using the electronic and lattice properties calculated with these programs, for HS_2 and H_5S_8, we calculated T_c by the gap equation in the density functional theory for superconductors [15–17].

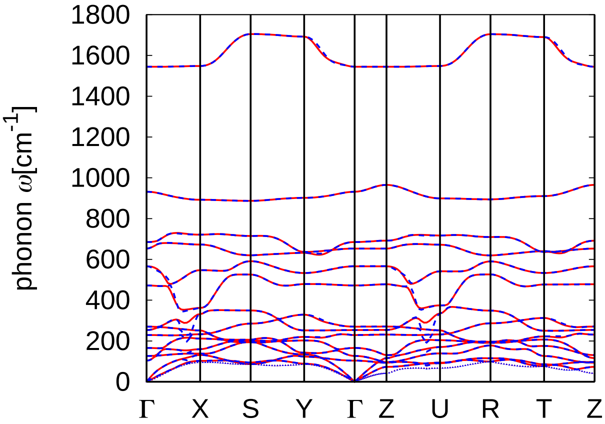

FIG. 1. Phonon dispersions for $\mathrm{RbTiO_2H}$ with 1/4 uniform hole doping, obtained from the dynamical matrices calculated on the (red) 6x6x2 and (blue) 8x8x2 **q** point meshes, respectively. In the latter case, softening around X is observed.

---

[1] N. W. Ashcroft, Phys. Rev. Lett. **21**, 1748 (1968).

[2] N. W. Ashcroft, Phys. Rev. Lett. **92**, 187002 (2004).

[3] J. Bardeen, L. N. Cooper, and J. R. Schrieffer, Phys. Rev. **108**, 1175 (1957).

[4] A. P. Drozdov, M. I. Eremets, and I. A. Troyan, V. Ksenofontov, and S. I. Shylin, Nature (London) **525**, 73 (2015).

[5] N. Sato and S. Tsuneyuki, Appl. Phys. Lett. **109**, 172903 (2016).

[6] N. Sato, R. Akashi, and S. Tsuneyuki, J. Chem. Phys. **147**, 034507 (2017).

[7] M. Ghim, N. Sato, R. Akashi, S.-H. Jhi, and S. Tsuneyuki, in preparation.

[8] I. Kruglov, R. Akashi, S. Yoshikawa, A. R. Oganov, and M. M. D. Esfahani, Phys. Rev. B **96**, 220101(R) (2017).

[9] S. Yoshikawa, R. Akashi, and S. Tsuneyuki, in preparation.

[10] P. Giannozzi *et al*, J. Phys.: Condens. Matter **21**, 395502 (2009); http://www.quantum-espresso.org/.

[11] S. Baroni, S. de Gironcoli, A. Dal Corso, and P. Giannozzi, Rev. Mod. Phys. **73**, 515 (2001).

[12] M. Kawamura, Y. Gohda, and S. Tsuneyuki, Phys. Rev. B **89**, 094515 (2014).

[13] J. P. Perdew, K. Burke, and M. Ernzerhof, Phys. Rev. Lett. **77**, 3865 (1996).

[14] J. P. Perdew, A. Ruzsinszky, G. I. Csonka, O. A. Vydrov, G. E. Scuseria, L. A. Constantin, X. Zhou, and K. Burke, Phys. Rev. Lett. **100**, 136406 (2008).

[15] M. Lüders, M. A. L. Marques, N. N. Lathiotakis, A. Floris, G. Profeta, L. Fast, A. Continenza, S. Massidda, and E. K. U. Gross, Phys. Rev. B **72**, 024545 (2005).

[16] M. A. L. Marques, M. Lüders, N. N. Lathiotakis, G. Profeta, A. Floris, L. Fast, A. Continenza, E. K. U. Gross, and S. Massidda, Phys. Rev. B **72**, 024546 (2005).

[17] R. Akashi, M. Kawamura, S. Tsuneyuki, Y. Nomura, and R. Arita, Phys. Rev. B **91**, 224513 (2015)

Relativistic *ab initio* calculations for valence fluctuation engineering of $4f$-$3d$ intermetallics

Munehisa MATSUMOTO
Institute for Solid State Physics, University of Tokyo
Kashiwa-no-ha, Kashiwa, Chiba 277-8581

April 30, 2018

We look at the intertwined relation between magnetism and superconductivity with a renewed interest in the effects of spin-orbit interaction and valence fluctuations. In $4f$-$3d$ intermetallics of which $3d$-electron part is carried by Fe-group transition metal (TM) elements, strong hybridization can be triggered between magnetically polarized conduction-electron band (c-electron band) and localized f-electrons. Here a hybridized electronic state with an intermediate nature between well localized $4f$-electron state and delocalized $3d$-electron state that mimicks the nature of $5f$-electron state may be found.

Among f-electron based superconductors the highest-temperature superconductivity so far is found for PuCoGa$_5$ with $T_\mathrm{c} = 18.5$ K. This is to be contrasted with $T_\mathrm{c} = 2.3$ K found for CeCoIn$_5$, both of which are most likely magnetically-mediated unconventional superconductors. There is also CeRu$_2$ with $T_\mathrm{c} = 6.3$ K even though this is presumably a conventional BCS superconductor. Tuning the c-f hybridization strength and bandwidth in the proximity to a magnetic quantum critical point, we seek a candidate material made of rare-earth (RE) and TM elements to have an electronic state common to the electronic state of PuCoGa$_5$. This may pave a way to a champion material among Ce-based superconductors.

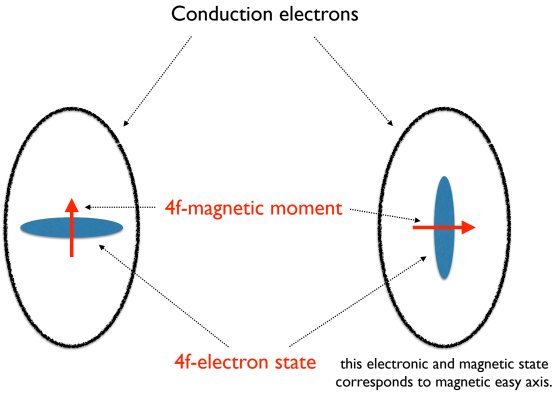

Figure 1: Schematic picture for potential-energy driven magnetic anisotropy realized in RE-TM compounds with localized $4f$-electrons.

Since the spin-orbit interaction that is relatively strong in RE locks the $4f$-electron states with $4f$-magnetic moments, exchange coupling between $4f$-moments and $3d$-electron magnetization leads to bulk magnetic anisotropy when localized $4f$-magnetic moments are put into a particular crystal field. It is pictorically shown in Fig. 1 where the Coulomb interaction between the localized $4f$-electron state and the crystal field environment determines the magnetic easy direction. Interesting flipping of the magnetic easy direction happens when the valence fluctuation comes in as shown in Fig. 2. Kinetic energy gain in $4f$-electrons as an outcome of c-f hybridization brings about orders of magnitude stronger magnetic anisotropy in a direction that is on the opposite side of

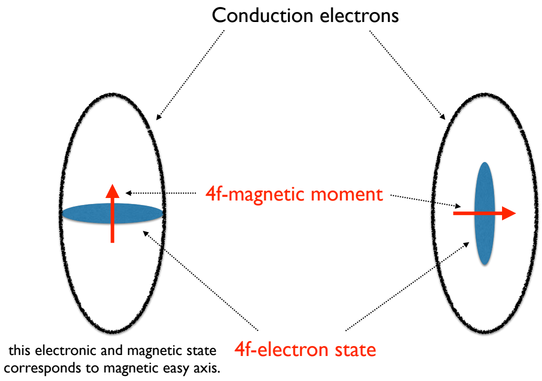

Figure 2: Schematic picture for kinetic-energy driven magnetic anisotropy realized in RE-TM compounds with delocalized $4f$-electrons.

the direction as realized in the conventional magneto-crystalline anisotropy.

Thus magnetic anisotropy and relatively high-temperature superconductivity can potentially be found for the same materials family in a way that is reminiscent of U-based compounds. We investigated effects of valence-fluctuations and spin-orbit interaction for $4f$-$3d$ intermetallics via relativistic *ab initio* calculations and numerical solutions of the associated quantum many-body problems via continuous-time quantum Monte Carlo (CT-QMC) method.

Methods Our *ab initio* calculations were done utilizing OpenMX [1] and LmtART [2]. With OpenMX structure optimization of a complex compound $R_2T_{14}B$ (R=RE element and T=TM element) with 68 atoms in the unit cell has been done utilizing the memory-intensive FAT nodes. Proceeding with OpenMX, fully relativistic calculations with the direction of magnetization being constrained to a specified angle enables us to inspect the magnetic anisotropy. Interfacing with CT-QMC is mostly done with LmtART on the basis of scalar-relativistic calculations. Effects of spin-orbit interaction and crystal fields are described on a model basis. With LmtART k-point parallelization is doable while all of the rest of the calculations scales almost linearly with the number of nodes.

Calculated results are fed back to experimental processes from materials fabrication and macroscopic characterization to microscopic probing of electronic states. Close contacts with experimental groups make an overall joint process to reach a desired material through a few iterations between theoretical calculations and experimental processes.

Effects of kinetic energy gain coming from valence fluctuations in the bulk stability of $4f$-$3d$ intermetallics have been reported elsewhere [3].

So far we have been working on a set of microscopic calculations combining *ab initio* calculations and many-body calculations in a thermal equilibrium state. Bridging the gap between such microscopic data and mesocopic observation slightly off equilibrium [4] makes the next steps toward providing calculated data that can be directly compared to experimental observations, such as the finite-temperature coercivity of RE permanent magnets made of $4f$-$3d$ intermetallics.

Acknowledgments Helpful discussions with Hiroaki Shishido and Tetsuro Ueno are gratefully acknowledged.

References

[1] http://www.openmx-square.org

[2] S. Y. Savrasov, Phys. Rev. B **54**, 16470 (1996).

[3] MM in the 73rd annual JPS meeting (2018).

[4] R. Kubo: J. Phys. Soc. Jpn. **12** (1957) 570.

STM simulations for modifeid β-FeSi$_2$(100) and Fe-adsorbed Si(111) surfaces

Kei Tanimoto and Ken HATTORI
Graduate School of Science and Technology, Nara Institute of Science and Technology
Takayama, Ikoma, Nara 630-0192

Using scanning tunneling microscopy (STM), author's group has been studied the growth of β-FeSi$_2$(100) nano-films on Si(001) [1] and iron-silicides formation on Si(111) [2] prepared in ultra-high vacuum. On β-FeSi$_2$(100) surface, STM showed a dip line on a bending region of the nano-film at a Si substrate step-edge [3]. Transmission electron microscopy results in cross section denied the geometrical dip. Thus in this research, first, we examined the possibility of electronic effects induced by in-plain strains, for the dip property. STM images were created with Simulation Tool for Atom TEchnology (STATE)-Senri under the dipole corrections in the vacuum region [4]. The β-FeSi$_2$(100) surface structure with Si tetramer on top has been established [1]. Here, the model is based on a free-standing single quintuple layers (QL) (Si/Fe/Fe/Si/Fe) with a Si bottom layer.

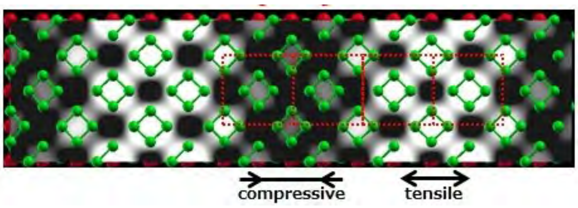

Figure 1: A simulated STM image of β-FeSi$_2$(100) with 10 % of in-plain compressive and tensile strains at sample bias voltage (V_S) of -1.0 V.

Figure 1 displays a topographic image at a filled state with in-plain compressive and tensile strains of $\Delta x/L = 0.1$ in maximum (L is the unit length in the x direction.) Here 4×1 unit cells, consisting of 32 Fe and 96 Si atoms, were used. In the calculation, the bottom-layer Si atoms were fixed to the ideal positions shifted with $[(\Delta x/L)\sin(2\pi x/4L), 0, 0]$, while the other atoms were relaxed $\leq$0.05 eV/Å. Obviously the compressive region indicates a dark (dip) feature while the tensile bright. The images at empty states showed the similar features. These STM simulations suggest that the dip lines at the downer side of the bending region in the experimental images are caused by compressive strain.

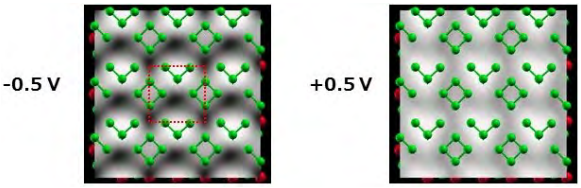

Figure 2: A simulated STM image of β-FeSi$_2$(100) with a mono vacancy in a Si tetramer at V_S = -0.5 and +0.5 V.

The β-FeSi$_2$(100) surfaces showed two types of defects experimentally in STM [3, 5]. One is a depression at a tetramer site [namely, dark (D) site] and another is a pair of high protrusion [bright (B)-site pair] at filled and empty states. In order to survey the defect structures, STM images of vacancy models and molecular-adsorption models were simulated in 1×1 or 2×2 unit-cell frames with the fixed bottom-layer. The simulations indicated that mono, di, tri, and tetra Si-vacancies in the Si tetramer present BB (bright in filled and bright in empty states, Fig. 2), DB, DB, and DD features, respectively.

For the hydrogen adsorption, the stable configuration was a bridge type among atop (8 different cases were simulated), bridge (8), and hollow (2) ones; a bridge H configuration did not induce any distinct change in both STM images (Fig. 3). For the hydroxyl adsorption, the stable configuration was also a bridge type among atop (1 case was simulated), bridge (1), and hollow (1) ones; a bridge OH configuration showed BB feature. For the oxygen adsorption, a bridge O configuration showed DD feature. One of the interpretations for experimentally-observed single DD site is tetra Si-vacancies which would explain an increase of the dark defects by high-temperature annealing, but the BB-site pair is under the discussion though a pair of OH bridge-sites is a candidate.

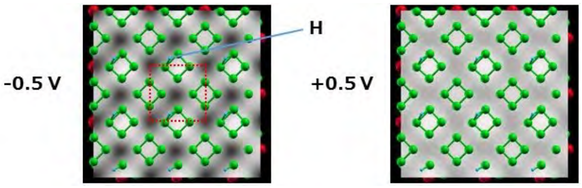

Figure 3: A simulated STM image of β-$FeSi_2$(100) with a hydrogen atom at a brige site of a Si tetramer at V_S = -0.5 and +0.5 V.

For the system of Si(111)7×7 with isolated Fe atoms, we observed 5 different adsorption types in experimental STM images [6]. Here, some configurations for a Fe atom on Si(111)7×7 and 4×4 surfaces based on the dimer–adatom–stacking-fault model [7] were simulated. First, clean Si(111) surfaces consisting of a Si adatom-layer, six Si-layers, and a bottom H-terminated layer were imaged for 7×7 (347 atoms) and 4×4 (118 atoms, a simple model of 7×7 keeping key structures [8]) models under relaxing top six layers.

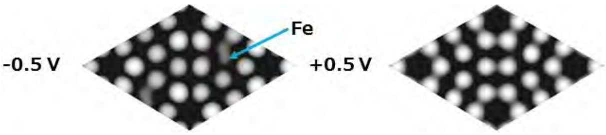

Figure 4: A simulated STM image of Si(111)7×7 with an iron atom at a H_3 site close to a center adatom on an unfaulted half unitcell at V_S = -0.5 and +0.5 V.

On the 4×4 surface, an Fe atom was located above 17 different Si atoms in the adatom, 1st, 2nd (3rd) and 4th (5th) layers, and fully relaxed without spin polarization. The stable configuration was a H_3 type (above 4th-layer Si close to an adatom), showing a dark adatom at V_S = -0.5 V which resembles one of the experimental images. On the 7×7 surface, 13 configurations were converged among 18 configurations, and the stable configuration was a H_3 type showing a dark adatom at -0.5 V (Fig. 4). In order to discuss the other adsorption types, we require the calculations for much more configurations with the spin polarization.

The authors thank Profs. Morikawa, Hamada, and Inagaki in Osaka University, and Prof. Yanagisawa in Ryukyu University for their great support in STATE-Senri calculations.

References

[1] O. Romanyuk, K. Hattori, M. Someta, and H. Daimon, Phys. Rev. B **90** (2014) 155305.

[2] K. Kataoka, K. Hattori, Y. Miyatake, and H. Daimon, Phys. Rev. B **74** (2006) 155406.

[3] M. Someta, M. Thesis, Nara Institute of Science and Technology, Nara (2008) [in Japanese].

[4] Y. Morikawa, Phys. Rev. B **63** (2001) 033405, and references therein.

[5] H. Yang, Dr.. Thesis, Nara Institute of Science and Technology, Nara (2018).

[6] K. Kataoka, Dr.. Thesis, Nara Institute of Science and Technology, Nara (2006).

[7] Guo-Xin Qian and D. J.Chadi, Phys. Rev. B **35** (1987) 1288.

[8] This corresponds to the extension of the 4×2 structure [A. Vittadini and A. Selloni, Phys. Rev. Lett. **75** (1995) 4756.]

Development of crystal structure prediction method and search for magnet and spintronics materials

Tomoki YAMASHITA
Research and Services Division of Materials Data and Integrated System (MaDIS),
National Institute for Materials Science (NIMS)
1-2-1 Sengen, Tsukuba, Ibaraki 305-0047

We developed a crystal structure prediction method based on Bayesian optimization [1]. Crystal structure prediction with Bayesian optimization can efficiently select the most stable structure from a large number of candidate structures with a lower number of searching trials using a machine learning technique. Crystal structure prediction simulations were carried out for Y_2Co_{17}, which is important compositions of Sm-Co magnets, to discuss the efficiency of Bayesian optimization. In these simulations, total energy calculations and structure optimization were done using the density functional theory with the projector-augmented wave method [2], as implemented in the VASP code [3]. These structure optimization calculations were performed using the supercomputer system at the ISSP. The results demonstrate that Bayesian optimization can significantly reduce the number of searching trials required to find the global minimum structure by 30–40% in comparison with pure random search, which leads to much less computational cost.

We collected the data of magnetocrystalline anisotropy (MA) in Co-based 3d transitions-metal thin films to perform machine learning analyses in future. First-principles calculations were done using the supercomputer system at the ISSP. Full-potential linearized augmented plane wave (FLAPW) method [4, 5] with generalized gradient approximation (GGA) was employed. Spin-orbit coupling was treated within the second-variation method and the magnetic anisotropy energy (MAE) was estimated by the force theorem. The MAE of possible atomic-layer alignments of Co-based 3d transition-metal films with $ABAB$ and $ABCABC$ stacking including Mn, Fe, and Ni layers are presented. The results predict that large perpendicular MA (PMA) can be achieved by tuning the atomic-layer alignments in Co-Ni films. We provide useful guidelines for the choice of atomic-layer alignments in Co-Ni thin films for realizing large MAE.

References

[1] T. Yamashita, N. Sato, H. Kino, T. Miyake, K. Tsuda, and T. Oguchi, Phys. Rev. Materials **2**, 013803 (2018).

[2] Blöchl, Phys. Rev. B **50**, 17953 (1994).

[3] G. Kresse and J. Furthmüller, Phys. Rev. B **54**, 11169 (1996).

[4] M. Weinert, J. Math. Phys. **22**, 2433 (1981).

[5] W. Wimmer, H. Krakauer, M. Weinert, and A. J. Freeman, Phys. Rev. B **24**, 864 (1981).

Elucidation of Catalytic Activity of Solid Acid and Base by Protonic Activity Estimation via Hydrated Multilayer

Ryuhei Sato and Shu Yamaguchi
Department of Materials Engineering,
The University of Tokyo, Bunkyo-ku, Hongo, Tokyo 113-0032

Proton activity on oxide surface is paid considerable attention to the application as electrolytes and metal/oxide catalysts. For example, a significant contribution of proton conduction on a CeO_2 surface was reported as a critical factor to an enhanced catalytic efficiency of electrochemical steam reforming of CH_4 on Pd/CeO_2 [1]. According to previous AIMD simulations, this proton migration on hydrated oxide surface is a kind of neutralization reaction of H_2O adsorbates. Therefore, to study the emergence of Brønsted acidity by the adsorption of acid-base molecules like H_2SO_4, HCOOH, CH_3OH, etc. is crucial for the catalytic reaction. Here, we studied the relationship between molecule adsorption and subsequent emergence of Brønsted acidity.

Adsorption reaction of H_2O, HCOOH, and CH_3OH on bare cubic ZrO_2(110) surface is analyzed by ab initio molecular dynamic (AIMD) simulation to study the adsorption mechanism. After adsorption reaction, we also examine the hydration reaction of HCOOH and CH_3OH-terminated surface to understand the interaction between these organic and H_2O molecules on the surface. All the simulations were performed by home-made code written by F. Shimojo et al. [2]. The author employed the GGA/PBE functional and PAW method with L4cpu and L36cpu queues.

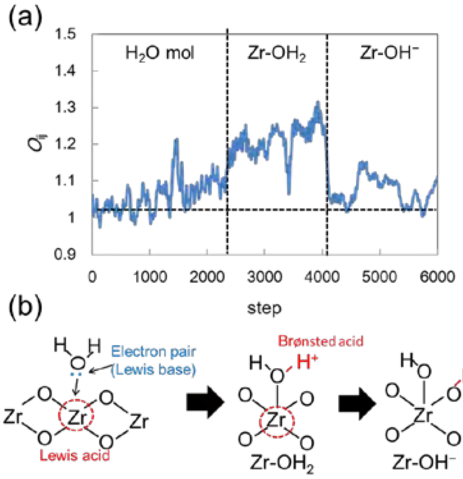

Figure 1. (a) time series of sum of bond overlap population around O atom in an adsorbed H_2O molecule during AIMD simulation of H_2O adsorption on cubic ZrO_2 (110) surface, and (b) schematic image of neutralization of surface strong Lewis acid (Zr ion sites) by molecule adsorption and subsequent deprotonation reaction by an adsorbed molecule.

According to the observation from these AIMD simulations, molecule adsorption is a neutralization reaction of surface ion sites as a strong Lewis acid (metal ion sites) or base (oxide ion sites). After this neutralization reaction, these adsorbed molecules subsequently release protons because of the strong Lewis acid/base interaction between surface sites and molecules. Owing to significant stabilization by the additional covalent bond formation, Brønsted acidity emerges by the increased instability of hydrogen. For example, H_2O molecules first chemisorb on Zr ion sites and then dissociate H^+ to form Zr-OH^- by the help of basic surface oxide ion site (>O) as shown schematically in Fig.1(b). Therefore, the strength of covalent bonding formed between Zr ion sites and molecules, in other words, the strength of the neutralization reaction of Lewis-acidic Zr ion sites by non-dissociative adsorbates, gives primary influence to Brønsted acidity of adsorbates.

Figure 1(a) shows time series of the sum of bond overlap population around O atom in adsorbed H_2O molecules during AIMD simulation of H_2O adsorption on cubic ZrO_2(110) surface in reference to O in H_2O molecule. As shown in Fig. 1(a), the number of bonds around O atom become excessive compared to H_2O molecule, when H_2O molecule adsorbs on a surface Zr ion site to form Zr-OH_2. This excessive bond is relaxed after proton dissociation, which implies that this excessive bond formed by non-dissociative adsorption contributes to the deprotonation reaction. This postulate is further confirmed by comparing bond overlap population between O and H atom in adsorbates and the one between surface Zr ion site and O atom in adsorbates in Fig. 2, showing that the strength of O-H bond decreases with the increase of Zr-O bond strength. Also, the rate of decrease in O-H bond is independent on adsorbate species, as far as these molecules are composed of same elements (here they are composed of C, H, and O atoms.), which implies there is a common mechanism for molecule adsorption and subsequent emergence of Brønsted acidity. Analysis of the bond property of adsorbates based on the energetics is now underway to directly compare the deprotonation behavior of adsorbed molecules, which include different elements and have different electronegativity.

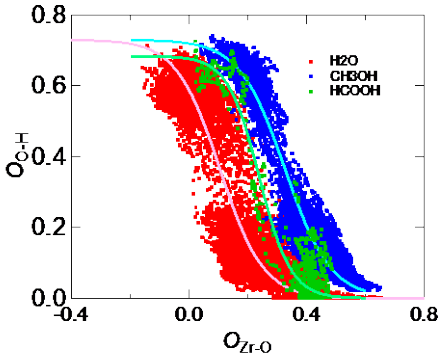

Figure 2. Bond overlap population between O and H atom in adsorbed molecules ($O_{O\text{-}H}$) vs that between O in adsorbed molecules and surface Zr ion sites ($O_{Zr\text{-}O}$) during AIMD simulation of molecule adsorption on ZrO_2 surface. Each dot represents the bonding property of an adsorbate in particular time step. Curves show the fitting result of these data by sigmoid function.

References

[1] R. Manabe, S. Okada, R. Inagaki, K. Oshima, S. Ogo, Y. Sekine, *Sci. Rep.* 6, (2016) 38007.

[2] F. Shimojo, R.K. Kalia, A. Nakano, P. Vashishta, *Comp. Phys. Comm.* **140** (2001) 303.

Functionality of solid-liquid interface

Osamu Sugino
Institute for Solid State Physics,
The University of Tokyo, Kashiwa-no-ha, Kashiwa, Chiba 277-8581

We have studied the H adsorption at the Pt(111)/solution interface using the density functional theory (DFT) within the level of random phase approximation (RPA). This system was studied intensively in the past using the DFT-PBE in the past [1] but reliable view on the adsorption isotherm has not been established. Considering its significance on the understanding of fuel-cell reactions, we have revisited this problem using the time-consuming DFT-RPA; most of the computational time was spent in this problem in this fiscal year.

After very stringently testing the convergence of the DFT-RPA total-energy with respect to the number of plane wave basis, k-points and Pt layers, we have estimated the value for the adsorption energy on the fcc and atop sites. Compared with DFT-PBE, RPA provide strong competition between the adsorption sites, supporting a coexisting feature at the coverage close to the full-monolayer. This result, together with additional calculation on the coverage-dependent adsorption energy, explains why H adsorbed on the atop site, H_{atop}, appears close to the full-monolayer condition and suggests that importance of the Heyrovsky reaction, by which the discharging reaction of a hydronium ion occurs on H_{atop}, was underestimated by PBE.

Major difference between PBE and RPA is found originated from the different value for the equilibrium lattice parameter. The difference can thus be made very smaller by letting the PBE calculation using the experimental (or RPA-optimized) lattice parameter. This provides a practical way to empirically adjusting the PBE calculation.

The difference in the adsorption energy between atop and fcc was found quite small, about twice the value of the thermal energy at room temperature. It is important to note that this small energy difference can be reliably predicted only when using the RPA level.

The different adsorption energy for the different sites is found mainly due to the difference in the zero-point energy, indicating an importance of the isotope mass in determining the most stable adsorption site. The RPA calculation showed that the order of the stability between H and D is the same but relative abundance of the atop adsorbate is significantly different between them. This suggests a possibility of separating D from H using the fuel cell system consistent with the existing experiment.

References

[1] T.T.T.Hanh, Y. Takimoto and O. Sugino, Surf. Sci. 625, 104-111 (2014).

First-Principles Molecular-Dynamics Study of Structural and Electronic Properties of Covalent Glasses under Pressure

Fuyuki SHIMOJO, Akihide KOURA, Masaaki MISAWA, and Shintaro HAYASHI
Department of Physics, Kumamoto University, Kumamoto 860-8555

So far, permanent densification of SiO_2 glass has been widely studied both experimentally and theoretically since its discovery in the 1950s [1]. It has been known that silicate glasses, such as $MgSiO_3$, also show permanent densification when the glasses are decompressed from high pressures. In this study, we investigate the microscopic structure of densified $MgSiO_3$ glass compared with SiO_2.

To clarify the microscopic mechanism of the densification, we have carried out first-principles molecular-dynamics simulations on the decompression process of $MgSiO_3$ glass in its relaxed state from high pressures up to 20 GPa. First, the temperature was increased to 3000 K at high pressures to obtain the liquid state. Second, the densified glass was obtained by decreasing the temperature to 300 K while keeping high pressures. Third, the pressure was decreased to 0 GPa, and permanently densified glass was obtained at ambient conditions.

We confirmed that the density of densified glass at ambient conditions is in good agreement with experiments [2]. Also, the static structure factors obtained by neutron and X-ray experiments were well reproduced by our simulations. In comparison of ordinary glass, some difference of structure factors in the long-wave length region was seen, while the overall profiles are very similar to each other. This result shows that the structure in the intermediate range, such as ring structure, is changed in permanently densified glass, while the local structure is almost the same as the coordination number is unchanged.

In the case of SiO_2 glass, the ring size distribution shows that the network of densified glass is formed from smaller size rings than ordinary glass, which suggests that permanent densification is caused by the reconstruction of the network structure. On the other hand, the network structure in $MgSiO_3$ glass is not clearly defined because many non-bridging, *i.e.* one-fold coordinated, oxygen atoms exist, and the connectivity between Si and O atoms is broken. The investigation of the densification mechanism in $MgSiO_3$ glass is underway.

References

[1] P. W. Bridgman and I. Šimon: J. Appl. Phys. **24**, 405 (1953).

[2] M. C. Wilding *et al.*: Europhys. Lett. **67**, 212 (2004).

First-Principles Calculation on Reversible Hydrogenation Reaction of Toluene using Heterogenous Catalyst

Hiromi NAKAI

Faculty of Science and Engineering,

Waseda University, Okubo, Shinjuku, Tokyo 169-8555

Reversible dehydrogenation reaction of methylcyclohexane into toluene, by using Pt catalyst is a prospective hydrogen storage and transportation technology. One of the issues is the demethylation reaction producing toxic benzene (BZ). Addition of small amount of Sn to the Pt catalyst suppresses the side reaction, whereas the mechanism is unknown.

The present study investigated the mechanisms of Sn addition effects by using density functional theory (DFT) calculations. The kinetics of the present system was detailed via micro-kinetic analyses; the reaction rate equations that are simultaneous ordinary differentiation equations for all elementary steps are solved numerically. All kinetic parameters, i.e., reaction rate constants (activation energies) were calculated by DFT. We have considered 12 elementary reactions occurring on Pt(111), Pt(311), $Pt_3Sn(111)$, and $Pt_3Sn(311)$, taking the reaction site dependences into account. Calculations were performed by using the VASP code, which is available on the System B with a number of computational nodes, installed at the Institute for Solid State Physics, the University of Tokyo.

Figure 1 shows the time-course changes of the ratio of side-reactions: ratio of partial pressure of BZ to hydrogen molecule. In the case of Pt surface, the selectivity rapidly increased and reached to the steady-state. In the case of Pt_3Sn, BZ/H_2 ratio gradually increased. Consequently, in the short time region of $t <$ ca. 400 s, BZ/H_2 ratio was smaller than Pt case. This means that the demethylation reaction is kinetically suppressed with Sn addition. Detailed analyses on surface coverages revealed that suppress of side reaction would be attributed to the smaller coverages of reactant species on Pt_3Sn surface than that on Pt surface, which were due to the smaller absorption energies of hydrocarbons onto the Pt_3Sn surface.

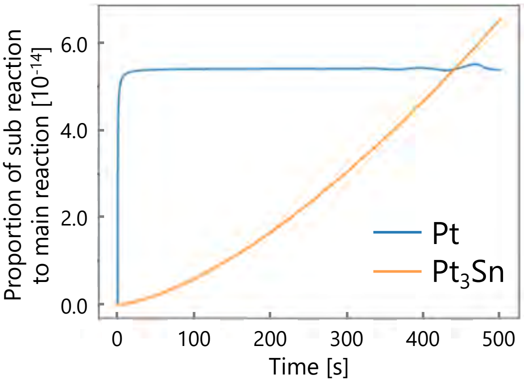

Figure 1. Time-course changes of the ratio of side reaction to main reactions.

Electronic States and Thermodynamic Stability of Two-Dimensional Crystals of Group IV Elements

Masaaki Araidai

Institute of Materials and Systems for Sustainability, Nagoya University
Furo-cho, Chikusa-ku, Nagoya, 464-8603

Two dimensional crystals consisting of group IV element heavier than carbon, such as silicene, germanene, and stanene, are supreme thin-film materials. They have been theoretically predicted to possess high carrier mobility and some intriguing functions such as band-gap control and topological insulator [1,2]. They have been recently synthesized on metallic substrate [3,4,5,6]. However, it has been reported that the electronic state of silicene on a metallic substrate are dramatically modified by the strong interactions with the surface atoms [7,8]. This indicates that one cannot utilize the intriguing electronic states inherent in two-dimensional crystals successfully and perfectly when they are placed on a metallic substrate. Therefore, toward the device fabrication utilizing the electronic states inherent in the two-dimensional crystals, it is prerequisite for understanding their properties on insulating substrates.

In this work, we investigated the optimized structures and the electronic states of germanene and stanene with larger spin-orbit interactions than silicene on α-Al_2O_3 (0001), using the first-principles calculations based on the density-functional theory. The calculations were performed using the VASP code [9]. We employed the projected-augmented-wave potential and the exchange-correlation functional of PBE-type generalized gradient approximation. All atomic configurations were relaxed until the Hellmann-Feynman force becomes smaller than 5 meV/Å.

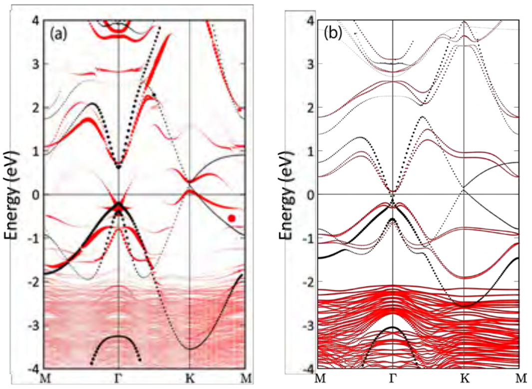

Fig.1 Electronic band structures of (a) 2x2 germanene on α-Al_2O_3 (0001) √3x√3 surface and (b) 1x1 stanene on α-Al_2O_3 (0001) 1x1 surface. The vasp_unfold code [10] was used to draw the unfolded band structure of germanene.

Figure 1 shows the electronic band structures of (a) germanene and (b) stanene on α-Al_2O_3 (0001) surfaces. The black dotted lines in each panel denote the band structure of the corresponding freestanding one. The bundles of the electronic band below ~1.7 eV in (a) and ~2.0 eV in (b) represent the valence bands of the surfaces. We can observe from Fig. 1 that the band structures are affected owing to the surface adsorptions, especially around K point, at which low-energy quasi-particles of free-standing germanene and stanene are massive Dirac fermions. The degree of the modulation depends on the strength of the interactions. We found from population analyses for chemical bonds that the electronic states are perturbed not by bondings with surface aluminum atoms but surface oxygen atoms.

References

[1] K. Takeda and K. Shiraishi, Phys. Rev. B **50**, 14916 (1994). [2] M. Ezawa, New J. Phys. **14**, 033003 (2013). [3] A. Fleurence, et al., Phys. Rev. Lett. **108**, 245501 (2012). [4] P. Vogt, et al., Phys. Rev. Lett. **108**, 155501 (2012). [5] L. Li, et al., Adv. Mat. **26**, 4820 (2014). [6] J. Yuhara, et al., 2D Mater. **5**, 025002 (2018). [7] Z.-X. Guo, et al., J. Phys. Soc. Jpn. **82**, 063714 (2013). [8] M. X. Chen and M. Weinert, Nano Lett. **14**, 5189 (2014). [9] G. Kresse and D. Joubert, Phys. Rev. B **59**, 1758 (1999). [10] M. Tomić, H. O. Jeschke and R. Valentí, Phys. Rev. B **90**, 195121 (2014).

Exploration of structure motifs characterizing the metal oxides

Kazuto AKAGI

AIMR, Tohoku University, Katahira, Aoba-ku, Sendai, Miyagi 980-8577

Electron trap site in a-HfO_2

Amorphous HfO_2 (a-HfO_2) is a prototype high dielectric constant insulator with wide technological applications. Using classical MD and DFT (PBE, HSE) calculations, we found that excess electrons and holes can be trapped as deep polaron states. They were localized at precursor sites and the polaronic relaxation was amplified by the local disorder of amorphous network [1]. Based on these findings, we tried extraction of structural motifs of the electron trapping site to identify the precursor structures in classical-MD calculations. First, we prepared 35 samples of electron trapping sites by DFT calculations and calculated persistent-homology. The topological information was translated to vectors via persistence diagrams where birth and death of "rings" with increasing radius of virtual spheres at atomic positions are recorded. Using a few common structural motifs obtained by principal component analysis (PCA) of these vectors, potential precursor structures in the classical-MD calculations were searched by evaluating “distance” between these principal component vectors and the vectors representing snapshots from the trajectories. The result was encouraging, but some precursors were failed to detect when structure relaxation by DFT calculation is significantly large.

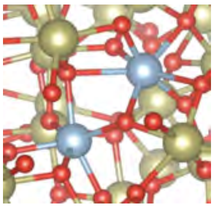

Fig.1 An example of the electron trapping sites well represented by PCA of persistence diagrams.

Shallow trap state in Rh:$SrTiO_3$

Rh^{3+}-doped $SrTiO_3$ is a highly active photocatalyst with visible light response for water splitting. The oxygen vacancy (Vo) formation required for charge compensation in this material leads to a complex defect-related electronic state, especially a shallow unoccupied trap state reducing the lifetime of photocarrier. Based on the systematic DFT (GGA and hybrid-functional) calculations of 4×4×4 $SrTiO_3$ cells containing one or two Rh^{3+} and Vo, we found shallow unoccupied trap state are closely related to Rh^{3+}-Vo complexes. We also found that the charge state of Rh is controlled by both the configuration and the ratio of Rh and Vo. While the valence state of an octahedrally-coordinated Rh can be reduced no further than the 3+ state, Rh in complex cluster configurations with other Rh atoms or Vo can be further reduced to lower valence states.

References

[1] M. Kaviani *et al.*, PRB, **95**, 075117 (2017).

First-principles calculation for surface electron dynamics

Kazuhiro YABANA
Center for Computational Sciences,
University of Tsukuba, Tsukuba 305-8577

We develop a first-principles computational method to investigate electron dynamics induced by ultrashort laser pulses based on time-dependent density functional theory (TDDFT) in real time. We develop the code SALMON (Scalable Ab-initio Light-Matter simulator for Optics and Nanoscience) and make it open to the public at our website, http://salmon-tddft.jp. At present, SALMON is capable of describing electron dynamics in either isolated or periodic boundary conditions. In the present project, we aim to extend the code so that we can describe the electron dynamics in a thin film, periodic in two-dimensions and isolated boundary condition for one-dimension. We expect we can investigate the electron dynamics at a surface calculating sufficiently thick films.

To describe the interaction of pulsed light with thin films, we solve the coupled equations: the Maxwell's equations for the electro-magnetic fields of the pulsed light and the time-dependent Kohn-Sham equation for electrons in the thim film. We can then directly investigate the reflection, transmission, and absorption of the pulsed light. A finite difference scheme with the uniform grids in the three-dimensional Cartesian coordinate is used to solve the equations. A common spatial grid is used for both electron and light-wave dynamics. Since the speed of light is much faster than that of electrons, we use different time steps for two dynamics.

As a test case, we applied the method for a thin silicon film with the surface atoms terminated with hydrogen atoms. We calculate the reflection, transmission, and absorption for several thin films of different thickness, changing the frequency and the intensity of the pulsed light, and compare them with results of ordinary macroscopic electromagnetism in which we utilize the dielectric function obtained from the TDDFT calculation. In our preliminary analysis, it is found that the results by the coupled Maxwell-TDDFT calculations and by the macroscopic electromagnetism agree well even for a rather thin film of a few nano-meters. For the film of thickness less than 1nm, the optical properties changes drastically at certain frequency region. We also find a large change in the reflection for an intense laser pulse due to the nonlinear effects.

Magnetic anisotropy analysis of transition-metal-doped Nd-Fe-B magnets by first-principles calculations

Yasutomi TATETSU

Tokyo Institute of Technology, Nagatsuta, Yokohama, Kanagawa 226-8502

Nd-Fe-B sintered magnets, known as the strongest magnets, are used in various kinds of applications, for example, vehicles, turbines, etc., since they have the largest $(BH)_{\max}$ among permanent magnets. However, the mechanism of the thermal instability in the coercivity of Nd-Fe-B magnets is not clear because there are numerous unknown factors that reduce the coercivity. Controlling the grain boundary phase of these magnets by annealing processes or doping some elements is the most effective way to enhance the coercivity of Nd-Fe-B magnets.

Previously, we performed first-principles calculations for the Cu-doped $Nd_2Fe_{14}B/Nd_4O$ systems using a computational code OpenMX [1] in order to understand the role of Cu in this system [2]. By calculating the formation energies of some model structures, we found that the models with Cu existing at the interstitial space and Fe site at the interface are energetically stable compared to the non-Cu-doped model structure. Especially, in the model with Cu at the Fe site at the interface, the magnetic anisotropy of Nd near Cu at the interface is improved due to Cu, which is in good agreement with experimental results [3].

There is a possibility that other elements, which have not been added into Nd-Fe-B magnets, may enhance the ability of Nd-Fe-B magnets. We study the magnetic properties of the substitution effects in $Nd_2(Fe, X)_{14}B$ (X = Mg, Al, Si, Ca, Sc, Ti, V, Cr, Mn, Fe, Co, Ni, Cu, Zn, Ga, Ge) by first-principles calculations in order to understand which added elements have the ability to improve the coercivity of Nd-Fe-B magnets [4]. We replace one Fe atom at different Wyckoff positions with one X atom in each calculation in order to determine the stability of the systems (see figure). System B was mainly used to optimize the Fe-substituted systems. By calculating the formation energy of

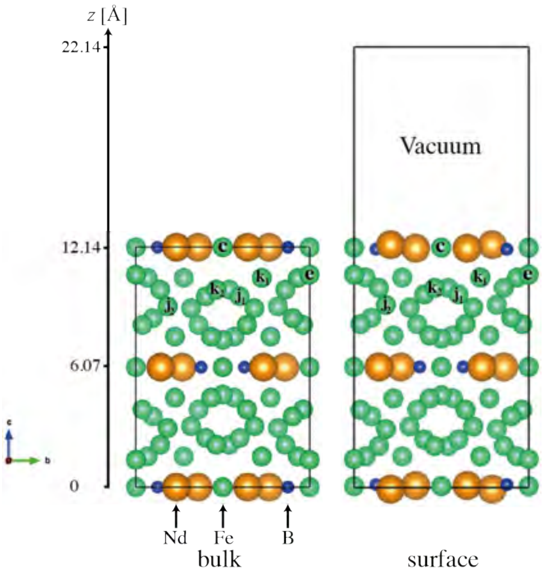

Figure: Fe-substituted model system of $Nd_2(Fe, X)_{14}B$.

the Fe-substituted system with X, only replacing Fe at the c site with Mg, Ca, Sc, Cu, Zn, or Ga in the bulk or surface system shows the improvement of the magnetic anisotropy of Nd near X because of the *p*-*d* interaction between Nd and these added elements. The charge transfer between Nd 5*d* and X *p* occurs in order to reduce the exchange interaction. This charge transfer increase/decreases the number of Nd 5*d* electrons in uniaxial/in-plain orbitals, which triggers the magnetic anisotropy improvement of Nd. Our calculation result suggests that one can consider the possibility of improving the coercivity of Nd-Fe-B magnets by adding these elements.

References

[1] http://www.openmx-square.org

[2] Y. Tatetsu, S. Tsuneyuki, and Y. Gohda, Phys. Rev. Appl. **6**, 064029 (2016).

[3] H. Sepehri-Amin *et al.*, Acta Mater. **60**, 819 (2012).

[4] Y. Tatetsu, S. Tsuneyuki, and Y. Gohda, submitted.

Hybrid *ab initio* QM/MM calculations of functional mechanisms of biological macromolecular systems recognizing supercoiled DNA

Masaru Tateno

Graduate school of Life Science, University of Hyogo, 3-2-1 Kouto, Kamigori-cho, Hyogo 678-1297

We have studied the functional mechanisms of biological macromolecular systems that interact with supercoiled DNA. The targets are the following two systems; i.e., supercoiled DNA recognition (SDR) peptide and DNA topoisomerase IIβ (topoIIβ). Moreover, the electronic structures of iron-sulfur [4Fe-3S] clusters in hydrogenases were also investigated this FY.

SDR peptide

The SDR peptide is a designed small protein that is composed of 27 amino acid residues, $(Lys)_9(Glu)_9(Lys)_9$. The SDR peptide was found to bind to the supercoiled DNA selectively and cooperatively. These significant properties are originated from its characteristic amino acid sequence. In this study, we analyzed the mechanisms of the selective and cooperative binding of the SDR peptide to supercoiled double strand DNA molecules, based on our previous studies [1].

We first focused on the physico-chemical properties of the SDR peptide in the free state. The conformational ensemble of the SDR peptide in solution was generated by an advanced molecular dynamics (MD) method (*i.e.*, temperature replica exchange; REMD). In this calculation, we performed 128-replica MD simulations in parallel, and generated a 24.32 μs (190 ns × 128 replicas) trajectory as the total. The numerous replicas (128 replicas) were derived from the fully-solvated system, which included 166,981 atoms. On average, a 20-ns MD simulation consumed 5 hours with 22 nodes (512 cores) or 10 hours with 2 nodes (total 48 cores) accelerated by 4 × 2880 CUDA cores, of SGI ICE XA (×4 Intel Xeon E5-2680v3 CPU and ×4 NVIDIA Tesla K40).

The REMD revealed that substantial amounts of ordered, helical structures were unexpectedly present in our obtained conformational ensemble, which was found to be consistent with our biophysical experimental analysis employing circular dichroism (CD) spectroscopy. Furthermore, we performed the statistical analysis of the structural ensemble, and identified the hydrophobic nucleus, which was stabilized by closely cohesive residue contacts formed through “hybrid” hydrophobic and electrostatic residue contacts. This is the first report to address the mechanisms of formation of the core packing in the semi-stable conformations of a peptide.

TopoIIβ

DNA topoisomerase IIβ (topoIIβ) is an enzyme to recognize and cleave the supercoiled double stranded (ds) DNA molecules, and thereby is involved in the regulation of the transcription and replication. By employing MD simulations, we built a structural model of the initial state (prior to the enzymatic reaction) of the enzyme-substrate (ES) complex of topoIIβ and dsDNA, toward hybrid *ab initio* QM/MM calculations to analyze the catalytic mechanisms of the dsDNA cleavage reaction.

This FY, we focused on the analysis of the frontier orbitals in the catalytic site. As a consequence, we found that the highest occupied molecular orbital (HOMO) was located on a tyrosine (Tyr) residue, which thus led us to a novel scheme of the catalytic reaction by topoIIβ. This identified mechanism may be closely relevant to the degenerated sequence motifs that are recognized by topoIIβ, and so we also performed a genome wide analysis to identify the motifs by our novel bioinformatics approach [2]. These combined methods would elucidate the reasons and mechanisms of the correlation between the catalysis, and the degeneracy of the recognition sequence motifs.

Hydrogenase

Hydrogenases are a metalloenzyme family, and catalyze both dissociation and production of dihydrogen (H_2); i.e., $H_2 \rightleftharpoons 2H^+ + 2e^-$. The crystallographic and spectroscopic experiments showed that a membrane bound hydrogenase (MBH) included a hydroxyl ion (OH^-) that was bound to an Fe of the super-oxidized $[4Fe\text{-}3S]^{5+}$ cluster that is located in the proximity of the [Ni-Fe] active site. However, the functional role of the hydroxyl ion was still left to be unknown. In this study, we investigated the electronic structure of the super-oxidized $[4Fe\text{-}3S]^{5+}$ proximal cluster in the presence/absence of the OH^-, employing *ab initio* density functional theory (DFT) calculation.

The analysis revealed that the OH^- ion significantly altered the electronic structure, thereby inducing localization of the HOMO and delocalization of the lowest unoccupied molecular orbital (LUMO) toward the [Ni-Fe] active site. The analysis also showed that the LUMO was consistent with the ET pathways found by the independent semi-empirical theoretical analysis. Thus, this is the first report to address the mechanisms for creating an ET pathway in a biological system, based on the electronic structure [3].

References

[1] J. Kang and M. Tateno: J. Phys. Soc. Jpn. **86** (2017) 074802.

[2] A. Sugimoto, T. Sumi, J. Kang and M. Tateno: J. Phys. Soc. Jpn. **86** (2017) 074803.

[3] J. Kim, J. Kang, H. Nishigami, H. Kino and M. Tateno: J. Phys. Soc. Jpn. **87** (2017) 034804.

First-principles study of ionization and diffusion of metal atoms at metal/solid interfaces in electric fields

Takashi NAKAYAMA
Department of Physics, Chiba University
1-33 Yayoi, Inage, Chiba 263-8522

Metal/solid interfaces are essential structures for various electronic/optical devices. However, metal atoms often diffuse from electrodes into solids such as SiO_2 by the thermal annealing processes and applied electric fields. This diffusion causes serious damage to recently developed nanoscale devices. In this view, the microscopic understanding of diffusion is important, especially in an electric field. However, there is little theoretical work on metal-atom diffusion around metal/solid interfaces. In this works, we studied the ionization and diffusion of various metal atoms in an electric field around metal/SiO_2 interfaces using first-principles calculations.

To simulate the interfaces, we adopt a (2×2) metal/SiO_2 (001) repeated-slab model made of 3-4 ML metal atoms and 16 ML α-quartz SiO_2. We consider eleven metals: Ta, Ag, Pt, Au, Al, Ni, W, Nb, V, Ti, and Cu. The adiabatic diffusion potential of a metal atom from the interface into SiO_2 was calculated by the standard first-principles method in the density functional theory. We employ a primitive method to produce an electric field perpendicular to the interface by simply removing electrons from the present slab system. All atom positions are optimized during the diffusion.

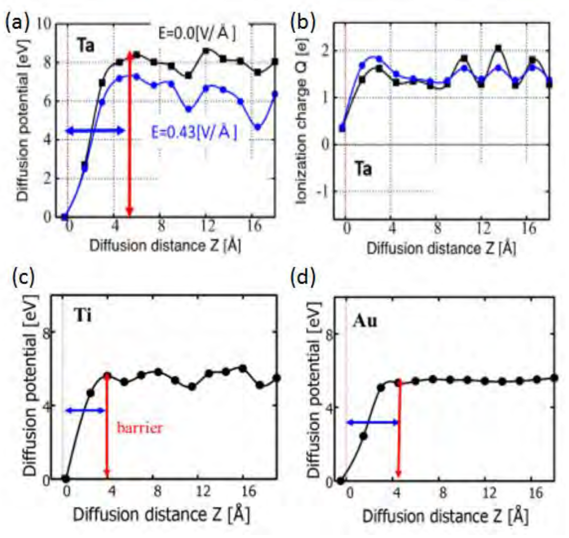

Fig.1. Adiabatic diffusion potentials at metal/SiO_2 interfaces as a function of distance from the interface, for (a) Ta, (c) Ti, and (d) Au atoms. (b) shows the ionization charge of Ta atom during the diffusion. In (a) and (b), the results in an electric field are also shown by blue lines.

Figs. 1(a) and 1(b) show the diffusion potential and ionization charge of the Ta atom, respectively, as a function of the distance z from the Ta/SiO_2 interface, while Figs. 1(c) and 1(d) are the potentials for the Ti and Au atoms. From these figures, we note two features: (1) the diffusion barrier height ϕ_B for penetrating into SiO_2 depends on the kind of atom. Fig. 2(a) shows the relationship between ϕ_B and $-\mu$ (chemical potential of a metal atom in metal). From these analyses, we found that the cohesive energy of metal atom layers is the leading factor for the penetration barrier ϕ_B.

(2) As shown in Figs. 1(a), 1(c), and 1(d), most of the metal atoms show the increase of potential in a similar 0-4 Å region near the interface. This region is closely related to the metal-induced gap states (MIGSs). Fig. 2(b) shows the electron density profile of one MIGS at a clean Ta/SiO_2 interface, and those of the electron-occupied states of a diffusing Ta atom when such a Ta atom is located at z=4.5 and 7.5 Å away from the interface. It is clearly seen that the electronic state of Ta decreases the hybridization with MIGS as the Ta atom leaves the interface. Since the hybridization of the Ta state with MIGS stabilizes the Ta atom, the hybridization with MIGS is the origin of the

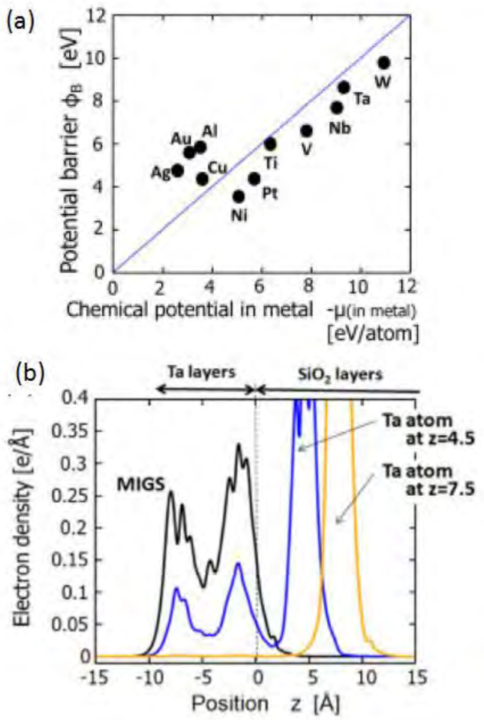

Fig.2. (a) Calculated potential barrier for metal-atom penetration into SiO_2 as a function of metal-atom chemical potential in bulk metal. (b) Electron density profile of original MIGS of Ta metal layers and Ta-atom states around Ta/SiO_2 interface.

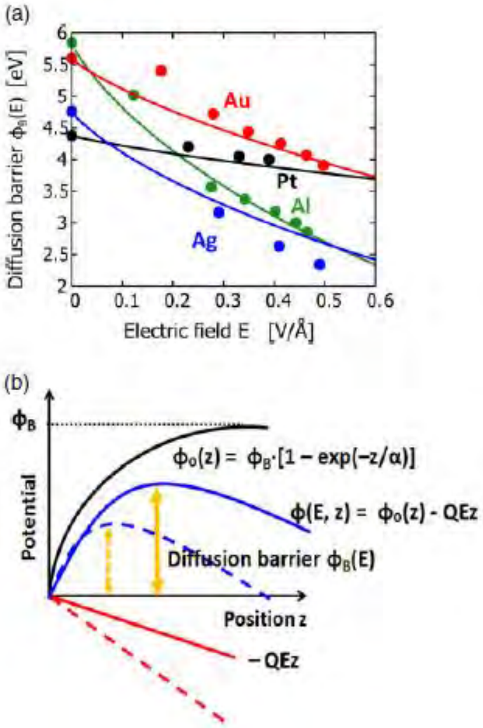

Fig.3. (a) Calculated diffusion barrier for the metal-atom penetration into SiO_2 as a function of electric field. The dots are obtained by first-principles calculations, while the lines are estimated using the model formula. (b) Model potential representing the metal-atom diffusion into insulators in electric fields. $\phi_B(E)$ is the potential barrier, while $\phi_0(z)$ and $-QEz$ are the diffusion potential in the case of no electric field and the electrostatic potential produced by the electric field, respectively. The solid and broken lines represent the cases of small and large electric fields, respectively.

region of potential increase with a similar width.

Next, we consider how the electric field accelerates the metal-atom penetration into SiO_2. Fig. 3(a) shows the diffusion penetration barrier for various atoms as a function of electric field strength. It is seen that the barrier height $\phi_B(E)$ decreases almost linearly with increasing electric field strength. We showed that the diffusion potential and the diffusion barrier in an electric field E are described as $\phi(E, z) = \phi_0(z) - QE$. and $\phi_B(E) = \phi_B - QE\alpha\,[1 - \log(QE\alpha/\phi_B)]$, respectively, as shown in Fig. 3(b). Here, ϕ_B , Q, and α are the potential barrier in the case of no electric field, the ionization charge of metal atom in SiO_2, and the penetration length of MIGS into SiO_2.

In this way, the barrier height $\phi_B(E)$ in an electric field is described by the universal formula, not depending on the kind of substrates and metal atoms. It is interesting to note that the MIGS are known to determine the Schottky barrier height and the defect density at metal/solid interfaces. By the present study, we also demonstrated that the MIGS work to determine the ionization and metal-atom penetration into SiO_2 in electric fields.

All these calculations were performed using the xTAPP, VASP, and pspwf codes. In order to realize the calculations for the present interface systems in electric fields, because the system is made of a large number of atoms (300-1000 atoms), the advanced computing facility having multi-task and higher-speed CPU (more than 64 cores × 2.5GHz), larger-size memory (around 128GB), and larger-size strange (more than 1 TB) is indispensable. These conditions are realized only by the ISSP supercomputing systems.

First-Principles Study on New Group-IV Semiconductor Alloys

Yuki NAGAE[1], Masashi KUROSAWA[1, 2, 3], Masaaki ARAIDAI[1, 2, 4],
Osamu NAKATSUKA[1, 4], Kenji SHIRAISHI[1, 4], and Shigeaki ZAIMA[4]
[1] *Graduate School of Engineering, Nagoya University*
[2] *Institute for Advanced Research, Nagoya University*
[3] *PRESTO, Japan Science and Technology Agency*
[4] *Institute of Materials and Systems for Sustainability, Nagoya University*

Silicon tin ($Si_{1-x}Sn_x$) alloy is a promising material for optical communication of intra- and interchip technology in silicon-based high-performance large-scale integrated circuits due to their preferable energy bandgap (E_g). However, comprehensive understandings of the energy band offset (EBO) with whole composition has not been clarified experimentally due to its low solubility (0.1%) of Sn in Si. In this study, we investigated the EBO of $Si_{1-x}Sn_x$ theoretically and compared it with conventional theoretical and experimental results.

The first-principles calculation was performed using the Vienna ab initio simulation package (VASP) code [1, 2] We used the modified Becke and Johnson (MBJ) exchange potential [3] to avoid the underestimation of E_g in conventional DFT calculation. To consider the electron-ion interaction, we used the PAW potential [4]. The unit cell and k-points were composed of 8 atoms of diamond lattice ($Si_{8-n}Sn_n$, n=0–8) and 2×2×2 mesh, respectively. We considered all of the unique atomic configuration by “Hakoniwa-method” [5], under the structurally relaxed situation in the hydrostatic pressure.

We calculated the charge neutrality level (CNL) of $Si_{1-x}Sn_x$ based on the interface hybridization that induced dipoles to compare the valence band maximum (VBM) for each Sn-content $Si_{1-x}Sn_x$ as the following equation [6],

$$\phi(\mathrm{CNL}) = \mathrm{VBM} + E_g D_{\mathrm{VB}}/(D_{\mathrm{VB}}+D_{\mathrm{CB}}),$$

where D_{VB} and D_{CB} correspond to the density of states (DOS) of valence and conduction bands, respectively. Figure 1 shows EBO of $Si_{1-x}Sn_x$ relative to Si with setting CNL of each $Si_{1-x}Sn_x$ as an equal level. The broken line represents a linear approximation of the referenced conventional conduction band minimum (CBM) and VBM between Si and α-Sn from the previous report [7]. We estimated a bowing parameter of 1.15 ± 0.02eV. The obtained Sn content dependence of VBO showed a similar tendency to the experimental results of $Si_{1-x}Sn_x$ with Sn content ranging between 0 and 40% [8,9], which cannot be ignored for designing band alignment. By estimating the energy band offset using calculations of *E*–*k* dispersion and the VBO, we could estimate the dependences of the VBM and CBM in the entire Sn content range not only in the low-Sn-content region.

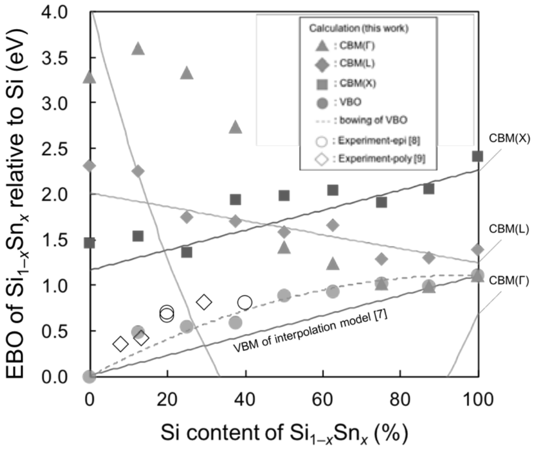

Fig. 1: EBO of $Si_{1-x}Sn_x$ relative to Si as a function of the Sn content. Solid lines show VBO and CBMs from previous report by Sun [7]. For the calculation results, the VBO and the CBMs at the Γ, L, and X valleys are shown as circles, triangles, diamonds, and squares, respectively. Experimental [8,9] and calculation results [10] are shown as opened and closed symbols, respectively. Copyright 2017 The Japan Society of Applied Physics [10].

References

[1] G. Kresse and J. Furthmüller, Phys. Rev. B **54**, 11169 (1996).

[2] B. Adolph, J. Furthmüller, and F. Bechstedt, Phys. Rev. B **63**, 125108 (2001).

[3] A. D. Becke and E. R. Johnson, J. Chem. Phys. **124**, 221101 (2006).

[4] P. E. Bröchl, Phys. Rev. B **50**, 24 (1994).

[5] K. Sueoka, E. Kamiyama, and J. Vanhellemont, J. Appl. Phys. **114**, 153510 (2013).

[6] M. Cardona and N. E. Christensen, Phys. Rev. B **35**, 6182 (1987).

[7] G. Sun, R. A. Soref, and H. H. Cheng, J. Appl. Phys. **108**, 033107 (2010).

[8] M. Kurosawa, M. Kato, K. Takahashi, O. Nakatsuka, and S. Zaima, Appl. Phys. Lett. **111**, 192106 (2017).

[9] M. Kurosawa, M. Kato, T. Yamaha, N. Taoka, O. Nakatsuka, and S. Zaima, Appl. Phys. Lett. **106**, 171908 (2015).

[10] Y. Nagae, M. Kurosawa, M. Araidai, O. Nakatsuka, K. Shiraishi, and S. Zaima, Jpn. J. Appl. Phys. **56**, 04CR10 (2017).

van der Waals density functional theory study of molecular adsorption on solid surfaces

Ikutaro HAMADA

Department of Precision Science and Technology, Graduate School of Engineering,
Osaka University, 2-1 Yamada-Oka, Suita, Osaka 565-0871

Molecular adsorption on the electrode surface is one of the important building blocks in diverse devices relevant to energy harvesting and storage, such as fuel cell, solar cell, and secondary battery, to name only a few. The accurate description of the molecular adsorption is challenging in the conventional density functional theory based on the local density and generalized gradient approximations, because they are static and local, and cannot capture the dynamic and nonlocal nature of the van der Waals interaction, which is crucial in the molecule-surface interaction. In this work, we use rev-vdW-DF2[1], an offspring of the van der Waals density functional (vdW-DF)[2], which has been show to describe the molecular adsorption on solid surfaces accurately.

All the calculations were performed using the STATE code[3], which employs ultrasoft pseudopotentials and plane wave basis set. The surfaces was modeled by a slab. Molecules are put on one side of the slab, and the spurious electrostatic interaction with image slabs was eliminated by using the effective screening medium method[4]. We used an efficient algorithm[5] of the self-consistent vdW-DF.

In this work I put emphasis on a polycyclic aromatic hydrocabon adsorbed on a metal surface, namely, diazuleno[1,2-c:2′,1′-g]phenanthrene (DAPh) and on the Cu(001) surface, and investigate the adsorption state and the on-surface reactions observed in the experiment[6]. As a first step, I investigated the adsorption site for the reactant and product and obtained the most stable adsorption sites in good agreement with the experiment. The investigation of the reaction mechanism is underway.

References

[1] I. Hamada: Phys. Rev. B **89** (2014) 121103(R)

[2] M. Dion et al., Phys. Rev Lett. **92** (2014) 246401.

[3] Y. Morikawa, H. Ishii, and K. Seki: Phys. Rev. B. **64** (2004) 041403.

[4] M. Otani and O. Sugino: Phys. Rev. B **73** (2006) 115407.

[5] J. Wu and F. Gygi: J. Chem. Phys **136** (2012) 224107.

[6] A. Shiotari et al. Nat. Commun. 8 (2017) 16089.

Hydrogen state in a rutile titanium dioxide by first-principles calculation

Kanako YOSHIZAWA
Research Organization for Information Science and Technology,
Kobe, Hyogo 650-0047

Titanium dioxide (TiO_2) has attracted increasing attention in recent years due to its numerous technological applications, such as photocatalysts, photovoltaics, and devices. Impurity hydrogen (H) and oxygen vacancy (V_O) affect electronic properties of TiO_2 and we study the effect of H doping of it. It is known that the electrons can localize at Ti 3d orbitals, forming Ti^{3+} ions [1, 2]. The trapped electrons form small polarons that consist of the electrons coupled to the distortion of the lattice around the Ti^{3+} ions.

We examine the electronic structure of H in rutile TiO_2 by using DFT calculation. We calculated using VASP package [3] on System B in ISSP. The large scale calculation was carried in 216-atom supercell with HSE hybrid functional in DFT. The spin density for a localized electron in Ti site exists and it is verified that the excess electrons are described as localized small polarons by DFT calculation.

We also understand H behavior by calculating the isotropic and anisotropic hyperfine coupling constants. Because muonium in crystals behaves similarly to H, muon spin rotation (μSR) has played an important role in identification of hydrogen-like states in TiO_2. We evaluate the accuracy of DFT calculation for H in TiO_2 by the comparison with hyperfine parameters of μSR [4] in the structure shown as the figure. As shown in the table, the hyperfine parameters of DFT calculation has anisotropy, the DFT calculation and μSR are qualitatively the same.

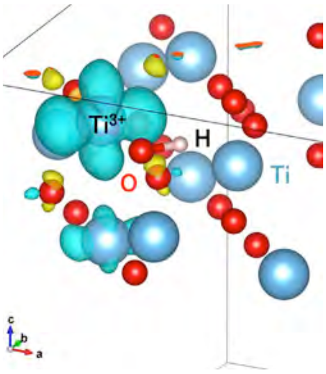

Figure: The position of Ti^{3+} ions (same structure as μSR [4]).

[MHz]	Axx	Ayy	Azz
H	−15.231	−13.761	26.074

Table: Hyperfine parameters of DFT calculation (gyromagnetic ratio $\gamma = 135.53$ MHz T^{-1})

References

[1] A. Janotti, C. Franchini, J. B. Varley, G. Kresse, and C. G. Van de Walle, Phys. Status Solidi RRL **7**, 199 (2013).

[2] F. Filippone, G. Mattioli, P. Alippi, and A. Amore Bonapasta, Phys. Rev. B **80**, 245203 (2009).

[3] http://www.vasp.at.

[4] K. Shimomura, R. Kadono, A. Koda, K. Nishiyama, and M. Mihara, Phys. Rev. B **92**, 075203 (2015).

First-principles theoretical study on ionization energy and electron affinity of organic semiconductors: Role of the electrostatic interaction

Susumu Yanagisawa
Department of Physics and Earth Sciences, Faculty of Science, University of the Ryukyus
1 Senbaru, Nishihara, Okinawa 903-0213

Ionization energy (IE) and electron affinity (EA) of organic semiconductor (OSC) are important quantities dominating charge injection barrier. Experimentally, IE (EA) is determined as the energy difference between the highest occupied (lowest unoccupied) energy level and the vacuum level. It was proposed that the orientation of the constituent organic molecules at the surface crucially affects IE and EA[1]. The electrostatic interaction such as the charge-permanent quadrupole interaction was proposed to be of importance[2].

In this study, using the periodic slab model of the OSC surface with the semi-local density functional theory (DFT) calculation, the surface facet or molecule orientation-dependent IE and EA of the pentacene polymorphs (see Fig. 1) were theoretically determined [3]. For DFT calculations, STATE code was used[4]. For accurate treatment of the induced polarization upon the injected charge in the bulk, the many-body perturbation theory within the GW approximation was employed. For the calculation of the bulk with the one-shot GW, the GW space-time code[5] was used. To gain insights into the polarization energy in terms of the electrostatic and induced polarization contributions, a following strategy was employed:

- The electrostatic term (W^+/W^-) was estimated by the energy difference in highest occupied/lowest unoccupied level between the isolated molecule and the periodic slab.
- The induced polarization terms E_P^+ and E_P^- were assumed to be of the same magnitude, and thus were estimated as half of the difference in transport gap between the isolated molecule and the bulk system.

The polarization energies P^+ and P^- upon the injected hole and electron, respectively, were determined as

$$P^+ = E_\mathrm{P}^+ + W^+, \tag{1}$$

$$P^- = E_\mathrm{P}^- + W^-. \tag{2}$$

The calculation was done for IE and EA of the different polymorphs of pentacene, i.e. thin-film and single crystal phases in which the molecules are standing and lying on the substrate, respectively[6]. The thickness of the slab treated with DFT was three (seven) monolayer for the thin-film (single crystal) phase, and the energy of their highest occupied/lowest unoccupied level was determined as average of the valence band/conduction edge energies over the Brillouin zone. For the fundamental gap or IE and EA of the isolated molecule, the experimental values were used[7].

Table 1 shows the calculated IE and EA for the facets of the pentacene polymorphs. The result is in agreement with the experiments. The IE and EA are found to be similar to those determined by the recent theoretical approach

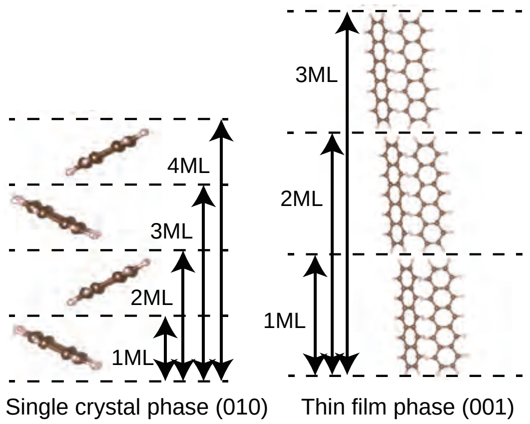

Figure 1: Schematics of the pentacene polymorphs

Table 1: Ionization potential (IP) and electron affnity (EA) of the pentacene polymorphs depending on the facets. Experimental results[8] are in parentheses.

	Pentacene	
	Thin film (001)	Single crystal (010)
IE	4.80 (4.90)	5.25 (5.45)
EA	2.31 (2.35)	2.83 (3.14)

at the same level of theory, in which the electrostatic potentials of the slab and the bulk were aligned[9].

Fig. 2 displays the polarization energies P^+/P^- for the polymorphs in terms of E_P and W. It is found that the different polarization energies for the different facets come from the electrostatic terms W^+/W^-, while the E_P are similar. The different charge-permanent quadrupole interaction for the standing/lying pentacene (see Fig. 1) dominates the different electrostatic contribution[2].

Overall, this work demonstrates the impact of the electrostatic terms affecting the IE and EA of OSC, which seems to come from the molecular orientation at the surface. The same approach has been also applied to elucidation of the measured IE and EA in thin films of a pentacene derivative[10].

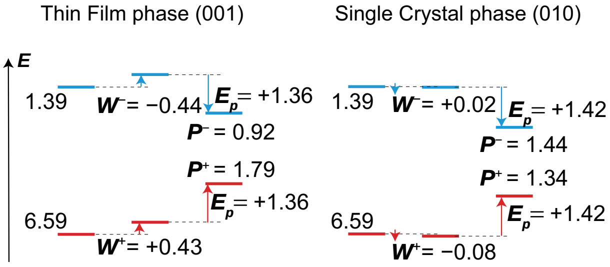

Figure 2: Effects of the electrostatic and the induced polarization terms on the polarization energies

References

[1] G. Heimel et al.: Nat. Chem. **5** (2013) 187.

[2] B. J. Topham and Z. G. Soos: Phys. Rev. B **84** (2011) 165405.

[3] S. Yanagisawa: AIP Conf. Procs. **1906** (2017) 030014.

[4] Y. Morikawa, H. Ishii, and K. Seki: Phys. Rev. B **69** (2004) 041403(R).

[5] M. M. Rieger et al.: Comput. Phys. Commun. **117** (1999) 211.

[6] T. Siegrist et al., Angew. Chem. Int. Ed. Engl. **40** (2001) 1732; H. Yoshida, K. Inaba, and N. Sato, Appl. Phys. Lett. **90** (2007) 181930.

[7] V. Coropceanu et al.: Phys. Rev. Lett. **89** (2002) 275503; L. Crocker, T. B. Wang, and P. Kebarle: J. Am. Chem. Soc. **115** (1993) 7818.

[8] H. Yoshida et al.: Phys. Rev. B **92** (2015) 075145.

[9] Y. Kang, S. H. Jeon, Y. Cho, and S. Han: Phys. Rev. B **93** (2016) 035131.

[10] K. Yamada, S. Yanagisawa, T. Koganezawa, K. Mase, N. Sato, and H. Yoshida, submitted to Phys. Rev. B.

Controlling magnetic properties of the quantum-well induced ferromagnetism in Pd(100) through the lattice distortion

Yusuke BAN[1], Hiroyuki KAGESHIMA[2], and Tetsuya SATO[1]

1Department of Applied Physics and Physico-Informatics, Keio University, 3-14-1 Hiyoshi, Kohoku-ku, Yokohama 223-0061, Japan

2Interdisciplinary Graduate School of Science and Engineering, Shimane University, 1060 Nishikawatsu-cho, Matsue 690-8504, Japan

Recently, we found the appearance of ferromagnetism in the ultrathin film of Pd(100) based on d-electron quantum-well states[1]. Moreover, it was revealed that the saturation magnetization of the Pd (001) ultrathin film changed accompanied by the structural phase transition of the $BaTiO_3$ substrate. In order to clarify the magnetization change accompanied by a phase transition of $BaTiO_3$, we performed the density functional calculation for distorted Pd films using the PHASE/ 0 program [2].

In the calculation, we used the pseudopotential method and LDAPW92 to the exchange and correlation interactions. A slab of vacuum (two monolayers) /Pd (N monolayers) /vacuum (three monolayers), 56 × 56 × 1 k-points, and 36Ry of cut-off energy were used. First, we calculated the out of plane lattice constant of Pd to obtain the lowest energy under the condition that the in-plane lattice constant is consistent with that of $BaTiO_3$ substrate. Changes in the magnetization of Pd (001) induced during the structural phase transitions of $BaTiO_3$ substrate were calculated. The change in magnetization is consistent with the experiment suggesting that the strain caused by the structural phase transition of $BaTiO_3$ modulates the magnetism. In order to investigate the mechanism of magnetization change accompanying strain, DOS was calculated considering strain effect. Near the Fermi energy, steep changes in the DOS were observed. This suggests that a slight change in the electronic structure of Pd(001) can induce a change in magnetization.

Based on this study, the relation between metallic ferromagnetism induced by the quantum well states and strain can be understood from the viewpoint of electronic structure. In addition this indicates the possibility to realize a multiferroic ~~devices~~ for magnetic switching using strain as an external field.

References

[1] S. Sakuragi *et al.*: Phys. Rev. B **90** (2014) 054411.

[2] Y.Ban *et al.*: Appl. Phys. Lett. **112** (2018) 142409.

Ab initio study of viscosity and local structures of basaltic melt under high pressure.

Satoshi OHMURA

Research Center for Condensed Matter Physics / Department of Environmental and Civil Engineering,

Hiroshima Institute of Technology Saeki-ku, Hiroshima, 731-5143

We have studied static and dynamical properties of covalent liquids under high-pressure and high-temperature conditions by *ab initio* molecular dynamics (MD) simulations. This year, we applied *ab initio* MD simulations to basaltic melt and investigated dynamical properties such as viscosity under high pressure conditions. The simulations have been done in System B in ISSP.

High-pressure behavior of basaltic aluminosilicate melt has been intensively studied due to its importance in deep Earth science related to such as early magma ocean and subsequent differentiation processes.

Recently, experimental studies reported that the viscosity of basaltic melt decreases with increasing pressure [1]. They suggested that this anomalous behavior is related to the coordination change of Al. However, so far, there exist no *ab initio* simulations of basaltic melt in the pressure range, where the anomaly in viscosity is observed experimentally.

In this study, we therefore performed *ab initio* MD simulations with gradually changing volume. We calculated the pressure dependence of the viscosity and successfully reproduced a viscosity minimum in the pressure range corresponding to the experiments. We also analyzed the atomic local-structures in the melt under pressure. The obtained pressure dependence of density and radial distribution functions do not show drastic structural changes and the coordination number around Si and Al increase continuously with increasing pressure. However, the coordination number around Al atoms increases more rapidly than that around Si atoms. We also investigated pressure dependence of atomic diffusion. It was clarified that pressure enhances atomic diffusion up to 5 GPa. However, when pressure is over 5 GPa, atomic diffusion becomes suppressed by pressure effects. From the atomic diffusion mechanism observed in the simulations, we clarified a relationship between the anomalous pressure dependence of viscosity and variations in the atomic-scale local structure.

[1] T. Sakamaki *et al.*, Nature Geoscience **6**, 1041 (2013).

First-Principles Study of Electronic Structures of Energy Device Materials

Hiroyoshi MOMIDA, Motoyuki HAMAGUCHI, Hiroshi KATSUMOTO
Institute of Scientific and Industrial Research, Osaka University
8-1 Mihogaoka, Ibaraki, Osaka 567-0047

We have studied electronic and atomistic properties of materials, which are used in energy storage and conversion devices, by the first-principles calculations. As to the energy storage materials, we have investigated electrode properties of the transition-metal (TM) fluoride and oxide materials for Li-ion and Na-ion batteries [1, 2]. Piezoelectric materials can be used for an energy conversion between mechanical and electric ones, and we have studied piezoelectric properties of wurtzite materials [3]. Related to this subject, mechanical properties of 5d-TM carbides have been studied by the first-principles calculations [4]. We have studied topological electronic properties in a layered material consisting of strong- and non-topological insulators using the supercomputer system in the last fiscal year, and the result is published recently in a journal [5].

1. Cathode properties of $\mathbf{Li_2}M\mathbf{TiO_4}$ (M = 3d TMs) for Li-ion batteries [2]

Cathode properties of $Li_2M TiO_4$ (M = V, Cr, Mn, Fe, Co, and Ni) for Li-ion batteries have been studied by the first-principles calculations. Structure stabilities and voltage–capacity curves for $Li_{2-x}MTiO_4$ ($0 \le x \le 2$) models with the rock-salt-based structures are calculated considering several Li concentration ($2-x$). It is found that battery reaction mechanisms associated with redox reactions of M and O dominates mainly in the ranges of lower and higher x, respectively. The O redox reactions can destabilize atomic structures in the higher x region, because the electron removal from O-p states produces high peaks at the Fermi level in the density of states. We actually calculate the structural stability of O using the models with O deficiency, and the result shows that O can be released easier than Li in the higher x region. We estimate the critical Li concentration (x_c) at which the vacancy formation energy of O becomes lower than that of Li, and find that the critical x value decreases with increasing number of 3d electrons as M changes from V to Ni. The O dissociations from the cathodes degrade the battery performance, because the calculated voltages of Li_2MTiO_4 with O deficiency are lower than those without O deficiency. Our systematic study for the series of M predicts that Li_2CrTiO_4 can be the best cathode material considering its cathode properties of high voltage and stability against O dissociation.

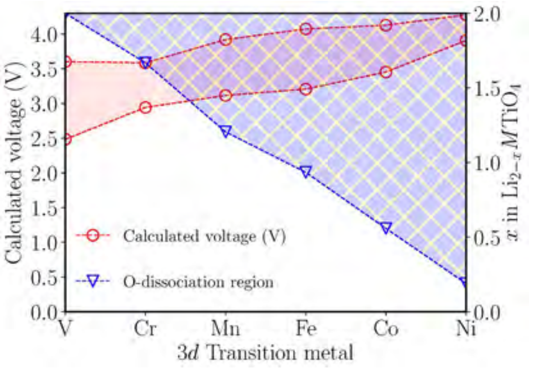

Figure 1: Calculated voltage ranges (circles) and the critical Li concentration x_c (triangles) in $Li_{2-x}MTiO_4$ (M = 3d TMs) [2].

2. Piezoelectricity of wurtzite materials: First-principles and statistical-learning calculations [3]

We calculate piezoelectric e constants along the c axis (e_{33}) by the first-principles method for more than a dozen of binary wurtzite materials, which are listed in the Inorganic Crystal Structure Database (ICSD). We investigate a relationship between e_{33} and several materials parameters using the statistical learning methods. It is theoretically shown that wurtzite materials with high e_{33} generally have small lattice constant ratios (c/a) almost independent of constituent elements, and approximately expressed as $e_{33} = -A[c/a-(c/a)_0]$ (in the c/a ranges higher than about 1.3) with the ideal lattice constant ratio $(c/a)_0 \sim 1.633$ and a constant parameter $A > 0$. We also find the better description of $e_{33} = -A' Z_v [c/a-(c/a)_0]$ (in the c/a ranges higher than about 1.3) with nominal ionic valences Z_v. This relation also holds for ternary materials such as $Sc_xAl_{1-x}N$. Based on the above relation, we have conducted a search for highly piezoelectric wurtzite materials by identifying materials with smaller c/a values. It is theoretically proposed that the piezoelectricity of ZnO can be enhanced by substitutions of Zn with Ca.

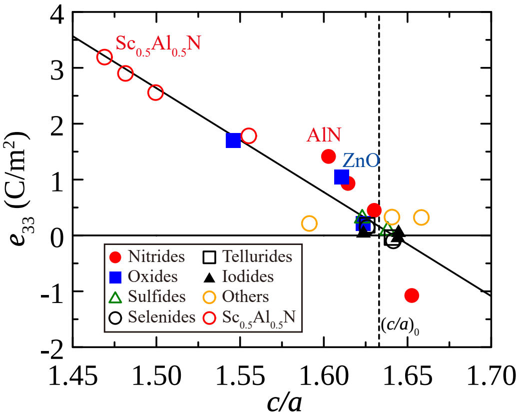

Figure 2: Piezoelectric e constants (e_{33}) versus lattice constant ratios (c/a) calculated for binary wurtzite materials listed in ICSD and $Sc_{0.5}Al_{0.5}N$ models [3].

References

[1] A. Kitajou, Y. Ishado, T. Yamashita, H. Momida, T. Oguchi and S. Okada, Cathode properties of perovskite-type $NaMF_3$ (M = Fe, Mn, and Co) prepared by mechanical ball milling for sodium-ion battery, Electrochimica Acta **245** (2017) 424.

[2] M. Hamaguchi, H. Momida and T. Oguchi, First-principles study on cathode properties of Li_2MTiO_4 (M = V, Cr, Mn, Fe, Co, and Ni) with oxygen deficiency for Li-ion batteries, J. Phys. Soc. Jpn., in press.

[3] H. Momida and T. Oguchi, Effects of lattice parameters on piezoelectric constants in wurtzite materials: A theoretical study using first-principles and statistical-learning methods, Appl. Phys. Express **11** (2018) 041201.

[4] M. Fukuichi, H. Momida, M. Geshi, M. Michiuchi, K. Sogabe and T. Oguchi, First-principles calculations on the origin of mechanical properties and electronic structures of 5d transition metal monocarbides MC (M = Hf, Ta, W, Re, Os, Ir, and Pt), J. Phys. Soc. Jpn. **87** (2018) 044602.

[5] H. Momida, G. Bihlmayer, S. Blügel, K. Segawa, Y. Ando and T. Oguchi, Topological interface states in the natural heterostructure $(PbSe)_5(Bi_2Se_3)_6$ with Bi_{Pb} defects, Phys. Rev. B **97** (2018) 035113.

Ab initio molecular dynamics study of static structure of glasses

Akihide KOURA
Student Affairs Department,
Kumamoto University, Kurokami, Kumamoto, Kumamoto 860-8555

We have studied static structure, electronic and dynamic properties of liquid, crystal, and glassy systems. In this project, we focused on the static structure of network forming glasses under pressure by using *ab initio* molecular dynamics simulations.

In this project, we have studied the static structure of liquid GeTe and liquid GeSe under pressure, and the static structure of the densified $GeSe_2$ glass. The study of the pressure dependence of the static structure on the liquid GeTe was published [1].

On the static structure of the densified glass $GeSe_2$, there is a different point comparing with that of the densified SiO_2 glass. In the densified SiO_2 glass, although the local structure is quite similar to the ordinary glass, the intermediate range order is different. Using ring analysis, the number of small rings increases in the densified glass [2]. On the other hand, in the densified $GeSe_2$ glass, the peak of bond angle distribution shifts from approximately 108° in the ordinary glass to 90° in the densified glass. The fact means the deformed tetrahedral units remains after depressurization. Using the ring analysis, which is more complicated than that in SiO_2 case because of the existence of Ge-Ge and Se-Se homo-polar bonds, it is shown that the tendency of decrease number of large size ring is the same as that in SiO_2. These features are supported by various covalent bond strengths.

We have also studied the pressure dependence of the static structure of liquid GeSe. The pressure and temperature ranges are from 0 to 240 GPa and 1000 to 4500 K, respectively. At ambient pressure, liquid GeSe shows the semiconducting property. With increasing pressure, the semiconductor-metallic (SCM) transition occurs between about 8 and 12 GPa. On the other hand, numbers of three- and five-fold coordinated Ge to Se atoms decrease and increase at about 12 GPa, respectively. The structural change and the SCM transition suggest that the Peierls-type distortion is completely dissolved at this pressure range.

References

[1] A. Koura and F. Shimojo: EPJ Web of Conferences **151,** 01002 (2017).

[2] E. Ryuo, D. Wakabayashi, A. Koura, and F. Shimojo, Phys. Rev. B **96** (2017) 054206.

First-principles meta-dynamics analysis of Catalyst Referred Etching method

– Analysis on dissociative adsorption of water molecule and etching reaction at interface between Pt and material surface –

Kouji Inagaki

Graduate School of Engineering, Osaka University
Yamadaoka 2-1, Suita, Osaka 565-0871

Atomic-level planarization of hard-to-work materials such as wide-band gap semiconductors has attracted much attention for a power electronic devices. Recently, a newly developed wet chemical surface planarization technique named CARE (Catalyst-Referred Etching) [1] realizes step-and-terrace shaped smoothened surfaces, only by wiping work surface with a catalytic metal plate in an etching solution. At present, as the etchant and the catalyst, dangerous and toxic concentrated hydrogen fluorine aqueous solutions and expensive Pt plates are utilized for etchant and catalyst, respectively. It is important to clarify the reaction process in the atomic level in SiC-HF-Pt system to find out alternative, effective and practical etchant and catalyst materials.

In this project, we performed first-principles reaction path calculations on the initial stage of the etching process, as well as developed a new metadynamics method for reaction path analysis with no initial knowledge. All reaction analyses for former theme were performed using a program package ‘STATE’ (Simulation Tool for Atom TEchnology) [2]. Reaction process for SiC-H_2O-Pt[3] and GaN- H_2O-Pt systems are investigated.

In the SiC analysis, the role of Pt as catalyst in the dissociative adsorption of a water molecule as an elemental reaction of the process is discussed from a viewpoint of chemical and mechanical interactions. It was shown from calculations that the distance between SiC work surface and Pt catalyst found to play an important role to the reaction barrier height. The chemical stabilization by forming Pt-O-Si bond and destabilization by mechanical distortion show different tendency for the initial, metastable and final structures against the distance; formation of multiple bonds both at Si-O-Pt and Si-SiC substrate in a metastable state make system rigid and sensitive to the distance while the other cases (initial and final) contains less number of bonds and become flexible. Therefore, the barrier becomes low at a particular distance between Pt and SiC surfaces.

In the development of a new metadynamics method, we proposed a new method for stacking penalty potential in which the potential height and width are simultaneously expanded or shrunk with the kinetic energy corresponding to the freedom which we are interested in, with considering that system has larger kinetic energy at lower potential energy. The test program built with Fortran and Lammps and the efficiency of the method is tested. It was shown that the method basically works well and possibility for higher performance than previous method is clarified.

References

[1] H.Hara, et al., J.Electron.Mater. **35** (2006) L11.
[2] Y. Morikawa, Phys. Rev. B **63** (2001) 033405.
[3] P.V. Bui, D. Toh, A. Isohashi, S. Matsuyama, K. Inagaki, Y. Sano, K. Yamauchi, and Y. Morikawa, Jpn. J. Appl. Phys. 57, 055703 (2018).

Ab initio studies toward functional nanomaterials based on abundant elements

Tetsuya TAKETSUGU
Faculty of Science, Hokkaido University
N10W8, Sapporo, Hokkaido 060-0810

Ab initio studies on various nano materials are crucial to understand and design new functional materials with abundant elements. Heterogeneous catalysts used in automotive gas exhausts control, water gas shifts, and fuel cells rely mostly on the precious metals (PMs) such as Pt, Rh, Pd. Platinum and palladium are also used for hydrogen based energy strategies. Due to their high cost and limited amounts, to reduce or even replace these metals is emergent issues in industry. To that end, we perform density functional theoretical (DFT) computations under the periodic boundary conditions together with projector augmented wave method with VASP using ISSP supercomputers to gain chemical insights.

Concerning the automotive catalysis, NO is reduced while CO and CH (hydrocarbons) are oxidized at the same time under the drastic temperature and oxygen concentration changes. With such extreme conditions, only Pt, Rh, and Pd turned out to be effective. To understand the reason as well as to clarify the possible chemical reaction pathways for TWC, we focus on the NO reduction reaction at the Pd surface and perform DFT calculations at the generalized gradient approximation level. Adsorption of NO, CO, O_2, as well as O to various Pd surfaces such as (111), (100), steps, and edges are studied and then nudged elastic band calculations are performed to study NO reduction reactions. We have also studied CO adsorption onto Pt surfaces by using hybrid functionals of HSE06 for a 4-layer slab of 2 by 2 super cells. As for the abundant elemental nano catalysis, we have studied structural and electronic properties of 3d transition metals (TM^{3d}) supported by an oxide surface. Electronic properties of optimized structures for one TM^{3d} atom doping with pristine and O-defective oxide substrates are studied and some adsorption states of small molecules are obtained. Here, for calculations including transition metals with localized f-electrons, we used DFT+U technique to account for the localized electrons. We have also tried hybrid functionals such as HSE06 but using those functionals for a large TM/Oxide surface turned out to be computationally too demanding to the present purpose.

On the hydrogen storage materials, we study PdAu alloy materials, to complement a hydrogen uptake and release experiment using thin films of Au:Pd alloys. DFT calculations are performed for Au:Pd alloy thinfilms modeled by alternating Au and Pd layers in 2-by-2 manner in the $\langle 001 \rangle$ direction using the unit cell consisting of Au_4Pd_4 and 1-by-2 in the $\langle 111 \rangle$ direction using unit cell consisting of $AuPd_2$. Density of states are obtained using a $21 \times 21 \times 11$ k-point meshes with the curoff energy of 500 eV.

References

[1] Y. Nishijima, S. Shimizu, K. Kurihara, Y. Hashimoto, H. Takahashi, A. Balcytis, G. Seniutinas, S. Okazaki, J. Juodkazyte, T. Iwasa, T. Taketsugu, Y. Tominaga, and S. Juodkazis, Optics Express, 25, 24081 (2017).

Ab-initio Study on Amorphization Dynamics and Ion Diffusion in Biogenous Iron Oxide

Kenji TSURUTA, Keiichi MITANI, Satoshi OHMURA[a], and Atsushi ISHIKAWA

Graduate School of Natural Science and Technology, Okayama University, Okayama 700-8530
[a] Department of Civil and Environmental Engineering, Hiroshima Institute of Technology, Hiroshima 731-5193

The chemical versatilities of nanostructured iron oxide (n-FeO) have long been attracting attention in the research of functional materials. Since ordinary synthesis of intrinsic n-FeO involves high-temperature processes and many of experimental observations have proven that n-FeOs possess amorphous structure, rapid and low-temperature generation of stable amorphous iron oxides is important for industrial applications. In the field of the microbiology, on the other hand, it has long been known that iron oxidizing bacteria, called *Leptothrix ochracea*, produces an iron oxide sheath. The recent reports have shown [1] that the sheath produced by the bacteria consists of agglomerated iron oxide nanoparticles of ~3 nm diameter with an amorphous structure involving uniformly distributed non-stoichiometric composition of Fe,O, Si, and P. It also suggests that amorphous iron oxide can be formed under the ambient temperature with the doping condition. Detailed mechanisms how the bacteria can produce the amorphous nanostructure under the conditions are yet elusive.

In the present work, we performed a first-principles molecular dynamics (FPMD) study on the models of a glassed iron oxide (GIO) and a non-stoichiometric iron oxide (NIO); the former is an amorphous derived from molten iron oxide [2], the latter is a hematite codoped with Si and P, which has been inspired by the aforementioned biogenous iron oxide.

In order to evaluate local bond order and orientational correlations, we calculated the local bond-orientational order parameter w_l and bond-angle correlation function, proposed by Steinhardt *et al.* for each atomic species. The parameter w_l can specify the symmetry of a particular cluster. Since the maximum/minimum values of the w_4 and w_6 are rigorously known, one can grasp a cluster shape and its fluctuations visually by plotting their instantaneous values into the (w_4, w_6)-plane, as depicted in Fig. 1. Also, the inter-cluster correlation based on the Landau theory of bond-orientational free energy (BOF), are applied to these models, and we consequently show that the GIO and NIO are unexpectedly the same structure despite their totally different fabrication processes. The BOF analysis revealed that the compositional changes of the hetero-oxide clusters caused the increase of their pair correlation entropy, and in turn triggered their network topology fluctuation such as a transformation of the sharing form. We thus concluded that the incipient formation of hetero-oxide clusters is essential in the rapid amorphization process and has been a hidden route of the amorphization under the ambient condition [3].

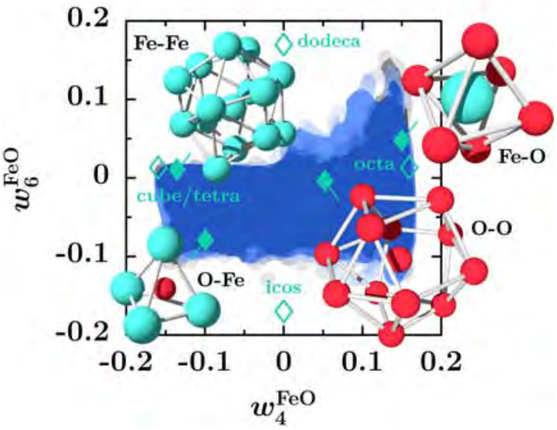

Fig. 1: Local bond-orientational order parameters (w_l) of Fe-O clusters. The gray and blue regions indicate the probability density in the FPMD trajectory for GIO and NIO, respectively.

References

[1] H. Hashimoto *et al.*, ACS Appl. Mater. Interface **6**, 5374-5378 (2014).

[2] M. Misawa, S. Ohmura, and F. Shimojo, J. Phys. Soc. Jpn. **83**, 105002 (2014).

[3] K. Mitani, S. Ohmura, A. Ishikawa, and K. Tsuruta, submitted.

First-principles calculation of solid oxygen using the vdW-DF+U method

Shusuke KASAMATSU
Institute for Solid State Physics, University of Tokyo
Kashiwa-no-ha, Kashiwa, Chiba 277-8581

Solid O_2 is a unique molecular crystal system in that it is comprised of elementary molecules carrying spin $S = 1$. In this system, magnetic and van der Waals (vdW) interactions compete with each other leading to a feature-rich temperature-pressure phase diagram with a variety of structural/magnetic phases. In addition, it It was shown recently that ultra-high magnetic fields can also induce a structural/magnetic phase transition to a previously unknown Θ phase [1]. Support from first-principles density functional theory (DFT) calculations is highly desired for understanding such phase transition behavior. However, it is known that conventional semilocal functional approximations fail rather miserably in describing the experimentally well-known ground state monoclinic α phase of solid O_2. This failure isn't surprising considering the lack of nonlocal correlation in semilocal functionals. However, even recently-developed vdW-DF functionals show only marginal improvement. This has been attributed to the inaccuracy in the description of the magnetic interaction, i.e., overbinding of antiparallel-spin O_2 pairs compared to parallel-spin pairs. Attempts have been made to build in the correct spin-polarization dependence into the vdW-DF functionals, but with limited success [2].

In this work, we took an alternative approach of employing the DFT+U approach to correct for such overpairing of antiparallel spins. The vdW-DF-optB86b functional applied to α-O_2 predicts lattice constants that differ by as much as 30% from experiment. We found that by combining this functional with DFT+U, all monoclinic lattice constants improve continuously with increasing U_{eff} up to $U_{\mathrm{eff}} = 12$ eV. At $U_{\mathrm{eff}} = 12$ eV, the calculated values are all within 2.1% of experiment, which is the best description of α-O_2 thus far achieved in the literature using DFT. The effect of the U_{eff} parameter was examined in detail using chemical bonding analysis. We also calculated the candidate Pa$\bar{3}$ structure for the high-field Θ phase, and the energetics are consistent with the experimentally measured critical field for the phase transition. Details are given in Ref. [3].

References

[1] T. Nomura *et al.*: Phys. Rev. Lett. **112** (2014) 247201.

[2] M. Obata I. Hamada, and T. Oda: Phys. Proc. **75** (2015) 771.

[3] S. Kasamatsu, T. Kato, and O. Sugino: Phys. Rev. B **95** (2017) 235120.

First principles study of Pt clusters adsorbed on graphene edges

Yuji HAMAMOTO
Department of Precision Science and Technology,
Osaka University, Yamada-oka, Suita, Osaka 565-0871

Today, researchers are exploring the possibilities of industrial applications of graphene due to its exceptional electronic and structural properties. One of the most promising candidates is the application of graphene as a support material for metal nanoparticle catalysts. Experimentally, it has been demonstrated that Pt clusters supported on graphene displays higher catalytic activity than those on conventional support materials such as carbon black [1]. A possible scenario for the enhanced catalytic activity of Pt clusters on graphene is that carbon monoxide (CO) tolerance of Pt clusters is improved by strong interactions with the graphene support. So far we have taken lattice vacancies in graphene as an origin of such interactions, where Pt clusters take various adsorption structures depending on the size of vacancies.

Similar strong Pt-graphene interactions can be realized if one consider the adsorption of Pt clusters on the edges of graphene nanoribbons. As a simple examples of such systems, we show Pt atoms adsorbed on zigzag edges of graphene in Figs. 1(a) and (b). As a result of the difference in the coordination numbers, the Pt adsorption energies for structures (a) and (b) are calculated to be -5.04 and -6.28 eV, respectively, indicating that structure (b) is much more preferable than (a). To investigate the CO tolerance of these systems, we also consider CO adsorption on Pt as shown in Figs. 1(c) and (d). The calculated CO adsorption energies for structures (c) and (d) are -2.10 and -1.35 eV, respectively. This suggests that the highly coordinated Pt adsorption structure (b) is more preferable both in terms of stability and CO tolerance.

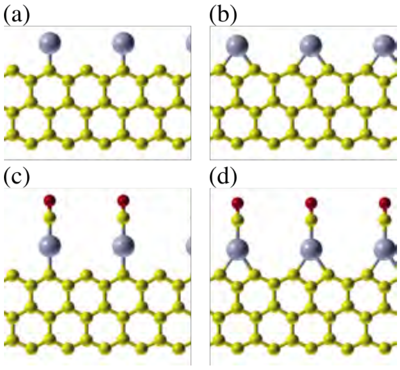

Fig. 1: Pt adsorption on graphene edges (a,b) and CO adsorption on the Pt atoms (c,d).

References

[1] E. Yoo, T. Okata, T. Akita, M. Kohyama, J. Nakamura, and I. Honma, Nano Lett. **9**, 2255 (2009).

[2] Y. Hamamoto et al., for preparation.

Elucidation of high-order harmonic generation from solids by atomistic simulations

Yasushi SHINOHARA

Photon Science Center,

The University of Tokyo, Hongo, Bunkyo-ku, Tokyo 113-8656

High-order harmonic generation (HHG) from crystalline solids has become an active field with intense and ultrashort coherent light sources. HHG in the gas phase is well developed by both theoretical and experimental point of view, leading attosecond resolution via optical science and engineering [1]. In contrast, the solid state HHG is still under intensive discussion, *e.g.* quantitative discussion of intraband current as an extra source of HHG.

We have developed an atomistic simulation framework to describe electronic real-time dynamics of crystalline solids based on time-propagation of one-body density-matrix. We obtain high-order harmonic spectra, taking Fourier transform of the induced current evaluated by the density-matrix. All parameters we need are field-free Hamiltonian and momentum operator because of velocity gauge. Matrix elements for the operator are derived from an *ab-initio* theory, density-functional-theory with local-density-approximation, by using the Elk FP-LAPW code [2].

We perform the simulation for GaSe crystal. Number of active orbital is 103 bands per each Brillouin zone sampling, corresponding to 39 eV energy range. We use 64x64x12 points for the Brillouin zone sampling to see converged results for polarization angle dependence. This simulation reproduces experimental angle dependent HHG spectra for both parallel and perpendicular components [3], at 0.25 eV central frequency, 100 fs pulse duration, and 10 MV/cm field strength imitating experimental condition.

In order to investigate role of intraband current and interband polarization in the HHG, we develop a way to decompose a total current into the two contributions by use of instantaneous eigenfunction of the Hamiltonian based on explicit numerical diagonalization among active bands. This analysis reveals that odd-order harmonics are dominated by the intraband current and even-order harmonics are exclusively contributed by the interband contribution.

References

[1] F. Krausz and M. Ivanov, Rev. Mod. Phys. **81** (2009) 163.

[2] http://elk.sourceforge.net/

[3] K. Kaneshima, Y. Shinohara, K. Takeuchi, N. Ishii, K. Imasaka, T. Kaji, S. Ashihara, K.L. Ishikawa, and J. Itatani, accepted.

First-Principles Molecular Dynamics Study of Biomolecule Synthesis on Primitive Ocean

Kohei Shimamura
Graduate School of System Informatics,
Kobe University, 1-1 Rokkodai, Nada-ku, Kobe 657-8501

We are conducting research on the origin of life using the first-principles molecular dynamics simulation package "QXMD" [1]. The origin of life is thought to have two stages. At the first stage (1), various kinds of reductive molecules were originated on a global scale in the harsh oxidizing environment of the early Earth. Next stage (2), using specific molecules from these various reductive molecules resulted in that primitive life was emerged. The stage (1) is important for preparing a reducing environment where the primitive life appeared easily and the stage (2) is important for providing food groupings for the primitive life. Although there are a lot of hypotheses to mention the stage of (1), we are interested in the possibility of the production of a large amount of organic molecules by the ocean collisions of iron meteorites which the simulation experiments have shown recently. This hypothesis was built on the fact of meteorite collisions at the late heavy bombing period which lasted about 3.8 billion years ago. Since the trace of life of 3.7 billion years ago have already been discovered, the meteorite collision events is considered to be greatly involved in the birth of life. We investigated the reaction processes in which reductive nitrogen and carbon reductive molecules were produced from N_2 and CO_2 as sources by the ocean collision of iron meteorite by means of the first-principles molecular dynamics simulations. Ammonia production was observed as the nitrogen reductive molecule. Interestingly, it was found that a large amount of ammonia produced by meteorite collision as a driving force by three different mechanisms [1]. As carbon reductive molecules, hydrocarbons and carboxylic acids were produced, where bicarbonate produced from CO_2 and H_2O played an important intermediate role in these reaction processes [2].

Such reductive molecules produced were primarily preserved in the early ocean but could not proceed to stage (2) because high concentrations are needed. It was necessary to provide a place where concentration of the reductive molecules could be done. While various kinds of concentrating plants have been considered so far, we are paying attention to the alkaline deep sea hydrothermal vent environment. In this environment some micrometer vesicular iron sulfides can be formed, where reductive organic molecules can be concentrated. Also, since there are abundant reducing agents such as hydrogen, it is a place capable of producing reductive organic molecules using iron sulfides as catalysts. We mimicked this environment and confirmed that carboxylic acid was produced from carbon dioxide on iron sulfide [3]. As a future work, we elucidate the concentration process by making larger simulation system.

References

[1] K. Shimamura, F. Shimojo, A. Nakano, and S. Tanaka: Phys. Chem. Chem. Phys. accepted.

[2] K. Shimamura, F. Shimojo, A. Nakano, and S. Tanaka: submitted.

[3] K. Shimamura, F. Shimojo, A. Nakano, and S. Tanaka: The 55th Annual Meeting of the Biophysical Society of Japan. Poster-number 3Pos163 (2017).

Construction and application of anharmonic potentials for adsorbed molecule on crystal/nanoparticle surface

Wataru Mizukami
Department of Advaced Matrerials Science and Engineering, Fackulty of Engineering Sciences
Kyushu University, 6-1 Kasuga Park, Fukuoka, 816-8580, Japan

Vibrational spectroscopy such as infrared or Raman spectroscopy is a vital tool to probe chemical phenomena at atomic/molecular level. Computational simulations are often used to get a clue to understanding vibrational spectra, where the harmonic approximation is predominantly used owing to its low computational costs. While evaluating vibrational energy levels beyond harmonic approximation is becoming increasingly commonplace for small molecules in gas phase, such methods for a molecule on a surface are not well developed.

This year, we have extended one of our potential-energy-surface (PES) construction methods, which utilizes the LASSO regression technique [1], to consider anharmonic effects on adsorbed molecules. As a test case, we have constructed an analytic PES for H_2O on Pt(111) surface. Thousands of electronic energy data points have been generated randomly for the regression. Those energies have been computed using DFT with the PBE functional. We have employed the VASP program for DFT calculations. An energy extrapolation scheme ONIOM has been used to correct DFT energies. The H_2O monomer has been chosen as a model system for the ONIOM extrapolation. The high-level model system energies (i.e., water-monomer energies) have been evaluated from Partridge–Schwenke potential [2], which is known as the most accurate PES for a single H_2O molecule. The accuracy of PES has been checked by vibrational configuration interactions implemented in the DYNAMOL program [1].

Apart from the PES construction, we have investigated a widely used Pt nanocluster catalyst. Recently, Einaga and his coworkers found that post-processing improves the performance of Pt/TiO_2 catalysis. The experimental analyses suggested that the TiO_2 surface with Pt clusters is prone to be reduced. We have computed the vacancy formation energy on TiO_2-rutile(100) surface with or without an adsorbed Pt cluster in the framework of DFT using the VASP program package. It has been found that interactions between Pt and TiO_2 decrease the vacancy formation energy by 1.4 eV, and the oxygen vacancy shortens the Pt-TiO_2 distance. Our computational result is consistent with the experimental observation using HAADF and STEM-EELS analyses. The stronger interaction between Pt and a reduced TiO_2 surface may explain the change of catalytic activities owing to post-processing.

References

[1] W. Mizukami, S. Habershon, D.P. Tew: J. Chem. Phys. **141** (2014) 144310.

[2] H. Partridge, D.W. Schwenkei: J. Chem. Phys. **106** (1997) 4618.

Calculation of electronic structure of $CH_3NH_3Pb(I,Cl)_3$ mixed crystals

Takayuki Makino

Department of Electric and Electronics Engineering,

University of Fukui, Bunkyo Fukui, Fukui 910-8557

Perovskite type halide compound is known to exhibit several interesting properties. They are , for example, strong excitonic effect and photovoltaic action. Deeper understandings for the corresponding mixed crystals are important from both technological and basic viewpoints [1]. In this research, we intended to calculate electronic structures of $CH_3NH_3Pb(I,Cl)_3$ mixed crystals.

First, we aimed to reproduce the result of previous research [2] conducted on $CH_3NH_3PbI_3$ by obeying the procedure shown in flowchart, corresponding to Fig. 1. We used PWscf package for this kind of calculations. Specifically, we use a set of the optimized norm-conserving Vanderbilt pseudo-potentials generated by Schlipf and Gygi. We confirmed that evaluated band-gap energy can be reproduced in accordance with the values evaluated by Brivio and coworkers [2]. We then moved into study of the electronic structure of $CH_3NH_3PbCl_3$.

Here, we explain about the detailed parameters used for these calculations and show a representative result gotten on a $CH_3NH_3Pb(I,Cl)_3$ mixed crystal. We used SC15 ONCV potential as a Pseudo potential for the structural optimization calculation, starting from the tetragonal symmetry. The used options in PWscf calculation are “vc-relax” and “cell_dofree=xyz”, respectively. We also used a pseudo-potential selected from Pseudo Dojo Potentials for band calculation. Figure 2 shows a band diagram calculated for a mixed crystal including 10% chlorine concentration. In the representation, the energetic origin was shifted so as to the top of the valence band becomes zero. We can notice that an abscissa axis corresponding to the direct optical band-gap is deviated from the Γ point, rather approaching to the R point somehow. We interpret this fact as being due to the change of the crystal structure, approaching to a cubic structure somehow. As one of evidences, relation between the *a*- and *c*-lattice constants becomes closer each other in case of 10% mixed crystal, compared with the purely iodide crystal. We are currently analyzing and summarizing the results because of completion of the calculations for several Cl concentrations.

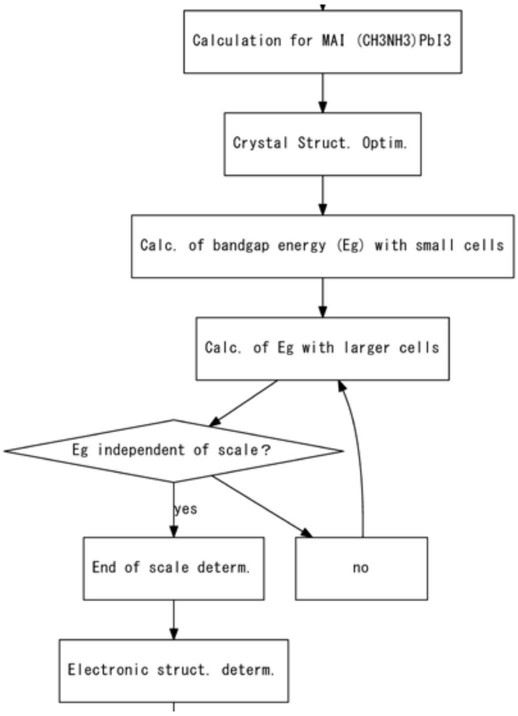

Fig. 1

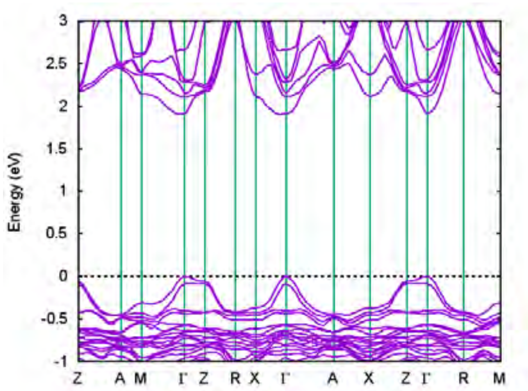

Fig. 2

References

[1] J. H. Heo and S. H. Im: Nanoscale **8** 2554 (2016).

[2] F. Brivio *et al.*, APL Materials **1**, 042111 (2013).

Curious chemical reactions of the entangled singlet state in nanographene VANG

Koichi KUSAKABE
Graduate School of Engineering Science, Osaka University
1-3 Machikaneyama, Toyonaka, Osaka 560-8531

1. The Kondo singlet in nanographene

In a study of tri-hydrogenated atomic vacancies V_{111}, Morishita, *et al.* discovered a series of molecular nanographene structures called VANG.[1] There are degenerated zero modes, *i.e.* the vacancy-centered quasi-localized zero mode and an extended zero mode at the Dirac point. The degeneracy is topologically protected as long as the mirror symmetry of VANG is preserved.[2] Owing to the degeneracy, these alternate hydrocarbon systems possesses the singlet ground state owing to topological nature of π network with $N_A = N_B$. This state is identified as the Kondo singlet.

2. Hydrogen storage application

Hydrogen adsorption on the graphene is affected by detailed conditions of surface morphology.[3] On an atomic vacancy, we have characteristic hydrogenation processes.[4] Among them, the V_{111} structure shows low energy barrier ~ 1.3eV for both adsorption on it and desorption to it. This effect coming from steric hindrance allows us to derive the solution for the hydrogen storage application.[5] On VANG, we have a realistic reaction process composed of migration paths and the $V_{221} \to V_{111}+H_2$ process (Figure 1). This process overcome the difficulty in organic hydrides, making nanographene the unique solution for economically efficient materials for storage.

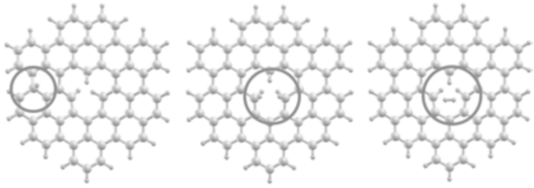

Figure 1: Hydrogen migration paths for a hydrogenated nanographene molecule, VANG, *i.e.* migration from the left panel having stable V_{211} to the middle panel with V_{111} and desorption of H_2 as $V_{221} \to V_{111} + H_2$ (the right).

3. Development of simulation tools

We have established a method to find new classes of edge states at armchair edge,[6] which is applicable for deformed graphene with armchair edges. The electron correlation effects are discussed in several contexts.[7]

Acknowledgement

This work was partly supported by KAKENHI (No. 26107526, 26400357, 16H00914).

References

[1] N. Morishita, *et al.* J. Phys. Soc. Jpn., **85**, 084703 (2016). [2] S. Miyao, *et al.* J. Phys. Soc. Jpn. **86**, 034802 (2017). [3] G.K. Sunnardianto, *et al.* J. Comput. Theor. Nanosci. **13**, 4883 (2016). [4] G.K. Sunnardianto, *et al.* Adv. Sci., Eng. Med., **8**, 421 (2016). [5] G.K. Sunnardianto, *et al.* Int. J. Hydro. Energy **42**, 23691 (2017). [6] M. Ziatdinov, *et al.* Phys. Chem. Chem. Phys. **19**, 5145-5154 (2017). [7] K. Nishiguchi, *et al.* J. Phys. Soc. Jpn. **86**, 084707 (2017) .

References

[1] N. Morishita, G.K. Sunnardianto, S. Miyao, K. Kusakabe, J. Phys. Soc. Jpn., **85**, 084703 (2016).

[2] S. Miyao, N. Morishita, G.K. Sunnardianto, K. Kusakabe, J. Phys. Soc. Jpn. **86**, 034802 (2017).

[3] G.K. Sunnardianto, I. Maruyama, K. Kusakabe, J. Comput. Theor. Nanosci. **13**, 4883 (2016).

[4] G.K. Sunnardianto, I. Maruyama, K. Kusakabe, Advanced Science, Engineering and Medicine, **8**, 421 (2016).

[5] G.K. Sunnardianto, I. Maruyama, K. Kusakabe, Int. J. Hydrogen Energy **42**, 23691 (2017).

[6] M. Ziatdinov, H. Lim, S. Fujii, K. Kusakabe, M. Kiguchi, T. Enoki, and Y. Kim, Phys. Chem. Chem. Phys. **19**, 5145-5154 (2017).

[7] K. Nishiguchi, S. Teranishi, K. Kusakabe, J. Phys. Soc. Jpn. **86**, (2017).

Development and application of time-dependent electron-transport simulator based on first-principles method

Yoshiyuki EGAMI
Division of Applied Physics, Faculty of Engineering, Hokkaido University
Kita 13, Nishi 8, Kita-ku, Sapporo, Hokkaido 060-8628

Recently, computational simulations with a high accuracy and efficiency have attracted much attention in both fields of fundamental science and engineering. For example, in the research on and development of electronic devices, numerical approaches play important roles to understand the relationship between atomic and electronic structures of materials and electric, magnetic and optical characteristics of devices. A large number of notable studies using first-principles calculations have been performed so far to elucidate the relationship and characteristics. However, most of the calculations are based on the density functional theory which describes the static characteristics of electrons in the steady state, and there remains to be discussed a time-dependent behavior of electrons.

In order to demonstrate the time-dependent transport properties of electrons through the nanoscale materials, we developed the impulse response (IR) method [1] based on the real-space finite-difference approach [2] within the framework of the time-dependent density functional theory. In this subject, for the IR method, we have worked on the improvement of the efficiency of parallel computing in the spatial dimensions since we cannot parallelize the calculations in the direction with respect to time due to the sequential evolution of scattering wave functions.

On the other hands, we have calculated the electron transport properties of the impurity-embedded carbon nanotube (CNT)[3] and molecular junction consisting of a transition metal complex molecule[4] using the conventional time-independent electron transport simulator[5, 6] in order to compare the characteristics obtained by the IR method. As the results, we found a high transmission probability near unity for electrons transporting the BN-embedded CNT when the geometrical coordinates of impurities coincident with spacial node positions of wave functions of propagating electrons. Moreover, the circular current flow around Mn atom in a Mn(dmit)$_2$ molecular junction is observed, where the d-orbitals of Mn atom play a key part. These work have been performed on System B.

References

[1] Y. Egami and K. Hirose: JPS Conf. Proc. **1**, 016012 (2014).

[2] K. Hirose *et al.*: *First-Principles Calculations in Real-Space Formalism*, (Imperial College Press, London, 2005).

[3] Y. Egami and H. Akera: Physica E **88** (2017) 212.

[4] Y. Egami and M. Taniguchi: Jpn. J. App. Phys. **57** (2018) 021601.

[5] Y. Egami, K. Hirose and T. Ono: Phys. Rev. E **82**, 56706 (2010).

[6] Y. Egami, S. Iwase, S. Tsukamoto, T. Ono and K. Hirose: Phys. Rev. E **92**, 033301 (2015).

Development of materials of proton-conducting solid electrolyte fuel cells and analysis of ion conduction

Gen Kojo, Junichiro Otomo

Graduate School of Frontier Sciences,

The University of Tokyo, Kashiwa-no-ha, Kashiwa, Chiba 277-8581

1. Introduction

Solid oxide fuel cells (SOFC) are one of the key electrochemical devices as energy and environmental devices. Recently, proton-conducting solid oxide fuel cells (p-SOFC) have attracted attention due to their energy conversion efficiency. Many kinds of materials have been studied for proton conducting solid electrolyte.

In this study, we discussed two proton conducting materials. The former material was lanthanum tungstate (LWO). It has been developed as an electrolyte materials for p-SOFC, and LWO has intrinsic oxygen vacancies in its crystal structure. For this material, we examined the proton diffusion mechanism in LWO by quantum chemical calculations.

The latter material was $La_2Ce_2O_7$ (LCO). LCO shows proton conductivity at intermediate temperatures (T < 600 °C). The proton conduction in $La_2Ce_2O_7$ depends on the amount of oxygen vacancies, which could be formed according to reaction (1):

$$\mathrm{La_2O_3} \rightarrow 2\mathrm{La}'_{\mathrm{Ce}} + 3\mathrm{O}_{\mathrm{O}}^{\mathrm{X}} + \mathrm{V}_{\mathrm{O}}^{\cdot\cdot} \qquad (1)$$

In this study, we tried to investigate the relationship between the crystal structure and the amount of oxygen vacancies using the density functional theory (DFT).

2. Computational methods

The proton diffusion pass was calculated by the NEB method [1] using the revised SIESTA code developed by Ohto et al [2]. The number of atoms was 89, and the number of images was 10.

DFT calculations were carried out for $La_2Ce_2O_7$ with VASP [3] code. The generalized gradient approximation (GGA) proposed by Perdew, Burke, and Ernzerhof (PBE) [4] represents the exchange-correlation energy functional. The valence configurations of the pseudopotentials were 4p5s26d1 for La, s2d1f1 for Ce, and s2p4 for O. The energy cutoff for the plane-wave basis was set at 500 eV. As for the structural models, $\mathrm{Fm\bar{3}}m$ was used. The structural relaxation of the unit cell was conducted using Monkhorst-Pack k-point sets with 4 × 4 × 4 until the total energy difference converged to less than 0.001 eV.

3. Results and discussion

The crystal structures are shown in Fig. 1a and the proto-conducting paths considered in this study are shown in Fig. 1b. To simplify the calculations, we used the oxygen at the O2 site with average O1-O2 and O2-O2 distances. The result of the NEB calculation are shown in Fig. 2; the barrier of proton diffusion in the O1-O1 jump is lower than those in the O2-O2 and O1-O2 jumps. This indicates that protons are likely to be trapped at O2 sites and once they

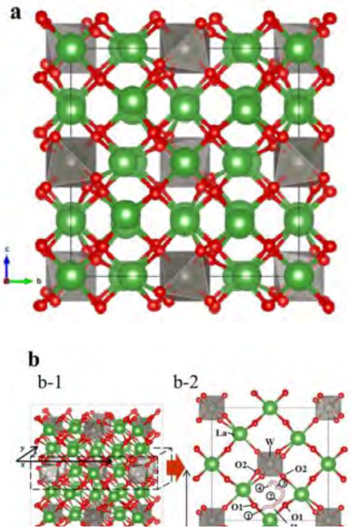

Fig. 1 (a) Optimized crystal structure of LWO and (b) image of proton diffusion paths in LWO calculated using the NEB method.

leave the O2 sites and jump across the high O1-O2 barrier, they diffuse over a long range through cycles of O1-O1 jumps until they are trapped at other O2 sites.

As for the LCO, in order to understanding the results observed in our experiment, the total energies of crystal structures were compared with different positions of oxygen vacancies (see Fig. 2). The calculation result was as follows: (a) -704. 184 eV, (b) -704.190 eV. Under the experimental conditions, i.e. sintering temperature or synthesis method, the samples might have the different position of the oxygen vacancy. Considering the results of this study, the conductivities of the samples synthesized with different methods will have the several conductivities.

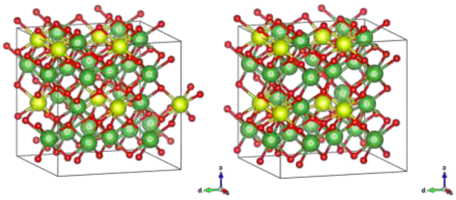

Fig. 2 Schematic images of the structures of La$_2$Ce$_2$O$_7$s.

4. Conclusion

The calculation with NEB method showed that proton diffusion in LWO occurred through an O1-O1 route. The DFT calculation results indicated that the conductivity of LCO was independent of the synthesis method.

References

[1] G. Henkelman *et al.*, *J. Chem. Phys.* **113** (2000) 9901.

[2] T. Ohoto *et al.*, *Phys. Rev. B*. **87** (2013) 1.

[3] G. Kresse *et al.*, *Phys. Reb. B: Condens. Matter. Phys.* **54** (1996) 11169.

[4] Perdew, J. P. *et al.*, *Phys. Rev. Lett.* 77 (1996) 3865.

Organic Molecule on Graphene: Electronic Structure at the Interface and Crystal Growth

Kazume NISHIDATE and Masayuki HASEGAWA

Faculty of Science and Engineering, Iwate University Ueda 4-3-5, Morioka, Iwate 020-8551

Intact graphene with this electronic structure is a zero-gap semiconductor and electronically behaves like a semimetal. Electronic properties of this pristine nanostructure are usually not preserved in graphene under internal or external perturbations such as mechanical strains, deformations, adsorption of foreign atoms or molecules, electric field, contact with substrates, and other interactions with the environment. In the last decade a large-scale epitaxial graphene of high quality has been successfully grown by thermal decomposition of silicon carbide (SiC) surfaces and it is, in fact, recognized and theoretically supported that the Dirac band with linear dispersion is lost in the so called “buffer” graphene layer due to the strong bonding to the SiC surface. On the other hand, a modified Dirac band with a substantial gap at the Dirac point has been observed in the so called “first” graphene layer on SiC and interpreted as a band gap opening due to A-B sublattice symmetry breaking as in the case of graphene on hexagonal boron nitride (h-BN). However, this interpretation has not been supported by any explicit analysis and, therefore, is not fully recognized at present. We also note that recently angle resolved photoemission spectroscopy (ARPES) has demonstrated that the “buffer” graphene layer on SiC is also electronically quasi-freestanding with a band gap larger than 0.5 eV for highly ordered interactions with the substrate, exemplifying that understanding electronic structure of graphene on substrates is still far from complete.

In our DFT calculation, we first use a lattice matched model to demonstrate that a substantial band gap is induced in graphene by sufficiently strong A-B sublattice symmetry breaking[1]. This band gap opening occurs even in the absence of hybridization between graphene π states and Au states, and a strong sublattice asymmetry is established for a small separation (d) between the graphene and Au layer, typically, d $<$ 3.0 Å. In realistic situations, which are mimicked using lattice mismatched models, graphene π states near the Dirac point easily hybridize with nearby (in energy) Au states even for a van der Waals distance, d $\sim$ 3.4 Å, and this hybridization usually dictates a band gap opening in graphene. In that case, the top parts of the intact Dirac cones survive the hybridization and are isolated to form midgap states within the hybridization gap, denying that the band gap is induced by sublattice symmetry breaking. This feature of a band gap opening is similar to that found for the so called “first” graphene layer on silicon carbide (SiC) and the predicted band gap and doping level are in good agreement with the experiments for graphene/Au/Ru(0001).

References

[1] K. Nishidate, S. Tanibayashi, N. Yoshimoto, and M. Hasegawa: Phys. Rev. B **97** (2018) 115437.

First-principles analysis for the iron-based superconductors and the related

Hiroaki IKEDA
Department of Physics, Ritsumeikan University
Kusatsu, Shiga 525-8577

We have investigated unconventional superconductivity in the strongly correlated electron systems. Our aim is to develop the first-principles calculations and reasonably describe the electronic structure of SCES. This year, we studied two topics using a Class B; the application of the quasiparticle GW method (QSGW) to the iron-based superconductors, and a study of gap structure in non-symmorphic superconductors.

First, we performed the QSGW in several typical iron-based superconductors. In the conventional LDA/GGA calculations for the iron-based superconductors, the compensated semi-metallic structure can be roughly described, but the size and curvature of the Fermi surface and the composed orbital characters are significantly deviated from the experimental results. Thus, the electron correlation is important. Here, we applied the QSGW, which improves the band gap of semiconductors. We realized that the obtained band structure (Fig.1) can be improved to explain experimental Fermi surface. This is complementary to the DFT+DMFT studies.

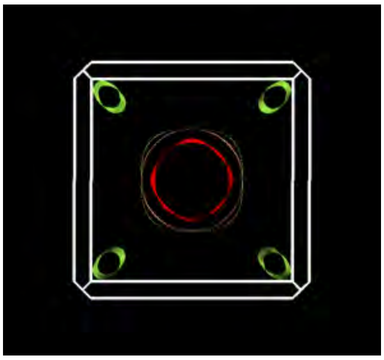

Figure 1: Fermi surface in QSGW for KFe_2As_2.

Second, we performed the group-theoretical classification of gap functions in non-symmorphic structure [1], and investigated recently discovered BiS_2-based layered superconductors. The electronic band structure is mainly composed of the Bi $6p$ orbitals with a relatively large spin-orbit coupling (SOC). The Bi site does not have inversion symmetry. Recent angle-resolved spectroscopies have indicated remarkable gap anisotropy and/or a sign change on a small Fermi pocket around X point. It implies a possibility of unconventional pairing state in this material. Here we have studied the gap structure in an extended Hubbard model with Bi-S inter-site interactions. The band structure was obtained by the first-principles downfolding. We found that the ferroic charge/quadrupole fluctuation driven by the inter-site interaction leads to a fully-gapped $d_{x^2-y^2}$-wave pairing state, in which the gap amplitude has sizable anisotropy on the Fermi surface. This work was published in [2].

References

[1] T. Nomoto, and H. Ikeda: J. Phys. Soc. Jpn. **86** (2017) 023703.

[2] K. Suzuki, H. Usui, K. Kuroki, and H. Ikeda: Phys. Rev. B **96** (2017) 024513.

First-principles Study of Defects of Magnesium Alloys

Daisuke Matsunaka
Department of Mechanical Systems Engineering,
Shinshu University, 4-17-1 Wakasato, Nagano 380-8553

Magnesium (Mg) has been of increasingly interest from the engineering viewpoint, because of its low density and relatively high specific strength. Despite intensive research efforts, there remain various problems to be overcome; low ductility and low toughness at room temperature. In order to investigate deformation behavior of Mg at the atomic level, we have carried out molecular dynamics simulations. Particularly, we have focused on effects of normal stress components on the <a> slip systems; basal, prismatic, and first-pyramidal slips. For the basal slip, partial dislocation s were generated and glided on the slip plane, irrespective of the applied normal stress. On the other hand, for the prismatic and first-pyramidal slips, distinct dislocation gliding was not observed and alternatively deformation twins were generated. In the simulations of the prismatic slip under the high normal stress of 300MPa, double twins were formed additionally.

In Mg alloys with rare earth elements, the addition in solid solution causes a significant increase in ductility. It is an important issue to elucidate effects of an alloying element on each deformation mode such as deformation twinnings and non-basal slips. First-principles calculations give us valuable information of alloying elements. Development of interatomic potentials for alloys which can describe the first-principles results is necessary for atomistic simulations of deformation in Mg alloys. In this study, we have investigated two-body potential forms between species in the embedded atom method (EAM) potentials. Although the invariance to a transform in which a term linear in the electron density is added to or subtracted from the embedding function and an appropriate adjustment is made to the two-body potential is not always hold, the transform was set so that the substitution energy got close to the first-principles values. Using the obtained alloy EAM potentials, the generalized stacking fault energy curves of the basal and prismatic slips were calculated and compared with the first-principles results.

References

[1] S. Yoshikawa and D. Matsunaka: to be submitted.

[2] D. Matsunaka and F. Kimura: Conf. Proc. Jpn. Soc. Comp. Eng. Sci. **23** (2018) B-01-07.

Electronic structure of light rare earth permanent magnets

H. Akai
Institute for Solid State Physics, University of Tokyo
Kashiwa-no-ha, Kashiwa, Chiba 277-8581

Despite intensive efforts to develop permanent magnets whose performances exceed that of the $\mathrm{Nd_2Fe_{14}B}$ magnet, no essentially novel magnet has been developed so far. In this situation, one might question whether it is possible at all to obtain a permanent magnet material that is superior to the currently available maximum performance.

To answer this, one should have a perspective on the possible maximum performance of permanent magnet materials. One of way to do this is to estimate the upper limits of magnetization J_{S}, Curie temperature T_{C}, and lowest order uniaxial magnetic anisotropy constant K_1, which make a prospect about the performance of magnets. We discuss each of these quantities on the basis of the results obtained through first-principles calculation.

The discussions are based on all-electron electronic structure calculations performed within the local density approximation (LDA/GGA) of density functional theory (DFT). Machikaneyama (AkaiKKR) KKR-CPA package [1] was used, and for the calculation of T_{C}, Liechtenstein's method [2] was employed.

Figure 1 shows the calculated magnetization J_{S} of $3d$ elements as a function of the lattice constant a and atomic number Z. The fractional atomic number of a fictitious atom is used. The number of total electrons per atom is equal to Z. The crystal structure is assumed bcc. A prominent feature is that it has a dome-like structure appearing around $a = 2.65$ A and z=26.4, where J_{S} takes the maximum value of 2.66 T. It is pointed out that this is related to the fact that in the bcc structure, the interatomic distance between nearest neighbor pairs becomes small, forming a considerable bonding–antibonding splitting with a pseudo gap in between. Unfortunately, the lattice constant $a = 2.65$ A is 7 % too small compared with the equilibrium lattice constant of bcc Fe. Contrary to the general behavior of the magnetic moment that increases as the volume increases, the magnetic polarization increases with decreasing a up to some point where the magnetic state collapses.

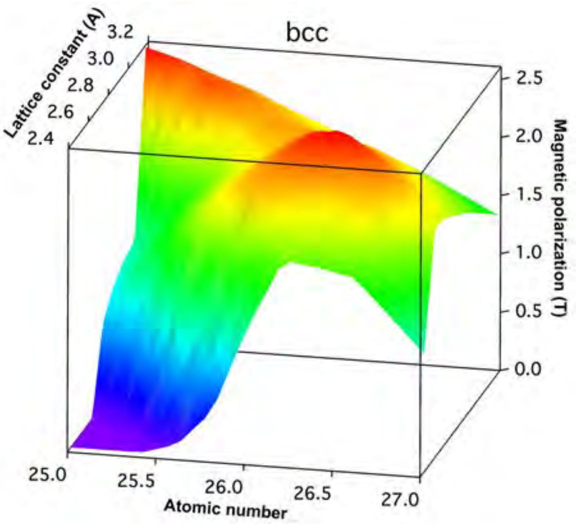

Figure 1: Saturation magnetic polarization J_{S} of the system plotted against the lattice constant and the fictitious atomic number[3].

Magnetic polarization takes on a large value at one of the corner points in the Z-a plane,

$Z = 25$ and $a = 3.2$ A, but this is not real. In this region, the antiferromagnetic state is more stable than the ferromagnetic state. Combining this fact with the information given by Fig. 1, we may conclude that a large J_S is expected only in the vicinity of the dome-like structure, and the upper limit of J_S would not exceed ~ 2.7 T.

Figure 2 shows the behavior of magnetic transition temperature T_C as a function of Z and a. Here, we again see a dome-like structure near $Z = 26.5$ and $a = 2.9$ A. This position approximately coincides with the position of the similar dome-like structure in J_S. This indicates that if $Z = 26.5$ and $a = 2.9$ A is forced by crystal structure, chemical composition, pressure, temperature, etc., $J_S \sim 2.7$ T is achieved. T_C drops rapidly toward the corner in the Z-a plane, $Z = 25$ and $a = 3.2$ A, where T_C becomes negative, meaning that the antiferromagnetic state should be the ground state. Now, we may say that the upper limit of T_C is ~ 2000 K (if fcc structure were assumed, the upper limit would be ~ 1500 K).

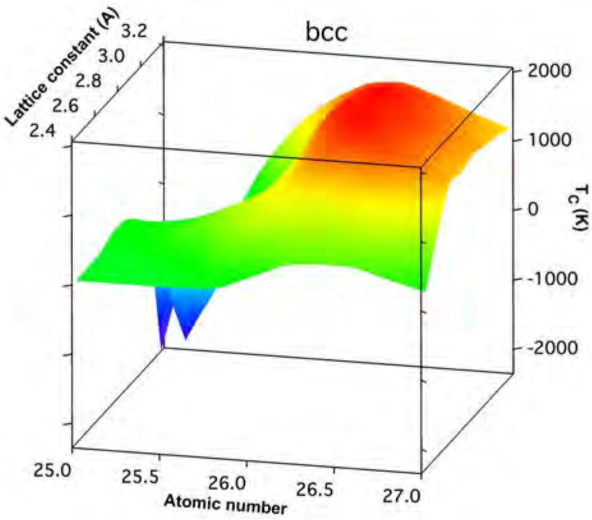

Figure 2: Magnetic transition temperature T_C of the system plotted against the lattice constant and the fictitious atomic number[3].

The main origin of magnetocrystalline anisotropy is spin orbit coupling. For Sm (Sm^{3+} in Sm-type Sm element), assuming that the orbitals are firmly bound to the lattice, the upper limit of the magnetic anisotropy constant K_1 estimated from the strength of the spin-orbit coupling , together with the values of $\langle L \rangle$, is as high as ~ 1000 MJm^{-3}. The upper limit of K_1 for other lanthanides, if scaled by the value of L, also would be similar to that of Sm. However, K_1 of rare earth magnetic materials is one to three orders of magnitude smaller than this values. This is because the anisotropy in lattice geometry is not large enough to firmly bind the orbital to the lattice: the $4f$ electron density rotates in line with magnetization to some extent. Therefore, the upper limit of K_1 is bound by the lattice geometry. Also, the magnetic moment carried by $3d$ orbitals of transition metal ions is only weakly coupled to the $4f$ orbitals of rare earth ions (through $3d$–$5d$ indirect and $5d$–$4f$ direct exchange coupling), the latter producing a large magnetic anisotropy. Accordingly, the magnetization is rather loosely bound to the lattice. The effect is in particular prominent at high temperature $T \gtrsim (2/3)T_C$, where the coupling between $3d$ and $4f$ becomes progressively weaker because of the thermal fluctuation.

In conclusion, calculations based on density functional theory conclude that the plausible upper limits of saturation magnetic polarization, magnetic transition temperature, and the magnetocrystalline anisotropy constant of permanent magnet materials could be ~2.7 T, ~2000 K, and ~1000 MJm^{-3}.

References

[1] H. Akai, AkaiKKR, `http://kkr.issp.u-tokyo.ac.jp/` (2002).

[2] A. I. Liechtenstein, M. Katsnelson, V. Antropov, V. Gubanov, J. Magn. Magn. Mater. 67 (1987) 65.

[3] H. Akai: Scripta Materialia (2018), in press.

Ab initio design of an optimal anisotropic ferromagnet

M. Matsumoto (Akai group)
Institute for Solid State Physics, University of Tokyo
Kashiwa-no-ha, Kashiwa, Chiba 277-8581

Introduction Rare-earth permanent magnets (REPM) have been and will be one of the most important materials for industrial applications in these several decades. In REPM a three-dimensional Ising ferromagnet is realized with the magnetization mostly coming from Fe-group elements and uni-axial anisotropy from rare-earth elements. Metastable states in the magnetization curve at finite temperature is exploited as a seemingly permanent magnetization as measured in a human-scale observation time. The theoretical challenge posed by one of the most common utility of REPM is to find a way to optimize the magnetization and the uni-axial magnetic anisotropy energy, in the temperature range between 230K and 450K. The $4f$-electrons are only loosely coupled to the $3d$-electron magnetization via an indirect exchange coupling mediated by $5d$-electrons of which scale is $O(1)$ meV. This weak coupling is on a par with the room-temperature scale as combined with the coordination number between rare-earth and Fe-group atoms. Thus $4f$-electron contribution to the bulk magnetism gets rapidly blurred out as the magnet is heated in the operation temperature range. The intrinsic solution to sustain the ferromagnetism with uni-axial anisotropy is to enhance $4f$-$3d$ coupling [1] possibly via $5d$-electron engineering and enhancing $3d$-electron magnetism which is mostly in charge of the operation-temperature magnetism. Pursuing the latter line of attack, we revisit the Slater-Pauling curve of Fe-Co alloys along which the magnetization M is maximized. Target quantities to be maximized as a function of Fe-Co mixing ratio are extended to Curie temperature T_{Curie}, uni-axial magnetic anisotropy energy K, together with the formation energy to ensure that the desired magnetic properties in the focus temperature range is realized with a bulk-stable material. We take $\mathrm{RCo_5}$ (R=rare earth) as a prototypical materials family and set R=Y.

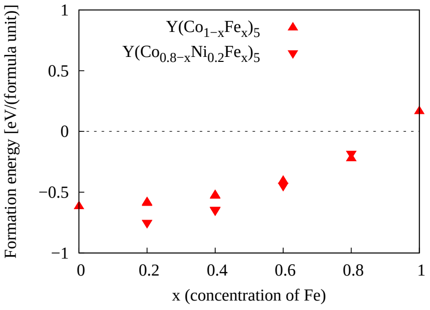

Figure 1: Calculated formation energy of $\mathrm{Y(Co,Fe)_5}$ and $\mathrm{Y(Ni,Co,Fe)_5}$ as a function of Fe concentration.

We calculate magnetization, magnetic anisotropy energy, and Curie temperature of $\mathrm{Y(Co,Fe)_5}$. All of them are summarized as a function of Fe concentration and the optimal chemical composition to extract the best performance in terms of intrinsic magnetism is inspected. On a basis of atom-by-atom substitution the lattice constants are calculated by a structure optimization scheme with OpenMX [3]. These results are given discretely for $\mathrm{YCo}_{5-n}\mathrm{Fe}_n$ with $n = 0, 1, 2, 3, 4,$ and 5. Continuous interpolation on the Fe concentration is done on the basis of coherent potential approximation as implemented in

AkaiKKR [2]. Resultant formation energy of Y(Co,Fe)$_5$ is shown in Fig. 1. These runs set up a working lattice for calculating M, K, and T_{Curie}.

Results Having in mind utility as a permanent magnet compound, calculated results for $\mathrm{Y(Co}_{1-x}\mathrm{Fe}_x)_5$ are summarized on a plane spanned by magnetization M and uni-axial magnetic anisotropy energy K. Materials that reside the upper and the right-hand side of M-K plane pop up as the promising candidates. Discrete results obtained with OpenMX at $T = 0$ shown in Fig. 2 combined with continuous results obtained with AkaiKKR for $M(x, T = 0)$ and $T_{\mathrm{Curie}}(x)$ shown in Fig. 3 indicate that Co concentration of around 20% would give an optimal performance in the observed trade-off between $K(x)$ and $M(x)$, also between K and T_{Curie}.

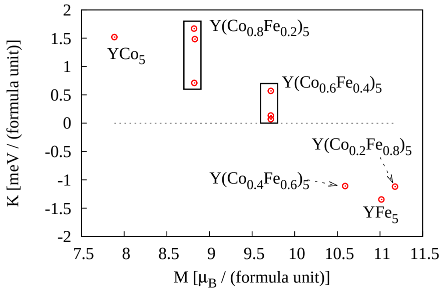

Figure 2: Calculated magnetization and magnetic anisotropy energy of Y(Co,Fe)$_5$ at $T = 0$.

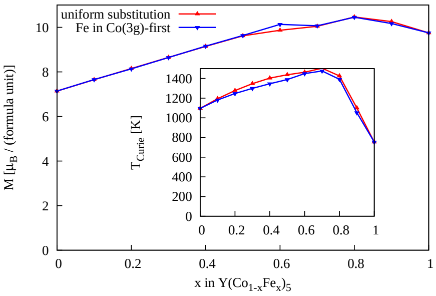

Figure 3: Calculated Curie temperature of Y(Co,Fe)$_5$.

Since Fe-rich side faces the significant instability as seen in Fig. 1 trade-off is going on also between (M, T_{Curie}) and formation energy where a peak for the former is found on the Fe-rich side while Fe-rich side is excluded from the loss of utility in the latter. Recently it has been discussed [4] that addition of Ni can stabilize Fe-rich composition for Sm(Ni,Co,Fe)$_5$ compounds. We have collected similar data for Y(Ni,Co,Fe)$_5$ as was plotted in parallel in in Fig. 1. Our Y-based materials with the common crystal structure share the trends in the range of Fe concentration from 20% to 60% with the observed trend that Ni helps the stabilization of 1:5 structure at a fixed concentration. Meanwhile the stability range of Fe concentration might not be quite enhanced for our particular case of Y-based compounds. The overall trends depend on the species of rare earth. A study over the comprehensive trends spanning a wider range of rare earth elements is reported elsewhere.

Conclusions Prerequisites for a good permanent magnet compound, namely, magnetization, uni-axial magnetic anisotropy energy, Curie temperature, and formation energy has been investigated *ab initio* as a function of Fe-Co mixing ratio for Y(Co,Fe)$_5$. The overall trend concerning 3d-electron part has been clarified and an optimal concentration range of a small amount of Fe in the middle of trade-off between the anisotropy and the rest has been identified.

References

[1] MM, H. Akai, Y. Harashima, S. Doi, and T. Miyake, J. Appl. Phys. **119**, 213901 (2016).

[2] http://kkr.issp.u-tokyo.ac.jp/jp/

[3] http://www.openmx-square.org

[4] P. Söderlind, A. Landa *et al.*, Phys. Rev. B **96**, 100404(R) (2017)

Geometric and electronic structures of two-dimensional atomic-layered materials

Noriaki TAKAGI[1], Ryuichi ARAFUNE[2], and Emi MINAMITANI[3]
[1]*Department of Advanced Materials Science, University of Tokyo*
Kashiwa-no-ha, Kashiwa, Chiba 277-8561,
[2]*International Center for Materials Nanoarchitectonics, National Institute for Materials, Science, 1-1 Namiki, Ibaraki 304-0044,*
[3]*Department of Materials Engineering, The University of Tokyo, 7-3-1 Hongo, Bunkyo-ku, Tokyo 113-8656, Japan.*

The discovery of graphene has fueled the competition to explore exotic two-dimensional (2D) materials. One-atom thick honeycomb sheets consisting of heavy atoms such as Si, Ge, Bi, etc., are attracting because these are strong candidates of 2D topological insulator. Semimetallic $MoTe_2$ and WTe_2, members of transition metal dichalcogenides, are theoretically categorized into type-II Weyl semimetal.

Recently, we have investigated the geometric and electronic structures of Bi thin films grown Au(111), $MoTe_2$ and WTe_2 mainly by using scanning tunneling microscopy (STM).

We carried out density functional theory (DFT) calculations to elucidate the structure for Bi monolayer on Au(111) and quasi-particle interference (QPI) occurring at the surfaces of $MoTe_2$ and WTe_2. The DFT calculations were carried out by the plane-wave-based Vienna Ab initio Simulation Package (VASP) [1, 2] with the projected augmented wave method [3].

For the structure of Bi monolayer, a structure model was optimized and the calculated STM image was compared with that observed by STM. Both images were reasonably agreed with each other. The results were presented in [4]

For QPIs of $MoTe_2$ and WTe_2, bulk band structures were calculated and the iso-energy cuts of the band structure were calculated. The several structures appearing in the QPIs were reasonably reproduced. Some of the structures were not explained by the bulk band structure and we assigned these structures to be Fermi arc surface states inherent to Weyl semimetal. The results are nicely agreed with the theoretical calculations presented previously [5]. The results were published in [6,7].

Reference

[1] G. Kresse and J. Furthmüller: Phys. Rev. B **56**, 11169 (1996).
[2] G. Kresse and J. Furthmüller: Comput.

Mater. Sci. **6**, 15 (1996).
[3] P. E. Blöchl: Phys. Rev. B **24**, 17953 (1994) 17953.
[4] N. Kawakami *et al.*:Phys. Rev. B **96**, 205402 (2017).
[5] A. A. Soluyanov *et al.*: Nature **527,** 495 (2015).
[6] C. -L. Lin *et al.*: J. Phys. Condensed Matters 30, 105703 (2018).
[7] C.-L. Lin *et al.*: ACS Nano **11**, 11459 (2017).

Geometric and electronic structures of magnetic molecules at surfaces

Noriaki TAKAGI[1], Ryuichi ARAFUNE[2], and Emi MINAMITANI[3]
[1]*Department of Advanced Materials Science, University of Tokyo*
Kashiwa-no-ha, Kashiwa, Chiba 277-8561,
[2]*International Center for Materials Nanoarchitectonics, National Institute for Materials, Science, 1-1 Namiki, Ibaraki 304-0044,*
[3]*Department of Materials Engineering, The University of Tokyo, 7-3-1 Hongo, Bunkyo-ku, Tokyo 113-8656, Japan.*

Adsorption of metal phthalocyanines (MPcs) on solid surfaces has gathered considerable attention because these molecules exhibit unique properties [1-3]. MnPc, FePc and CoPc are typical members of MPc family and the adsorption of these molecules on solid surfaces has been intensively studied. Recently, we have investigated the magnetism of FePc on noble metal surfaces, especially the relation between the spin state and the molecule-surface (Mol-S) interaction, by using scanning tunneling microscopy (STM) and spectroscopy (STS) and photoelectron spectroscopies. We have elucidated that the S=1 spin state of the bulk FePc is converted when the molecule directly contacts Cu(110) [4]. In contrast, the S=1 state is preserved by inserting atom-thick oxide layer between the molecule and the Cu substrate [4]. On Au(111), two unpaired spins of S=1 FePc exhibit Kondo effect because of the exchange coupling with the substrate electrons [5,6,7]. These examples indicate the spin state is sensitive to the molecule-surface interactions.

Using the plane-wave-based Vienna Ab initio Simulation Package (VASP) [8,9] with the projected augmented wave method [10], we performed the DFT calculations for MnPc molecules on In atomic layers grown on Si(111). The substrate was described as a slab model and the molecular adsorption structures were calculated as functions of molecular configuration and adsorption site. The results were compared with those acquired by STM. We found the DFT results reasonably explain the adsorption structures of MnPc on In layers grown on Si(111).

Reference

[1] R. Bonnett: Chem. Soc. Rev. **24**, 19 (1995).
[2] C. C. Lanznoff and A. B. P. Lever: *Phthalocyanines, Properties and Applications* (Wiley, New York, 1996).

[3] K. Kadish, and R. Guillard: *Applications of Phthalocyanines, The Porphyrin Handbook* (Academic Press, San Diego, 2003).

[4] N. Tsukahara *et al.*: Phys. Rev. Lett. **102**, 167203 (2009).

[5] N. Tsukahara *et al.*: Phys. Rev. Lett. **106,** 187401 (2011).

[6] E. Minamitani *et al.*: Phys. Rev. Lett. **109**, 086602 (2012).

[7] R. Hiraoka et al.: Nat. Commun. **8**, 16012 (2017).

[8] G. Kresse and J. Furthmüller: Phys. Rev. B **56**, 11169 (1996).

[9] G. Kresse and J. Furthmüller: Comput. Mater. Sci. **6**, 15 (1996) 15.

[10] P. E. Blöchl: Phys. Rev. B **24**, 17953 (1994).

Reaction processes of polyalcohols in high temperature water by First Principles Calculations

Chang Yong Lik[1], Takehiko Sasaki[1], Motoyuki Shiga[2]

1 Department of Complexity Science and Engineering, Graduate School of Frontier Sciences,
The University of Tokyo, Kashiwa-no-ha, Kashiwa, Chiba 277-8561
2 Center for Computational Science and E-Systems, Japan Atomic Energy Agency
148-4 Kashiwanoha Campus, 178-4 Wakashiba, Kashiwa, Chiba, 277-0871

1 Introduction

Conventional chemical reactions taking place in organic solvents would cause negative effects on the environment. In recent years, the need to find eco-friendlier means of producing chemical products has driven a surge of interest to carry out chemical reactions in high-temperature water (HTW) as a reaction medium in green chemistry. To fully comprehend the reaction mechanisms behind this, it is necessary to carry out extensive studies in simulations with first-principles calculations. In this study, the dehydration reaction of 1,2,5-pentanetriol (PTO) to tetrahydrofurfuryl alcohol (THFA) and 3-hydroxytetrahydropyran (3-HTHP) is conducted with Metadynamics of first-principles calculations in HTW at 573 K and 20 MPa. The free energy surface (FES) analysis is carried out to study the reaction mechanism behind the dehydration process, and compare it with the previous experimental study [1].

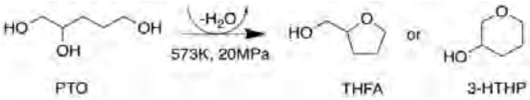

Fig. 1: The dehydration of PTO.

The dehydration reaction pathways of PTO are labeled as 5PTO2, 5PTO5, 6PTO1 and 6PTO5 as shown in Figure 2.

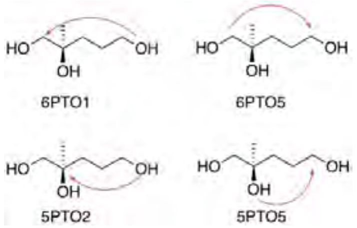

Fig. 2: The dehydration reaction pathways of PTO.

2 Method

By using PIMD[2]/DFTB3[3] (Metadynamics software) developed by Shiga Motoyuki of Japan Atomic Energy Agency, we analyzed the FES by Metadynamics and observed the dehydration reaction by Molecular Dynamics; to obtain the energy barrier of the transition state from the free energy analysis and estimate the number of calculation steps and required time for the reaction to happen. Furthermore, the same calculation is performed with PIMD/VASP [4] to obtain the energy barrier more accurately.

In Metadynamics, the FES of the system is sampled based on the reaction coordinates

(Collective Variables: CV) of the system, then a positive Gaussian function potential is added to the actual FES to bias the reaction. The definition of CV is shown in Figure 3.

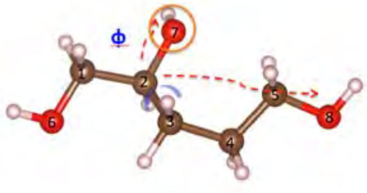

Fig. 3: The definition of CV [5PTO2] : Dihedral angle Φ (C2-07&C3-C4), the difference in bond length r ($d=r_{28}-r_{27}$,) coordination number n_2 (the number of hydrogen attached to O7).

3 RESULTS

The free energy of (R)-PTO was calculated with Metadynamics by adding a Gaussian function potential of height=100 K, width={Φ = 12.0 °, r = 0.20, n = 0.066}. 6PTO1, 6PTO5 via S_N2 yielded 3-HTHP, while 5PTO2, 5PTO5 via S_N2 yielded THFA. The free energy of each reaction pathway is summarized in Table 1.

Table 1: Free Energy of each reaction pathway.

Product	Reaction Pathway	Free Energy[kcal/mol]		
		1	2	Average
THFA	5PTO2	33.86	32.67	33.27
	5PTO5	32.29	27.30	29.80
3-HTHP	6PTO1	33.02	34.76	33.89
	6PTO5	38.71	37.01+	37.86+

In the previous study,[1] the free energy of THFA and 3-HTHP in acidic condition at 573K under 20MPa; were 41.70 kcal/mol and 43.92kcal/mol respectively. In this calculation, it was found that the activation energy for THFA was smaller by 4.09kcal/mol than that for 3-HTHP, in agreement with the experimental results. Furthermore, the S_N2 reaction occurs when the oxygen atom attached to the attacking carbon atom is protonated, indicating that the acidic condition and the presence of protons play an important role in this reaction. However, the calculated free energy is much smaller than the experimental value. The error seems to be caused by the roughness on the FES when the sampling is stochastically performed.

4 CONCLUSION

The free energy of (R)-PTO was calculated with Metadynamics and the qualitative agreement with the experimental results was obtained. To minimize the error and free energy fluctuation, it is necessary to perform this calculation four times, and to sample the FES in the vicinity of the transition state with a smaller CV. In addition, we increase the calculation accuracy of free energy by the Well-Tempered Metadynamics [5].

References

[1]A. Yamaguchi, N. Hiyoshi, O. Sato, K.K. Bando, M. Shirai, Green Chem., 2009, 11, 48-52.

[2]PIMD.https://ccse.jaea.go.jp/ja/download/pimd/index.jp.html.

[3]Density Functional Theory based Tight Binding. https://www.dkb.org.

[4]VASP. https://www.vasp.at/.

[5]A. Barducci, G. Bussi, M. Parrinello, PRL 100, 2008, 020603.

Theoritical analysis of vibronic mode and spin ordering of thin film of transition metallated porphyrin-derivative

Ken-ichi SHUDO
Yokohama Nat'l Univ.
Tokiwadai 79-5, Hodogaya-ku Yokohama 240-8501

Porphyrin-derivatives with transition metal cores are of great interest from view points of the spin theory and the magnetism application. We build a metal-organic framework (MOF) structure of a monolayer molecular films of tetrakis(4-carboxyphenyl)porphyrin (TCPP) with the carboxyl groups bridged by copper ions [1]. This MOF structure has regular arrangement of the electronic spins interacting each other in the planar membrane. So-realized spin lattice is a good prototype among two-dimensional Ising systems.

To investigate the magnetism, we observed experimentally the magnetic circular dichroism (MCD) in optical absorption of Fe-cored MOF of TCPP in near-IR to UV region, which showed strong signal due to the spin–angular-momentum coupling. It has temperature-dependence, as suggests the films has ferromagnetism [?]. At the same time, in this ISSP project, the theoretical calculation of spin-dependent density of state (DOS) of the Fe-cored TCPP-MOF was performed using VASP code [3], suggesting that the MOF exhibits ferromagnetic component near Fermi level. The charge density projected onto the Fe atom resolved the spin polarization (shown in Fig. 1) originating from the Fe core. Several states derived from the Fe orbitals are also found spreading over the molecules at the energy in the molecular HOMO/LUMO gap in the isolated TCPP molecules. Thus, the ferromagnetism newly emerges in the spin lattice in MOF structure.

Author acknowledge Mr. T. Sumiya and Dr. H. Raebiger (YNU), and Dr. A. Muranaka and Prof. M. Uchiyama (Riken) for their contribution.

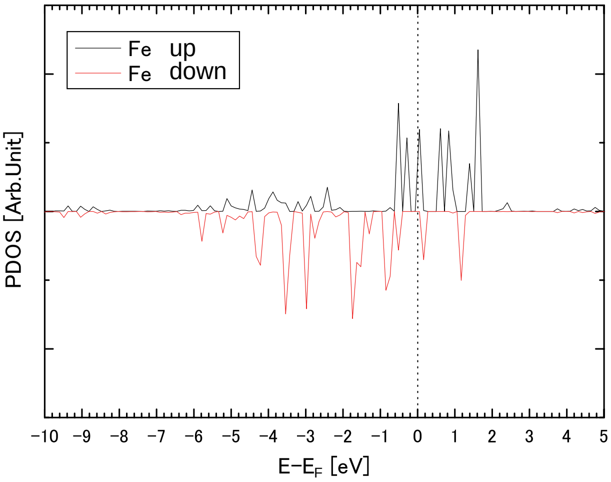

Figure 1: Spin polarization of the partial DOS projected onto the Fe atom in MOF of Fe-cored TCPP.

References

[1] R. Makiura, S. Motoyama, Y. Umemura, H. Yamanaka, O. Sakata and H. Kitagawa: Nature Mat. **9** (2010) 565–571.

[2] M. Gouterman: Optical Spectra and Electronic Structure of Porphyrins and Related Rings, in *The Porphyrins, Vol. III : Physical Chemistry part A* ed. by D. Dolphin, Academic Press (1978, ISBN: 978-0-12-220103-5)

[3] http://www.vasp.at

Study of interaction between radiation damage and interstitial atom

Kazuhito Ohsawa

Institute for Applied Mechanics,

Kyushu University, Kasuga-koen, Kasuga, Fukuoka 816-8580

Hydrogen (H) isotope trapping in tungsten (W) and its alloys are paid attention in the field of fusion reactor because W is one of the important plasma facing materials. Stable configurations of H atoms in mono-vacancy in a bulk W have been reported in the previous work. So, in the present work, we will show stable configurations of H atoms in di-vacancy. Formation energies of di-vacancy and binding energies of H atoms to the di-vacancy are calculated by first-principle calculations based on density functional theory.

Figure 1 shows four H atoms trapped in di-vacancy in a bulk W, as an example. Stable structure of W di-vacancy is two mono-vacancy arranging in <111> direction. There are 12 octahedral interstitial sites (O-sites) in the di-vacancy. Six O-sites are located in the junction of the two mono-vacancies. The H atoms are located close to O-sites and H atoms prefer to O-sites in the junction, as shown in Fig. 1. Binding energies of H atoms to mono- and di- vacancy are shown in Fig.2. Binding energies of H atoms to di-vacancy are much larger than those to mono-vacancy.

According to Fig. 2, H atoms enhances di-vacancy formation. In the fusion reactors, H isotopes are supplied to plasma facing materials. So, the presence of H isotopes is supposed to affect on the growth of vacancy type defects in W of plasma facing materials.

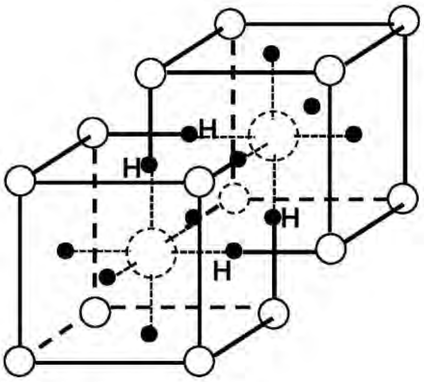

Fig. 1: Stable configuration of four H atoms in W di-vacancy. Black close circles are O-sites.

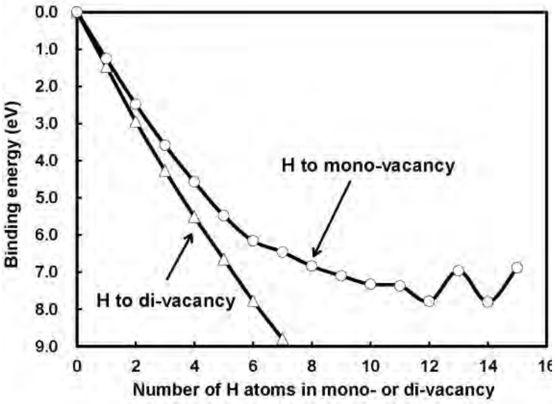

Fig. 2: Binding energy of H to mono- and di-vacancy in W lattice.

Study on physical properties of structural elementary excitations of semiconductor surfaces and interfaces

Hiroyuki KAGESHIMA
Interdisciplinary Graduate School of Science and Engineering, Shimane University
1060 Nishi-Kawatsucho, Matsue, Shimane 690-8504

Our project has been focused on the physical properties of structural elementary excitations of semiconductor surface and interfaces. We have performed two topics in this year. One is the supporting effect on physical properties of vacancies of monlayer $\mathrm{MoS_2}$ [1, 2]. The other is the dynamical properties of $\mathrm{SiO_2}$ at the interface with Si [3, 4]. The calculations were performed based on the first-principles calculation. Program package VASP was employed.

In the first topic, we focus on the properties of vacancies of monolayer $\mathrm{MoS_2}$. Our previous studies revealed that the formation energies of vacancies such as $\mathrm{V_S}$, $\mathrm{V_{S2}}$, and $\mathrm{V_{Mo}}$ are very small in case of negatively charged. We put the monolayer $\mathrm{MoS_2}$ on another monolayer $\mathrm{MoS_2}$, and examine the change of vacancy stabilities. The calculated results indicate that the formation energies increase by more than 0.2 eV. Further, when we put on monolayer $\mathrm{MoSe_2}$, the formation energies increase by more than 0.5 eV. We can understand this stabilization by the vacancy stability on surfaces. Because monolayer $\mathrm{MoS_2}$ is two-dimensional material and has exactly two bare surfaces, vacancies can be easily formed. However, one of the monolayer surface is covered by some other material, it is not a surface any more. Now $\mathrm{MoS_2}$ has only one bare surface. Therefore, the atoms in $\mathrm{MoS_2}$ interact with more atoms before, and vacancies are stabilized.

In the second topic, we focus on the oxygen vacancy effect. During oxidizing Si, we previously found that excess Si is emitted from the interface into the oxide. The excess Si in the oxide causes oxygen vacancies in the oxide. We study the effect of such oxygen vacancy on the diffusivity of Si and O in the oxide based on the first-principles molecular dynamics. We perform the study in the temperature range from 3000 K to 6000 K, and find that the incorporation of oxygen vacancy surely enhances the diffusion of Si and O. We analyze the calculated results, and successfully obtain the equation for the enhanced diffusion. When we compare the obtained equation with the empirical equation experimentally obtained previously, we find good consistencies in their activation energies, prefactors, and enhancement coefficients.

References

[1] S. Urasaki and H. Kageshima, 29th International Conference on Defects of Semiconductors (ICDS2017), Matsue, Japan, ThA1-1.

[2] H. Kageshima and S. Urasaki, International Conference on Solid States Devices and Materials, Sendai (SSDM2017), Japan, PS-13-10.

[3] Y. Yajima and H. Kageshima, International Workshop on Dielectric Thin Films (IWDTF2017), Nara, Japan, P-21.

[4] Y. Yajima, K. Shiraishi, T. Endoh, and H. Kageshima, Jpn. J. Appl. Phys. **57**, 06KD01 (2018).

Search and realization of novel electronic properties of solid surfaces and interfaces and of small particles

Takeshi INAOKA
Department of Physics and Earth Sciences, Faculty of Science,
University of the Ryukyus, 1 Senbaru, Nishihara, Okinawa 903-0213

We describe two of those subjects which we addressed this year.

In view of application to high-speed electronic devices, we examined the subband structure of InSb quantum wires with gates on both sides. We employed those computer programs which we developed ourselves and which incorporate the nonparabolic conduction-band dispersion in the local density approximation. It is quite important to realize how we can control the subband structure effectively by side gates.

Graphene is a very popular single-layer structure of carbon (C) atoms arranged in a hexagonal lattice. This layered material has been examined widely and intensively. It is expected to have extremely high electron mobility. However, we consider that there might be another monolayer structure of C atoms. Using the program package 'Vienna Ab initio Simulation Package' (VASP) [1,2], we explored the possibility of another monolayer structure of C atoms.

(1) Control of the subband structure of InSb quantum wires by side gates [3]

Narrow gap semiconductor InSb has a remarkably nonparabolic conduction-band dispersion, and it is a promising candidate material for high-mobility devices because of its extremely small band-edge effective mass. We can fabricate a quantum wire (QW), namely a two-dimensional (2D) electron system confined in a strip region, by digging trenches in a AlInSb wafer which has a InSb layer as a 2D quantum well. Figure 1 shows the configuration of the QW, side gates and a doping layer which extend infinitely in the z direction. The doping layer above the QW provides electrons to the QW, and the electrons can be controlled by the gates on both sides of the WQ. We assumed the charge neutrality of the QW, the side gates, and the doping layer as a whole. Incorporating the nonparabolic conduction-band dispersion as such in the local-density approximation, we investigated the subband structure to control it effectively by the side gates.

Nonparabalicity of the bulk conduction band reveals itself in subband dispersions as well. When vacuum space extends on both sides of the slab substrate, the electric field produced by the side gates are reduced significantly in the slab substrate, because the electric field is screened conspicuously by polarization of the dielectric substrate with a large static dielectric constant ε_s=17.88. However, when we fill both sides of the slab substrate with dielectric medium, the lateral electric field from the side gates starts to operate effectively on the subbands, especially on the 1st subband, and simultaneously the electron density of the QW, and consequently the number of occupied subbands increases. As for real systems, we should also note that the depth of each trench is finite and that dielectric medium lies below the bottom of the trench.

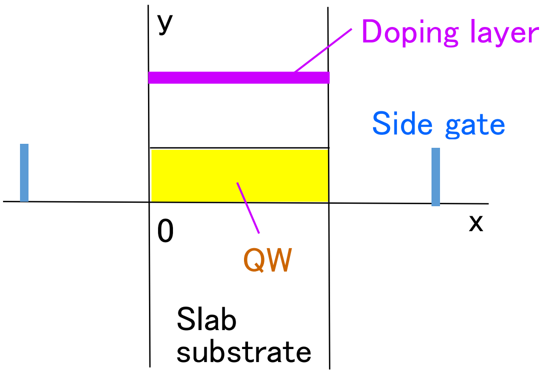

Fig. 1 Configuration of the quantum wire, the side gates, and the doping layer

(2) Proposal of a new single-layer structure of carbon atoms [4]

Graphene has carbon (C) atoms arranged in a hexagonal lattice. Its band structure is characterized by the so-called Dirac cones, and its conduction band and its valence band touches at the Dirac points in the Brillouin zone. Is it the only monolayer structure of C atoms? As another possible structure, we considered the monolayer structure in Fig. 2 which is composed of tetragonal and octagonal patterns. Hückel's rule asserts that cyclobutadiene molecule with its C atoms at four corners of a regular tetragon and cyclooctatetraene molecule with its C atoms at eight corners of a regular octagon are unstable because of generation of an unpaired electron. However, combination of tetragonal and octagonal patterns as in Fig. 2 results in a stable electronic structure. By means of the hybrid density functional method and the generalized gradient approximation in a comparative manner, we optimized the lattice in Fig. 2, and identified the ground state of the electron system. The eighth and ninth bands, each of which is spin-degenerate, cross the Fermi level. It was found that the electron system is a semi-metal which is characterized by the electron pocket around the $\bar{\mathrm{M}}$ point and the hole pocket around the $\bar{\Gamma}$ point. The areal density of the electrons or the holes is more than $2\mathrm{x}10^{14}$ cm^{-2}. The electron system is stable to atom displacement normal to the plane with C atoms on it.

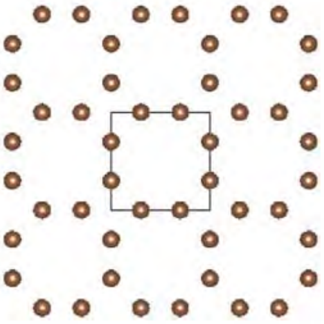

Fig. 2 Proposed monolayer structure of C atoms

References

[1] G. Kresse and J. Hafner: Phys. Rev. B **47** (1993) 558-561.

[2] G. Kresse and J. Furthmüller: Comput. Mat. Sci. **6** (1996) 15-50.

[3] T. Inaoka: to be prepared.

[4] T. Inaoka: in preparation.

First-principles simulation of magnetism and formation of amorphous grain boundary phase of Nd-based permanent magnets

Asako TERASAWA
Department of Materials Science and Engineering, Tokyo Institute of Technology
J1-3, Nagatsuta-cho 4259, Midori-ku, Yokohama 226-8502, Japan

Improvement of Nd-Fe-B magnets without heavy rare earth elements is one of the topics of increasing importance in the applied physics and materials science. The key for high-coercivity Nd-Fe-B magnets lies in the Nd-rich grain boundary (GB) phases [1]. However, the details of structural and magnetic properties of those GB phases are not clarified yet. Some experiments revealed the relationship between the crystallinity of GB phases and the relative angles between the interfaces and the c-plane of neighboring grains [2], which indicates the complexity of the physics in grain boundary phases in Nd-Fe-B magnets. Considering these backgrounds, we targeted the amorphous grain boundary phase for a computational study of magnetism in Nd-based permanent magnets. To simulate the grain boundary phase, we created a model of amorphous Nd-Fe alloy containing 54 atoms computationally on the basis of density functional theory (DFT). For the DFT calculations, we adopte OpenMX [3] code. To create amorphous structures, we performed melt-quench molecular dynamics simulations [4] which contain 0.6 ps of melting, 0.6 ps of quenching, and 0.6 ps of stabilizing procedures at 300K. An example of created amorphous structure is shown in Fig. 1.

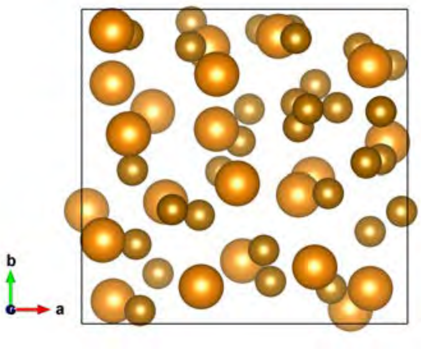

Figure 1: An example of calculated amorphous Nd-Fe alloy, which contains 22 atoms of Nd and 32 atoms of Fe. In the figure, the larger spheres correspond to the Nd atoms and the smaller spheres correspond to the Fe atoms.

Even though we could create amorphous structures from melt-quench MD simulations, we had three problems that makes it difficult to calculate those magnetism. First, the anti-ferromagnetic spin configuration in amorphous structure is not self-evident. This make it difficult to discuss the magnetism of amorphous systems by the energetics. Moreover, spin-dependent density functional calculations tend to become unstable when calculating disordered structures and disordered spin configurations. Finally, complicated structures of amorphous systems makes it difficult interpret the calculated results, even when we attain convergence in some calculations. To solve this problem, we constructed a method to analyze amorphous systems using the Gabriel graph [5], a graph based on the distance between the set of point shown in Figure 2 (a). Using the Gabriel graph, it is possible to define the nearest neighbors in an amorphous systems. It is then possible to draw Gabriel graph of calculated amorphous alloy, as in Fig. 2 (b).

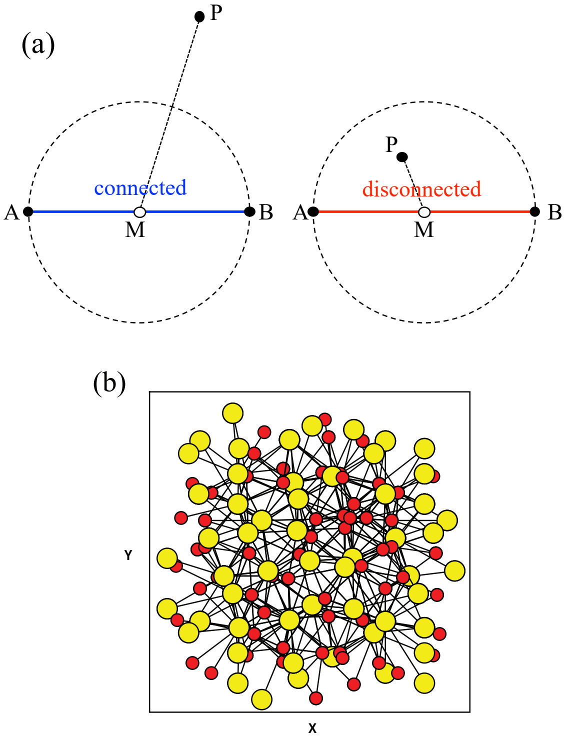

Figure 2: (a) A schematic of Gabriel graph. In the Gabriel graph, the criterion to connect points A and B is judged from the distance from the middle point M between A and B. When there are no nearer points than A or B, A and B are connected. If any other nearer points are found, they are disconnected. (b) A Gabriel graph calculated from the amorphous Nd-Fe alloy, containing about 40 % of Nd. The larger yellow circles and smaller red circles correspond to Nd and Fe atoms, respectively.

Determining the nearest neighbor sets of atoms by Gabriel graph, it is possible to examine the magnetism using a simple Heisenberg model. When assuming exchange coupling between only nearest neighbors which depends on the species of two atoms and independent of distances, it is possible to write the relationships between total energy and the magnetic moment as follows:

$$\begin{aligned} E \approx\ & E_0 - 2\bar{J}_{\text{Fe-Fe}}\sum_{i\text{-}j\in\text{Fe-Fe}}\mu_i\mu_j \\ & -2\bar{J}_{\text{Fe-Nd}}\sum_{i\text{-}j\in\text{Fe-Nd}}\mu_i\mu_j \\ & -2\bar{J}_{\text{Nd-Nd}}\sum_{i\text{-}j\in\text{Nd-Nd}}\mu_i\mu_j, \end{aligned} \tag{1}$$

where E is the total energy of DFT calculations, μ_i is the magnetic moment of atom i, $\bar{J}_{\text{X-Y}}$ is the exchange coupling between nearest neighbor pairs of atoms of species X and Y. Since E and μ_i can be obtained from DFT calculations, it is possible to determine $\bar{J}_{\text{Fe-Fe}}$, $\bar{J}_{\text{Fe-Nd}}$, $\bar{J}_{\text{Nd-Nd}}$ from several sets of calculations having the same atomic coordinates and different spin configurations. It was possible for us to obtain 8 different spin configurations which gave converged results for the amorphous Nd-Fe alloy shown ing Fig. 1, and the exchange coupling constants were calculated as follows: $\bar{J}_{\text{Fe-Fe}} = 3.637$ [meV/μ_{B}^2], $\bar{J}_{\text{Fe-Nd}} = 1.614$ [meV/μ_{B}^2] and $\bar{J}_{\text{Nd-Nd}} = -3.594$ [meV/μ_{B}^2]. And using these exchange coupling constants, we are able to calculate the paramagnetic curie temperature of the alloy as 871 K.

Calculations and interpretations of magnetism of amorphous materials had been a big challenge for materials science for many decades, and our approach can open up a new perspective to the amorphous magnetism.

References

[1] K. Hono *et al.*, Scripta Mater. **67**, 530 – 535 (2012).

[2] T. T. Sasaki *et al.*, Acta Mater. **115**, 269 (2016).

[3] T. Ozaki, Phys. Rev. B **67**, 155108 (2003).

[4] I. Štich *et al.*, Phys. Rev. B **44**, 11092 (1991).

[5] K. R. Gabriel *et al.*, Society of Systematic Biologists, **18**, 259 – 270 (1969).

Electron-Phonon Interactions in Isotopic Diamond Superlattice

Yuki Bando, Toyoda Masayuki, and Susumu Saito
Department of Physics Tokyo Institute of Technology
2-12-1 Ookayama, Meguro-ku, Tokyo 152-8550 Japan

The isotopic diamond superlattices that are periodic arrays of layers of carbon isotopes, such as ^{12}C and ^{13}C, with diamond structure, have been known to confined carriers to the layers of the lighter isotope (12C) due to the isotope effect on the electron-phonon interaction [1]. This phenomena has a great potential to realize the band-gap engineering in diamonds and to utilize diamonds as electronic devices. In this study, we developed the tight-binding model which enables us to calculate the electron-phonon interactions for various structures of isotope diamond superlattice efficiently. We compared the result of adiabatic Allen-Heine-Cardona theory between tight-binding model and density functional perturbation theory (DFPT) [2]. The DFPT calculations were performed by using ABINIT code [3] on the cpu nodes of system B. The visualized images of the crystal structures were created by using XCrySDen [4].

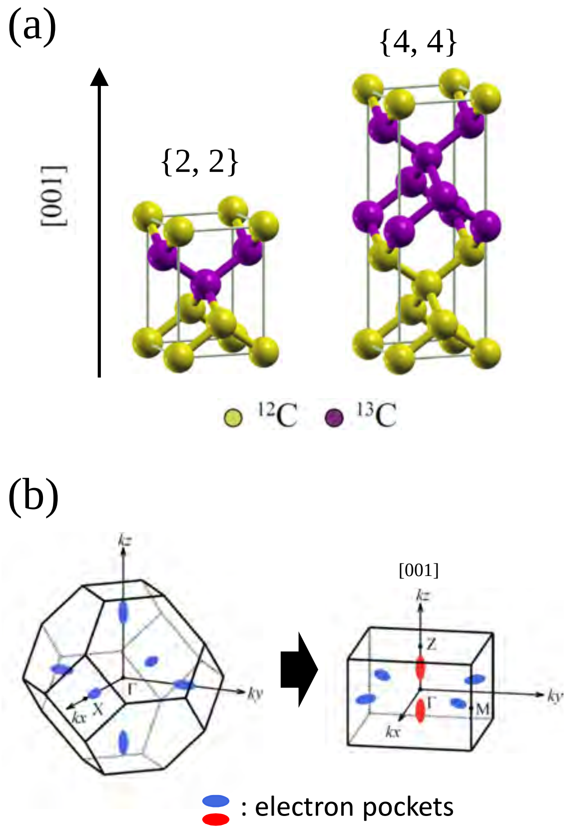

Figure 1: Tetragonal unit cells of $\{2, 2\}$ and $\{4, 4\}$ isotope diamond supperlattices (see text for the defnition of the labels). (b) Schematic image of the electron-pockets in the fcc (simple diamond) and tetragonal (superlattices) Brillouin zones.

Figure 1(a) shows the crystal structures of the superlattices. The stacking direction is along [001] and each structure is labeled as $\{m, n\}$ that means it consists of periodic arrays of m atomic layers of ^{12}C and n atomic layers of ^{13}C. The tetragonal unit cells of the superlattices have a lower symmetry than the original $Fd\bar{3}m$ symmetry and thus the electron-phonon interaction would modify the electronic structure in such a way that it breaks the original symmetry. One of such examples is schematically shown in Figure 1(b), where the six identical electron pockets in diamonds are separated into two groups in superlattices: two pockets along Γ-Z line and four along Γ-M line.

We constructed a tight binding model to calculate electron-phonon interactions using localized orbitals. This tight binding model is based on Wannier representation of electron-phonon interactions [5]. The electron-phonon matrix elements are strongly localized with respect to the distance between atomic vibrations and electronic orbitals in the case of diamond. Therefore, we can consider these quantities just as hopping parameters. We used one hopping parameter to describe FAN term Σ_{FAN} of electron-phonon interactions among valence states. This parameter was fitted with the sum of Σ_{FAN} + diadonal Debye-Waller term Σ_{dDW} calculated by DFPT at Γ.

Figure 2 shows zero point renormalization (ZPR) calculated by tight binding model and DFPT in fcc diamond. Even though we used only one parameter and not include Σ_{dDW} term directly, the ZPRs of tight binding model on momentum space are highly similar to those of DFPT.

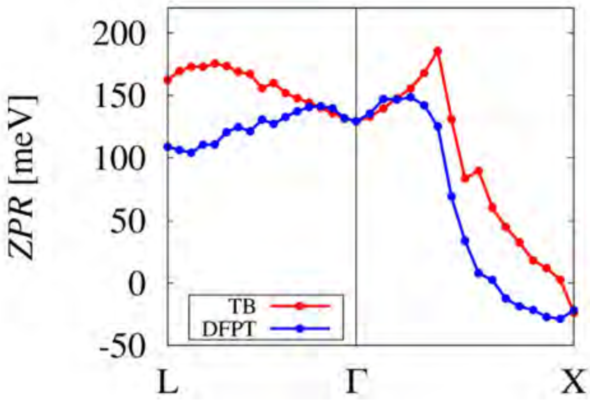

Figure 2: ZPR of the valence band top state calculated by tight binding (TB) model and DFPT

Figure 3 shows the valence band structure in tetragonal diamond along [001] direction. The valence band top state rise up due to ZPR. On the other hand, the valence band bottom state fall down slightly due to ZPR. These behavior are good agreement with those in case of DFPT calculation in fcc diamond.

As a conclusion, we found that newly developed tight binding model has the possibility to compute electron-phonon interactions in isotopic diamond superlattice quantitatively. In the future research, we will include Σ_{dDW} and a couple of conduction states into electron phonon interactions, and will carry out more detailed analysis in various structures of isotopic diamond superlattice.

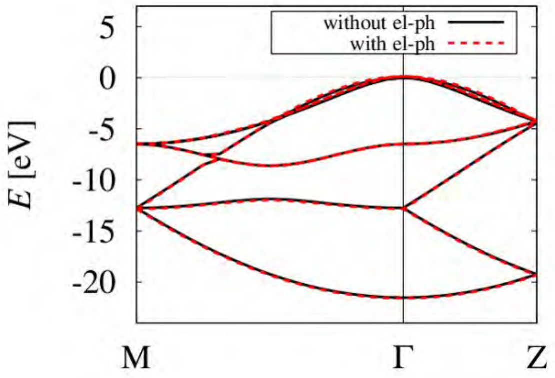

Figure 3: Valence band structure computed by tight binding model in tetragonal diamond

References

[1] H. Watanabe, et al, Science **324** (2009) 1425.

[2] S. Ponce, et al, Phys. Rev. B **90** (2014) 214304.

[3] X. Gonze, et.al, Computer Physics Communications **180** (2009) 2582-2615.

[4] A. Kokalj, Comp. Mater. Sci., **28** (2003) 155.

[5] F. Giustino, et.al, Phys. Rev. B**90** (2007) 165108.

Organic Molecules under High Pressure and Electronic Structures of B-C-N materials

Toshihiro Shimada, Ichiro Yamane, Takahiro Tamura, Takashi Yanase, Taro Nagahama
Division of Applied Chemistry, Faculty of Engineering
Hokkaido University, Sapporo 060-8628

Nitrogen and/or boron containing carbon materials are important because various functions are expected. However, the synthesis of these materials are in primitive stage and it is very difficult to obtain three dimensional solid as designed.

Synthesis under high pressure is a powerful technique to obtain novel materials. We are experimentally studying what happens when high pressure is applied to organic crystals to study possible synthesis of new carbon materials. In order to explain the experimental results and extract knowledge about the chemical reactions, we used ISSP supercomputer.

First, we explain our research on nitrogen containing molecules. Experimentally, single crystals of an organic molecule with nitrogen atoms (quinoxalino[2',3':9,10]phenanthro [4,5-abc]phenazine (TQPP), Fig. 1) are used as precursor. After high pressure treatment at room temperature, precursor molecules underwent oligomerization accompanied by transformation from sp^2-hybridization carbon atoms to sp^3 ones. We used a DFT package VASP [2] to understand the process in computer. We used PBE functional[3] and plane wave. Hydrostatic pressure was simulated by adjusting cell parameters and calculating the total energy change. To analyze oligomerization and structure of product, structural optimization calculation was performed starting from structure of TQPP crystal obtained by single crystal X-ray diffraction. When the structure was compressed with quasi-hydrostatic condition in simulation, TQPP molecules in the crystal polymerized and column-like one dimensional polymer was obtained (Fig. 2).

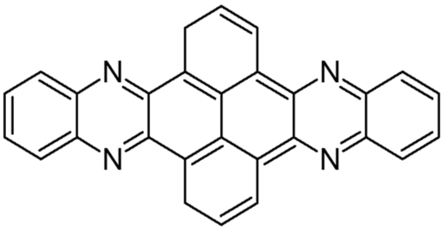

Fig. 1. Molecular structure of TQPP

Second, we computationally studied the electronic structures of graphene-like layered structures consisting of carbon, boron and nitrogen atoms. We replaced boron or nitrogen atoms to carbon atoms starting from hexagonal boron nitride. We previously reported that oddnumbered uneven substitution has given two dimensional metals with very different work functions (3.01 eV and 4.88 eV) [4].

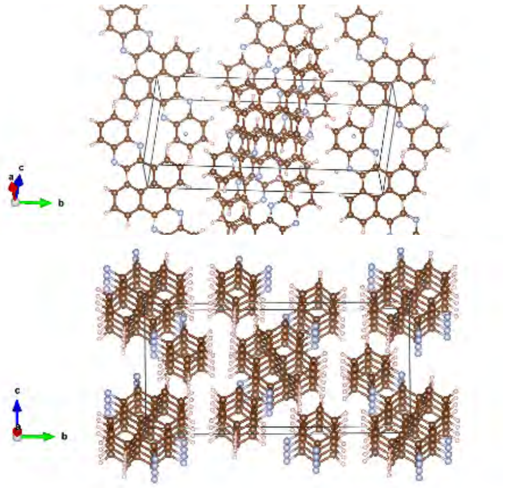

Fig. 2. Crystal structure of TQPP determined experimentally (above) and Structure of tube-like polymerized TQPP obtained by structural optimization under compression (below)

Using ISSP supercomputer, we examined the effect of C doping to hexagonal boron nitride (h-BN) to its electronic structure is examined by first principles calculations using the association from π-electron systems of organic molecules embedded in a two-dimensional insulator. In a monolayered carbon-doped structure, odd-number doping with carbon atoms confers metallic properties with different work functions. Various electronic interactions occur between two layers with odd-number carbon substitution. A direct sp^3 covalent chemical bond is formed when C replaces adjacent B and N in different layers (Fig.3, electron localization function by VASP). A charge transfer complex between layers is found when C replaces B and N in the next-neighboring region, which results in narrower band gaps (e.g. 0.37 eV). Direct bonding between C and B atoms is found when two C atoms in different layers are at a certain distance.

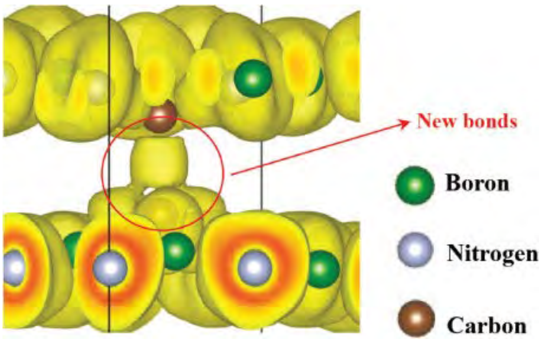

Fig. 3. sp^3 C-C bond formation between layers

References

[1] S. Yamanaka et al., J.Am.Chem.Soc. 130, 4303(2008).

[2] G. Kresse and J. Furthmüller,, Phys. Rev. B 54, 11169 (1996).

[3] J. P. Perdew, K. Burke, M. Ernzerhof, Phys. Rev. Lett. 77, 3865 (1996).

[4] Wei Xie, T. Yanase, T. Nagahama, T. Shimada, C-J.Carbon Res. 2 (2016) 2.

[5] Wei Xie, T. Tamura, T. Yanase, T. Nagahama, T. Shimada, Jpn. J. Appl. Phys. 57 (2018) 04FL11.

Finding the ground state of Prussian blue derivatives

Yoyo HINUMA
Center for Frontier Science
Chiba University, 1-33 Yayoicho, Inage, Chiba, Chiba 263-8522

$Na_xCo[Fe(CN)_6]_{0.09}$•$2.9H_2O$ is a Prussian blue analogue material that can be used as a sodium battery cathode (crystal structure without Na and H_2O shown in Fig. 1). There are two transition metal elements that change valence; at $0<x<0.6$, Co is 3+ and Fe valence changes between low spin (LS) +3 and LS +2, while at $0.6<x<1.6$ Fe is LS 2+ and Co is between +3 and +2. [1] The crystal structure of a similar material, $Na_xMn[Fe(CN)_6]_y$•zH_2O, has a similar crystal structure and can be cubic, rhombohedral, and monoclinic depending on x and temperature.

Ground state structure search from a high symmetry crystal by iterating calculation of supercell force constants, finding dynamic instabilities and then deforming along the direction indicated by the instabilities has been demonstrated in Cu using VASP and phonopy codes [3].

Interestingly, no imaginary phonon modes were found in cubic $MnFe(CN)_6$ (space group $Fm\text{-}3m$) based on PBEsol+U and SCAN approximations. This was unexpected because octahedral LS Fe^{3+} should be subject to Jahn-Teller distortion.

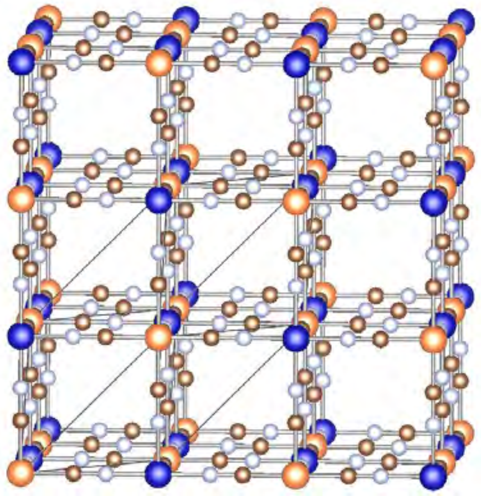

Fig. 1 Jungle gym like crystal structure of cubic $CoFe(CN)_6$. Lines indicate the primitive cell. Large blue, large orange, small brown, and small gray balls are Co, Fe, C, and N respectively. Na can enter cubes with 12 Co-C-N-Fe edges.

References

[1] M. Takachi et al.: Appl. Phys. Express **6** (2013) 025802.

[2] Y. Moritomo et al.: J. Phys. Soc. Jpn. **80** (2011) 103601.

[3] A. Togo and I. Tanaka, Phys. Rev. B. **87** (2013), 184104.

First-principles study of atomic structures, stabilities, and electronic properties of atomic-layered materials

Yoshitaka FUJIMOTO
Depertment of Physics, Tokyo Institute of Technology
Oh-okayama, Meguro, Tokyo 152-8551

Graphene has received much interest from fundamental nanoscience and applicable nanotechnology due to various unique properties, and is a good candidate material for future nanoelectronics devices including gas sensors.

We here report first principles density functional study to examine atomic structures, stabilities, and electronic properties of various gas molecules including environmentally polluting gas molecules adsorbed on the B-doped graphene [1, 2].

We first study the adsorption energies and atomic structures of various gas molecules adsorbed on the B-doped graphene monolayer. It is found that the NO and NO_2 molecules can bind with chemical bonds with large adsorption energies and short distances between gas molecules and the B-doped graphene. The B atom protrudes from the planar graphene sheet due to a chemical bond between the O atom in the NO_2 molecule and the B atom in the B-doped graphene, whereas it still resides in the planar sheet for the NO molecule adsorption.

We next study the energy band structures near the Fermi energy for the B-doped graphenes adsorbed with NO and NO_2 molecules. When the NO molecule is adsorbed, the two unoccupied flat NO-molecule related states appear above the Fermi energy. When the NO_2 molecule is adsorbed, the unoccupied NO_2-related state appears above the Fermi energy.

We also study the electronic properties of the NO and NO_2 molecules adsorbed on the B-doped graphene monolayer. The adsorption of the NO (NO_2) molecule induces the charge transfers between the N (O) atom in the NO (NO_2) molecule and the B atom in the graphene: for the adsorption of the NO molecule, electrons move from the NO molecule to the B-doped graphene, while for the adsorption of NO_2 molecules, electrons move from the B-doped graphene to the NO_2 molecule.

We here study the work functions of B-doped graphenes with and without NO and NO_2 molecules. Our calculated work function of the pristine monolayer graphene is 4.44 eV, and is in agreement with the experimental observations. The work function of the B-doped graphene is larger than that of the pristine graphene. When the NO molecule is attached to the B-doped graphene, the work function decreases. On the other hand, the work function of the B-doped graphene increases when the single NO_2 molecule is adsorbed.

We study the scanning tunneling microscopy (STM) images of the B-doped graphenes with NO and NO_2 molecules. The theoretical STM image of the B-doped graphene without adsorbates has the triangle-shaped corrugation, and agrees with the experimentally observed images. The STM image of the graphene surface with the NO molecule has two ring-like corrugations above the NO molecule when the NO molecule is adsorbed. For the case of the NO_2-molecule adsorption, there exist large and small spherical-shaped protrusions above the NO_2 molecule.

In summary, we have examined the adsorptions of the various molecules including environmentally polluting gases on B-doped graphene monolayers using first-principles density-functional calculations. The NO and NO_2 molecules can bind with chemical bonds on the B-doped graphene monolayer. The adsorptions of the NO molecule and the NO_2 molecule give rise to the charge transfers between the NO (NO_2) molecule and the B-doped graphene.

References

[1] Y. Fujimoto and S. Saito, Chem. Phys. **478**, 55 (2016).

[2] Y. Fujimoto and S. Saito, submitted.

Research on work functions of mixed anion layered compounds LaCuSO

Yoichi KAMIHARA
Department of Applied Physics and Physico-Informatics, Keio University
3-14-1 Hiyoshi, Yokohama, Kanagawa 223-8522

The mixed anion compounds with a ZrCuSiAs-type structure (known as 1111-like systems) has attracted a great interest due to their important properties of potential applications. LaCuSO is one of the typical examples of having the structure. It has alternately stacked layered structures composed of a lanthanum oxide layer with a large band gap and a copper sulfide layer as a conductive layer. It is possible to exhibit functionality by a two-dimensional electronic structure controlled electronic state by making lattice defect at the respective element sites.

In this report, we focus and analyze surfaces of LaCuSO, which are expected as a candidate for new catalytic materials with crystallographically vacant sites at several sites. In first, we analyze work functions of these materials.

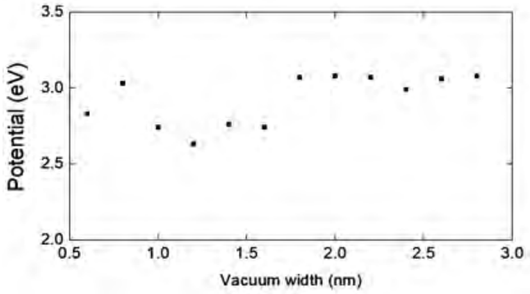

Figure 1: Vacuum energy level as a function of vacuum width for LaCuSO (001) slab model. Positions of atoms are relaxed where the Hellman-Feynman forces were reduced until 0.1 eV nm^{-1}.

Considering the two-dimensional crystal structure, only the surface in the c-axis direction was treated. For description of the surface, we used a slab geometry, which is infinite and periodic in the direction parallel to the surface but finite in the perpendicular direction. The supercell consists of an atomic region where unit cells are expanded to 2×2×1 and a vacuum region with a thickness of 1.8 nm determined by preliminary test calculation (Fig. 1). We consider the LaO-terminated LaCuSO surface and CuS-terminated one (Fig. 2). The surface relaxation was considered a slab thickness of 3 layers from surface and 4-6 layers are fixed. Work function Φ is defined as follows.

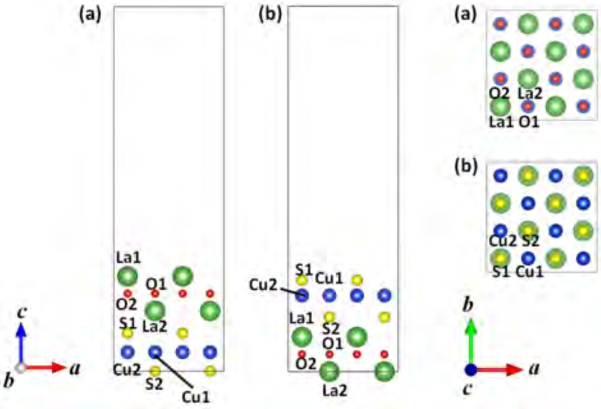

Figure 2: (a) LaO-terminated 2×2×1 LaCuSO (001) slab model. (b) CuS-terminated 2×2×1 LaCuSO (001) slab model. The thickness of vacuum region is 1.8 nm.

$$\Phi = E_{\mathrm{vac}} - E_{\mathrm{F}} \tag{1}$$

where E_{vac} is the energy level of the vacuum and E_F is the Fermi energy. E_F is calculated by the following formula because of the difference in Fermi energy between slab and bulk.

$$E_{\mathrm{F}} = E_{\mathrm{fermi}}^{\mathrm{bulk}} - E_{\mathrm{core}}^{\mathrm{bulk}} + E_{\mathrm{core}}^{\mathrm{slab}} \tag{2}$$

where $E^{\mathrm{bulk}}_{\mathrm{fermi}}$, $E^{\mathrm{bulk}}_{\mathrm{core}}$, $E^{\mathrm{slab}}_{\mathrm{core}}$ are calculated Fermi energy of bulk, energy level of the core-like state of bulk and that of slab, respectively. An example of the result is shown below. Fig. 3 is a diagram of the potential distribution in the surface vertical direction. The potential here includes potential due to ions and Hartree term, not including exchange correlation term.

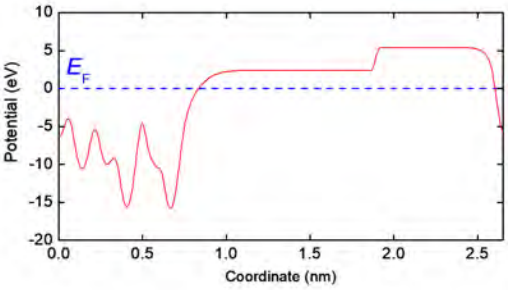

Figure 3: Electronic potential distribution of LaCuSO (001) slab model. The horizontal axis is a coordinate perpendicular to the surface. The constant region in the right corresponds to the vacuum region.

Each calculation has been carried out based on density functional theory (DFT) using Projector Augmented Wave (PAW) method[1] implemented in the Vienna ab-initio Simulation Package (VASP)[2]. Generalized gradient approximation (GGA) of Perdew-Burke-Ernzerhof (PBE) functional[3] was adopted for exchange-correlation energy. Dipole correction based on Neugebauer's method[4] is adopted in order to correct error due to artificial electric field asymmetry caused by periodic boundary condition of model.

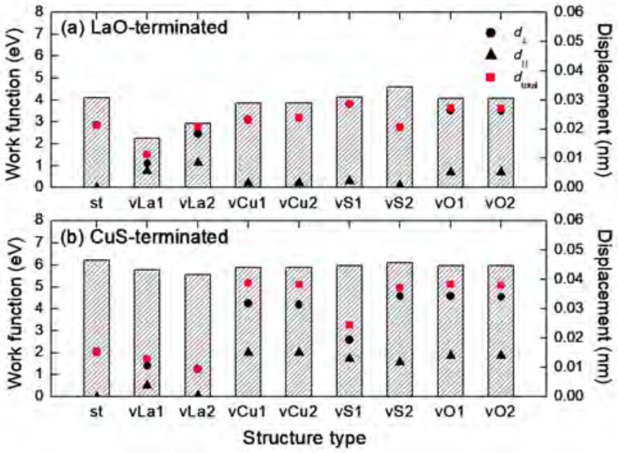

Figure 4: Summary of the surface properties of (a) LaO-terminated and (b) CuS-terminated LaCuSO surface with and without deficiency. Work functions are shown by bar graph with the left axis. The average displacements are plotted with the right axis. Structure "st" means a surface having a stoichiometric composition. Structure vXX means the surface having vacancy defects on XX site of Fig. 2. Each defect surface has the rate of 12.5 % vacancy.

Fig. 4 shows that the work function of LaO-terminated LaCuSO surface tends to be lower than that of CuS-terminated surface. Besides, on the LaO-terminated surface, the changes in the work function with respect to the vacancy is more remarkable than the other surface. The plots on Fig. 4 show the average displacement of surface atoms. The difference in displacement between the stoichiometric surface and the defect surface is larger on the CuS-terminated surface than on the LaO-terminated one. Therefore, the stabilization by surface relaxation is more pronounced on the CuS-terminated surface. For this reason, it is considered that the change in work function due to defect is smaller on the CuS surface and larger on the LaO surface.

The work function of two different surfaces of LaCuSO are calculated. The work function of the LaO terminating surface tends to be smaller. Moreover, it is suggested that dependence of work function on vacancy is larger on the LaO-terminated surface than on the CuS-terminated surface.

References

[1] P. E. Blöchl: Phys. Rev. B **50** (1994) 17953.

[2] G. Kresse and J. Hafner: Phys. Rev. B **47** (1993) 558.

[3] J. P. Perdew, K. Burke and M. Ernzerhof: Phys. Rev. Lett. **77** (1996) 3865.

[4] Jorg Neugebauer and Matthias Scheffl: Phys. Rev. B **46** (1992) 16067.

Quantitative Calculations of Momentum Distribution Function and Quasiparticle State in Ferromagnetic Transition Metals and Compounds Based on the First-Principles Momentum Dependent Local Ansatz Theory

Yoshiro KAKEHASHI
Department of Physics and Earth Sciences, Faculty of Science, University of the Ryukyus,
1 Senbaru, Nishihara, Okinawa, 903-0213, Japan

Though the density functional theory (DFT) is an excellent method to calculate the ground state properties, it is well-known that the quantitative aspects become worse with increasing Coulomb interaction strength. In order to describe correlated electrons quantitatively and to remove the difficulties in the DFT, we have recently proposed the first-principles momentum dependent local ansatz (MLA) wavefunction method on the basis of the tight-binding LDA+U Hamiltonian [1].

In this project, we have extended the MLA to the ferromagnetic case, and performed the numerical calculations of the ground state for Fe, Co, and Ni to clarify the quantitative aspect of the theory.

In the ferromagnetic state, we have to introduce the momentum dependent variational parameters so that the two-particle excited states are independent each other. In the cubic system, self-consistent 26 parameters appear including correlation energy ϵ_c, chemical potential μ, local charge n_L, as well as the magnetization m_L.

Assuming μ, n_L, and m_L which determine the potential energy, we solve the Hartree-Fock type one electron energy eigen value equations, as shown in Fig. 1. After we obtain the energy bands, we solve the self-consistent equations obtained from the variational principle. Then we know the wavefunction and calculate new chemical potential μ, local charge n_L, and the magnetization m_L. We perform the iteration loop until the self-consistency is achieved.

We obtained the spin magnetizations 2.44 $\mu_{\rm B}$ for Fe, 1.71 $\mu_{\rm B}$ for fcc Co, and 0.54 $\mu_{\rm B}$ for Ni, respectively. These values are compared with 2.15 $\mu_{\rm B}$ (LDA) and 2.46 $\mu_{\rm B}$ (GGA) for Fe, 1.59 $\mu_{\rm B}$ (LDA) and 1.66 $\mu_{\rm B}$ (GGA) for Co, 0.62 $\mu_{\rm B}$ (LDA) and 0.66 (GGA) for Ni, and show better agreement with the experimental values (2.22 $\mu_{\rm B}$ for Fe, 1.72 $\mu_{\rm B}$ Co, and 0.57 $\mu_{\rm B}$ for Ni).

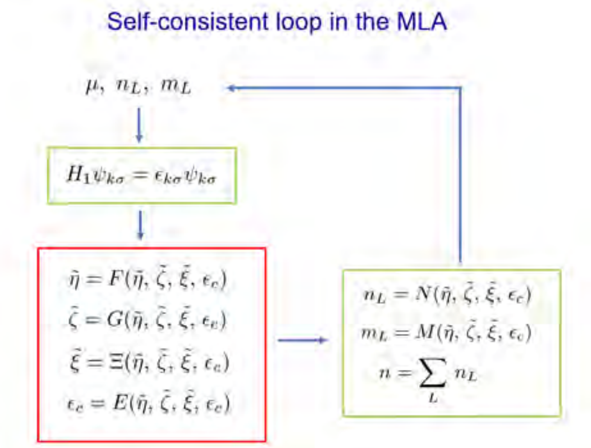

Figure 1: Self-consistent loop in the Momentum-dependent Local Ansatz (MLA) theory.

References

[1] Y. Kakehashi and S. Chandra, J. Phys. Soc. Jpn. **85**, 043707 (2016); **85**, 064714 (2016), 084708 (2016); **86**, 034711 (2017).

Computational Phase and Morphology Design of Electrochromic WO_3

Ahin Roy and Yukio Sato
Department of Materials Science and Engineering,
Kyushu University, 744 Motooka, Nishi-ku, Fukuoka 819-0395

WO3, an electrochromic material, exists in a myriad of phases. Recent experiments show that through use of oxalate capping in a hydrothermal reaction, it is possible to control phase and morphology of WO_3. [1] In order to elucidate the electronic interaction in the capping process, we carried out *ab initio* simulations for oxalate capping on hexagonal (11-20) and orthorhombic (001) surfaces, as shown in Figure 1a and 1b. The calculations with all electron projector augmented wave PBE potentials with generalized gradient approximation were carried out with the Vienna Ab Initio Simulation Package (VASP) code. [2]

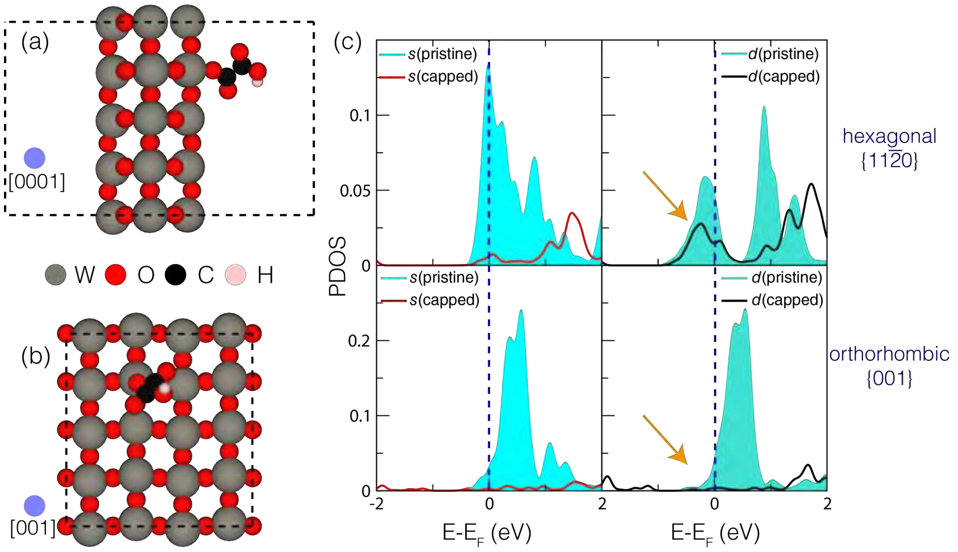

Figure-1: Relaxed geometries of the oxalate capped (a) hexagonal (11-20) and (b) orthorhombic (001) surfaces, the unit cell is marked in black dotted solid line; (c) shows the *l*-decomposed electronic density of states (DOS) projected on the adsorption site. The upper panel shows the adsorption-induced changes in the DOS for hexagonal (11-20) surface, and the lower panel shows the changes for the orthorhombic (001) surface.

In such a scenario, the binding energy of the oxalate on the hexagonal (11-20) surface and orthorhombic (001) surface was found to be -0.61 eV, and -1.26 eV respectively. This clearly shows that the oxalate species binds more strongly on orthorhombic phase, leading to a lower interfacial energy, and hence can act as a phase-directing agent.

To understand the electronic interaction during the capping of different facets of WO_3, we calculated the *l*-decomposed electronic density of states (DOS) projected on the capping site. As can be seen from Figure 1c, there is a large depletion of the both *s*- and *d*-states near Fermi energy, in the case of capping in orthorhombic WO_3 compared to that of hexagonal WO_3. The simulation results clearly show that oxalate interacts with the orthorhombic surface more strongly compared to hexagonal surface. A stronger interaction implies a lower interfacial energy, leading to a phase-selection during nucleation. Moreover, because of the binding of the oxalate on (001) surface, the growth in the [001] direction is prohibited, and forms a 2-D morphology. Whereas, absence of oxalate leads to formation of hexagonal phase, which grows in anisotropic *c*-direction leading to a rod morphology.

The two synthesized phases exhibit very different electrochromic property. Experiments illustrate that under an applied voltage H^+ can intercalate into the phases changing its color from yellow to blue. The H^+ diffusion co-efficient was found to be higher in the case of hexagonal WO_3 compared to that of orthorhombic one. Hence, the color switching was faster for hexagonal phase.

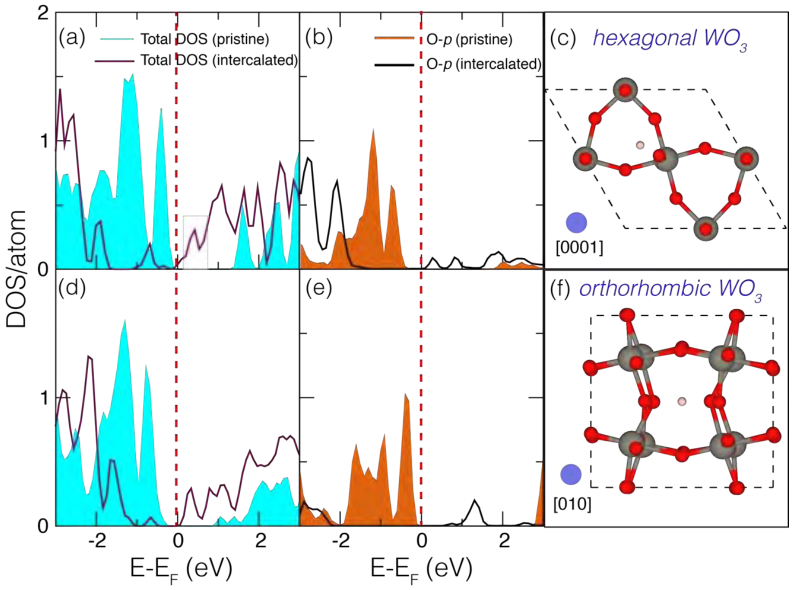

Figure-2: (a) Total DOS and (b) PDOS of the hexagonal phase before and after intercalation of H^+; (c) shows the H^+-intercalated hexagonal WO_3; (d) and (e) are the Total DOS and PDOS of the orthorhombic phase before and after intercalation of H^+; (f) is the structure of H^+-intercalated orthorhombic WO_3.

In order to understand the H^+-intercalation in details, we investigated the intercalation induced electronic structure changes. The intercalation energy E_{int} of the H^+-ion in the hexagonal/orthorhombic phase can be calculated as follows:

$$E_{int} = E_{int-struc} - E_{bulk} - E_{H2O/H^+}$$

where, $E_{int-struc}$ is the total energy of the H^+-intercalated unit cell, E_{bulk} is the energy of the hexagonal/orthorhombic WO_3 phase in bulk state, and E^0_{H2O/H^+} is the ionization potential of H_2O to generate H^+ ion (0.42 eV, considering the process as a one-electron process). The calculated E_{int} for hexagonal phase is 0.18 eV, whereas that for orthorhombic phase is 2.09 eV. This large contrast in the intercalation energy clearly rationalizes that the threshold voltage for H^+-intercalation would be lesser for the hexagonal phase compared to that of the orthorhombic phase. This also indicates that once intercalated, it would be harder for the H^+ ions to de-intercalate from the orthorhombic phase. Thus, the transmission switching is expected to be faster for the hexagonal phase, in agreement with the experiments.

To look at the electronic interaction in detail, the total and partial electronic DOS of the systems were carried out. As can be seen from Figure 2, there is a clear switching of the WO_3 from a semiconductor to metal upon H^+-intercalation. Such transition has been reported before, owing to the reduction of the WO_3. As can be seen from Figure 2b and 2e, the H^+-intercalation leads to a huge depletion of the oxygen *p*-states. This effect is more pronounced in case of the orthorhombic WO_3. The trend of such oxygen *p*-state depletion also follows the trend of E_{int}, reflecting a stronger electronic interaction and slower intercalation kinetics for the orthorhombic phase.

References:

[1] K. Ghosh*, A. Roy*, S. Tripathi, S. Ghule, A. K. Singh, and N. Ravishankar, Journal of Materials Chemistry C, 5, 7307-7316 (2017) (*equal contributions)

[2] G. Kresse and J. Hafner, Phys. Rev. B 47 , 558 (1993); ibid. 49 , 14 251 (1994)

Search for new electronic properties of new nanoscale interfaces

Katsuyoshi KOBAYASHI and Akiho KUBO
Department of Physics, Ochanomizu University
2-1-1 Otsuka, Bunkyo-ku, Tokyo 112-8610

In 2017 we theoretically studied the transition-metal dichalcogenide (TMD) monolayers in asymmetrical structures. TMDs are layered material having three-layer structures consisting of monatomic transition-metal layer sandwiched between two monatomic chalcogen layers. The two chalcogen layers are usually formed of identical elements. New structures with different chalcogen layers were experimentally synthesized in 2017 [1, 2]. We studied the atomic and electronic structures of the asymmetric TMD monolayers by the density-functional method. We used the program package VASP.

The atomic structures of TMD monolayers are 1H or 1T structures. The 1T structure has a modified structure with a double period named 1T′ structure. It is theoretically predicted that the TMDs in the 1T′ structure are quantum spin Hall insulators in the monolayer structure [3] and Weyl semimetals in stacked structures [4]. The total energy difference between the 1T and 1H structures are small, and it was experimentally succeeded to undergo the transition between these two structures by electron doping [5]. We calculated the atomic and electronic structures of MoSTe, MoSeTe, WSTe, and WSeTe as examples of asymmetric TMD monolayers. We studied the effect of electron doping in these systems. Following results were obtained from the calculations.

One is that the 1H structure has lower total energy than the 1T structure for all the four asymmetrical systems above. The 1H structure is the stable structure of the TMD monolayers in the symmetrical structure except for WTe_2 [6]. WSeTe is an intermediate system between WSe_2 and WTe_2 and may be regarded as one near to the former.

Next we studied the effect of electron doping. The total energy difference between the 1H and 1T structures decreases with increasing the amount of electron doping for all four systems. It undergoes the transition of stable structures from 1H to 1T at some amounts of doping in all the systems. This result is the same as the symmetrical structures [5]. It may be possible to materialize the 1T′ structure by electron doping in the case of the asymmetrical structures also.

Finally we calculated the electronic structures. The electronic states in the 1H structure are semiconductors for all four asymmetrical TMD monolayers. MoSeTe and WSeTe are direct gap semiconductors, and MoSTe and WSTe are indirect gap semiconductors. Both the top of valence bands and the bottom of conduction bands are located at the K point in the Brillouin zone in the former case. The top of valence bands is changed to the Γ point in the latter case. Band inversion between the d bands of transition metals and the p bands of chalcogens appear for all four asymmetical TMD monolayers in the 1T′ structure.

References

[1] A.-Y. Lu *et al.*: Nat. Nanotech. **12** (2017) 544.

[2] J. Zhang *et al.*: ACS Nano **11** (2017) 8192.

[3] X. Qian *et al.*: Science **346** (2014) 1344.

[4] A. A. Soluyanov *et al.*: Nature **527** (2015) 495.

[5] Y. Wang *et al.*: Nature **550** (2017) 487.

[6] Y. Li *et al.*: Nat. Commun. **7** (2016) 10671, Supplementary information.

Strain control of carrier localization in polar semiconductor materials

Hannes RAEBIGER
Department of Physics, Yokohama National University
Graduate School of Engineering
Tokiwadai, Hodogaya-ku, Yokohama 240-8501

Carrier localization or delocalization is typically considered a material property, i.e., shallow defects yield mobile, delocalized charge carriers, and deep defects trap charge carriers. We have previously demonstrated that in some particular systems, charge carriers exhibit a duality between trapped and delocalized, and by increasing the defect concentration, we may observe a second order phase transition from trapped to delocalized state [1]. This duality and ensuing physics of excitonic phases [2] is corroborated by numerous experiment (see Refs. in [1]). The key to unveiling such localization-delocalization dualities is the inclusion of a self-interaction correction [3], which have optimized for the use in magnetic semiconductors.

Motivated by our previous results, we investigated the coexistence of localized and delocalized states in Mn and Fe doped p-type GaN. In these systems, we find a variety of differently localized and delocalized states [4]: carrier holes localized on single anion sites are not equivalent, and we find a variety of extended states, including states delocalized along quasi-1D chains or 2D planes. These differently localized states have markedly different structural relaxations, and are very sensitive to lattice strain.

We exploit the strain sensitivity, and demonstrate that the carrier localization can be controlled by applying axial strain, as illustrated in Figure 1. This is explained by the interplay of the piezoelectric effect and the electric polarization of the differently localized charge carriers. This discovery offers the new perspective to switch on and off carrier channels in GaN, and other polar semiconductors.

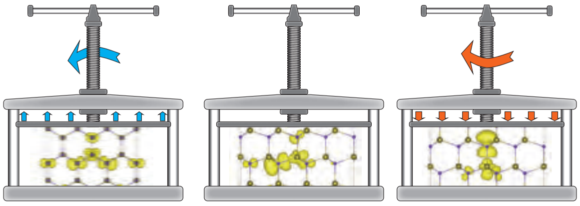

Figure 1: Hole localization around Fe impurities in GaN. Tensile strain (left) delocalizes hole carriers in plane perpendicular to strain axis, and compressive strain (right) localizes them along the strain axis. In unstrained GaN (center) holes around Fe impurities localize in the ab-plane.

References

[1] S. Bae and H. Raebiger: Phys. Rev. B (Rapid Communications) **94** (2016), 241115(R).

[2] W. Kohn: Phys. Rev. Lett. **19** (1949) 416.

[3] S. Lany and A. Zunger: Phys. Rev. B **80** (2009) 085202.

[4] H. Raebiger, S. Bae, C. Echeverria-Arrondo and A. Ayuela: Phys. Rev. Mater. **2** (2018) 024402.

First-principles statistical thermodynamics simulations on the structure and reactivity of heterogeneous catalysts

Fahdzi MUTTAQIEN, Teruo HIRAKAWA, Sasfan Arman WELLA, Yuji HAMAMOTO,
Kouji INAGAKI, Hidetoshi Kizaki, Ikutaro HAMADA, and Yoshitada MORIKAWA
Department of Precision Science and Technology,
Osaka University, Yamada-oka, Suita, Osaka 565-0871

We focus on chemical reactions at surfaces and interfaces including ligand-free Suzuki-Miyaura cross coupling reactions in aqueous solutions [1,2], CO_2 adsorption and hydrogenation on Cu surfaces [3,4], dependence of absorption spectra of Ru-complex on pH [5], oxygen vacancy diffusion in $Sr_3Fe_2O_{7-\delta}$ [6], and etching of SiC by Pt catalyst in water solution [7]. In the present report, we discuss CO_2 adsorption and hydrogenation on Cu(111) [3,4].

One of the most important intermediate steps in the methanol synthesis over Cu-based catalysts is CO_2 hydrogenation into formate (HCOO). Based on a kinetics analysis, it was suggested that formate synthesis takes place through an Eley-Rideal (ER) type mechanism, in which gas phase CO_2 directly reacts with adsorbed H. In the ER type mechanism, there is a possibility to enhance the reaction rate of formate synthesis by controlling the translational, vibrational, and rotational energies of impinging CO_2. The initial impinging CO_2 energies must be related to the energy states of desorbed CO_2 from formate decomposition bacause formate synthesis and decomposition are reversible reactions. Therefore, elucidation of formate decomposition dynamics is important for improving catalytic formate synthesis.

Very recently, the dynamics of desorbed CO_2 produced from the formate decomposition reaction has been studied by measuring the angle-resolved intensity and translational energy distribution of the steady-state reaction of formic acid (HCOOH) and oxygen on a Cu surface [8]. It was reported that the translational energy of desorbed CO_2 is approximately 0.10 eV and independent of the surface temperature. The measured CO_2 translational energy is much smaller than the activation energy of formate synthesis, which is 0.59 ± 0.05 eV, suggesting that internal modes, such as vibrational and rotational modes, should be excited in the desorbed CO_2. In this study, we therefore investigate the energy distribution of desorbed CO_2 as a formate decomposition product by means of *ab initio* calculations. We also show the importance of the van der Waals (vdW) correction in describing the adsorption and desorption processes of CO_2 on Cu surfaces[4]. From knowledge of desorbing product dynamics, we can deduce optimal conditions for the formate synthesis reaction through CO_2 hydrogenation.

The calculations were performed using a plane-wave pseudopotential code named "Simulation tool for Atom TEchnology (STATE)" [9,10]. Since the vdW correction is important to describe the adsorption and chemical reaction of inert molecules, we compare the Perdew-Burke-Ernzerhof (PBE) results and those obtained using vdW density functionals (vdW-DFs), i.e., the original vdW-DF (vdW-DF1), optB86b-vdW, and rev-vdW-DF2 functionals as implemented in the STATE code [11]. We performed *ab initio* molecular dynamics (AIMD) simulations starting from the transition state (TS) structure of the formate decomposition process to gas phase CO_2 and adsorbed H to evaluate the translational and internal (rotational and vibrational) energies of desorbed CO_2.

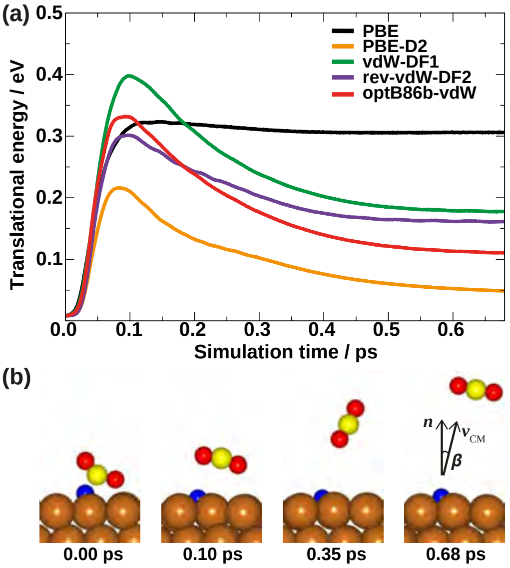

Fig. 1. a) Time evolution of the translational energy of desorbed CO_2 from formate decomposition calculated using PBE, PBE-D2, and vdW-DFs. (b) Representative snapshots from AIMD trajectory of CO_2 desorption.

We have investigated the minimum energy path of CO_2 hydrogenation into formate and the dynamics of formate decomposition into gas phase CO_2 and adsorbed hydrogen using density functional theory calculations. Based on the dynamics analysis of formate decomposition as shown in Fig. 1, the bending energy of desorbed CO_2 is twice larger than the translational energy. Since formate synthesis from CO_2 and H_2, the reverse reaction of the formate decomposition, is experimentally suggested to occur by the ER type mechanism, our results indicate that the reaction rate of formate synthesis can be enhanced if the bending vibrational mode of CO_2 is excited rather than the translational and/or stretching modes.

References

[1]. T. Hirakawa, Y. Uramoto, D. Mimura, A. Takeda, S. Yanagisawa, T. Ikeda, K. Inagaki, and Y. Morikawa, J. Phys. Chem. B, **121**, 164-173 (2017).

[2]. T. Hirakawa, Y. Uramoto, S. Yanagisawa, T. Ikeda, K. Inagaki, and Y. Morikawa, J. Phys. Chem. C, **121**, 19904-19914 (2017).

[3]. F. Muttaqien, H. Oshima, Y. Hamamoto, K. Inagaki, I. Hamada, and Y. Morikawa, Chem. Comm., **53**, 9222-9225 (2017).

[4]. F. Muttaqien, Y. Hamamoto, I. Hamada, K. Inagaki, Y. Shiozawa, K. Mukai, T. Koitaya, S. Yoshimoto, J. Yoshinobu, and Y. Morikawa, J. Chem. Phys., **147**, 094702-1-8 (2017).

[5]. S.-S. Tan, S. Yanagisawa, K. Inagaki, Y. Morikawa and M. B. Kassim, Phys. Chem. Chem. Phys., **19**, 25734-25745 (2017).

[6]. T. Ohta, H. Kizaki, and Y. Morikawa, J. Phys. Chem. C, **122**, 4172-4181 (2018).

[7]. P.-V. Bui, D. Toh, A. Isohashi, S. Matsuyama, K. Inagaki, Y. Sano, K. Yamauchi, and Y. Morikawa, Jpn. J. Appl. Phys., **57**, 055703-1-5 (2018).

[8]. J. Quan, T. Kondo, G. Wang, and J. Nakamura, Angew. Chem. Int. Edit., **56**, 3496-3500 (2017).

[9]. Y. Morikawa, Phys. Rev. B, **51**, 14802 (1995).

[10]. Y. Morikawa, K. Iwata, and K. Terakura, Appl. Surf. Sci. **169-170**, 11-15 (2001).

[11]. Y. Hamamoto, I. Hamada, K. Inagaki, and Y. Morikawa, Phys. Rev. B, **93**, 245440-1-9 (2016).

Study on an automatic derivation technique of first-principles effective model based on the many body electron theory

Hirofumi SAKAKIBARA

Department of Applied Physics and Mathematics,

Tottori University, Koyama-cho Minami, Tottori city, Tottori 680-8552

The automation of the derivation of low-energy models from fist-principles is one of the major purposes in condensed matter physics. The derivation of the Hubbard model, which is a minimal model for magnetisms and superconductivities driven by unconventional paring mechanisms, is very useful because the electron correlation effects can be accurately taken into account in such models. Therefore the automation possibly enables us to find novel magnetic/superconducting materials fully theoretically.

In the previous study, we have constructed a method to estimate Hubbard-type electron interactions denoted by U. We assume the equality between the screened interaction in full-orbital spaces and in model spaces, only consisting of target bands, to determine U. This constraint removes the double counting of screening effects between first-principles calculation and model calculations. We have named this method model-mapped RPA (mRPA) [1].

Here we explain more details of the mRPA. mRPA reconciles the two values; one is the "value" of the screened Coulomb interactions W from first-principles and the other is the screened interaction W_m from model calculation. The recently developed constrained random phase approximation (cRPA) is similar in its concepts, but actually different. Its "constraint" is the equality between the "operator", $W = W_{\mathrm{m}}$. This constraint leads to the equation $U = v/\{1 - v(P - P_m)\}$, where v is the bare Coulomb interaction, P is the full-space polarization and P_m is the polarization among the model space [2]. Namely, cRPA actually calculate the expectation value of the operator $v/\{1 - v(P - P_m)\}$. Therefore, the U_{mRPA} and U_{cRPA} are not necessarily equal to each other. Our previous report have shown that U_{cRPA}=2.0eV and U_{mRPA}=3.9eV in the single-band model of $\mathrm{HgBa_2CuO_4}$, which is a layered cuprate superconductor [1].

We have extended mRPA to apply to the multi-orbital system, because general systems require the multi-orbital degrees of freedom. Then the U becomes a matrix consists of four orbital legs. Generally, we cannot algebraically solve the equation $W = W_m$ in mRPA because W_m is a q-integral value denoted as $\Sigma U/(1 - U P_m)$. However, since we can calculate W_m from a parameter set (U, U', J, J'), we can obtain the appropriate parameter set by some updating algorisms approaching the "solution" which satisfy the $W=W_m$. In the actual mRPA code, a simple recursive substitution algorism is implemented.

We have determined the interaction matrix U of two-orbital model in La_2CuO_4 and in $HgBa_2CuO_4$ by the extended mRPA. Because the d_{z^2} orbital is heavily mixes with the $d_{x^2-y^2}$ orbital in La_2CuO_4, the two-orbital model incorporating the d_{z^2} orbital is necessary [3]. In contrast, in $HgBa_2CuO_4$ the orbitals are less mixed implying such system can be describe a conventional single-orbital model [4].

Based on the value of U from mRPA, we have also performed many-body calculations based on the fluctuation exchange approximation (FLEX). FLEX considers the self-energy from the spin and the charge fluctuations, and can estimate the superconducting pairing driven by such fluctuations.

By substituting Green's functions with the self-energy to the linearized Eliashberg's equation, we estimate the theoretical measure λ of the transition temperature (T_c) of superconductivity, where λ reaches unity at $T= T_c$. From the results, it is revealed that the orbital mixture effect from the d_{z^2} orbital controls T_c [3,4] rather than the material dependence of U. This independency of U is caused by the fact that the total pairing strength saturates as the self-energy becomes sufficiently large. This picture is obtained in the parametric region where $U > 2$eV. Note that the hopping integrals between the nearest neighbor copper sites are estimated to be about 0.45eV in general cuprates superconductors. The other cuprates superconductors are expected to be in the region of $U > 2$eV.

References

[1] H. Sakakibara *et al*: J. Phys. Soc. Jpn. **86,** 044714 (2017).

[2] F. Aryasetiawan, M. Imada, A. Georges, G. Kotliar, S. Biermann, and A. I. Lichtenstein, Phys. Rev. B **70**, 195105 (2004).

[3] H. Sakakibara *et al.,* Phys. Rev. Lett. **105** 057003 (2010).

[4] H. Sakakibara *et al*, Phys. Rev. B **89**, 224505 (2014).